Ph.D. Dissertation

Influence of high pressure on luminescent properties of $R\mathrm{AlO}_3$ and CsPbBr_3 perovskites

Wpływ wysokiego ciśnienia na własności luminescencyjne perowskitów $R\mathrm{AlO}_3$ i CsPbBr_3

M.Sc. Lev–Ivan Bulyk
Supervisor: Prof. Dr hab. Andrzej Suchocki

Institute of Physics, Polish Academy of Sciences

A thesis submitted in fulfillment of the requirements for
the degree of Doctor of Philosophy

Warsaw
April 2023

Table of contents

I. Preface

I am submitting this dissertation in partial fulfillment of the requirements for the degree of Doctor of Philosophy in Physics at the Institute of Physics, Polish Academy of Sciences (IP PAS). The research presented in this dissertation was carried out under the supervision of Professor Andrzej Suchocki at the Division of Physics and Technology of Wide–Band–Gap Semiconductor Nanostructures – ON4 of IP PAS, from October 2016 to September 2022. Throughout this period, I dedicated myself to the research and measurement aspects of this work, which is original and not previously published. The results and discussions presented in this dissertation are a reflection of my efforts and are not influenced by any external sources.

This dissertation comprises less than 51,000 words and is a testimony to the extensive research I conducted during my Ph.D. program. I take pride in my contributions to the field of physics and hope that this work will inspire future research in this area.

Lev–Ivan Bulyk
Warsaw
April 2023

II. Abstracts

II.1. Abstract

This study provides a comprehensive analysis of the luminescent properties of two different types of perovskites: rare–earth aluminum oxide perovskites ($RAlO_3$, where R represents Gd, Tb, Lu, Y, or a mixture) doped with Eu^{3+} and Ce^{3+} ions and cesium lead bromide ($CsPbBr_3$). Spectroscopic techniques were employed to investigate the luminescence centers and band gap properties of the materials, with a focus on high–pressure spectroscopic studies using a diamond anvil cell (DAC).

One part of the study focuses on the luminescent properties of Eu^{3+}–doped RAP (R = Gd, Tb, Y, Lu, or a mixture), which have applications in scintillation detectors. The K–value, which represents the ratio of the intensities of $^5D_0 \rightarrow {}^7F_2$ and $^5D_0 \rightarrow {}^7F_1$ transitions of Eu^{3+}, is studied as a function of pressure. The results show that YAP exhibits an atypical shift towards higher energy for some lines with increasing pressure, and the K–value of YAP is smaller compared to the other studied samples. In LuAP, the K–value's behavior on pressure is affected by the interaction of Eu^{3+} centers with defects, which manifest in luminescence as broadband and are attributed to Pb^{2+} dimers. The study concludes that the K–value parameter depends on several factors, including the lattice parameters of the perovskites, the symmetry of the local structure, the concentration of defects, and the strength of the interaction between defects and Eu^{3+} centers.

Another part of the study investigates the luminescent properties of Ce^{3+}–doped LuAP and YAP. The direct bandgap values of YAP and LuAP are determined to be 7.63 eV and 7.86 eV, respectively, through absorption measurements in the near–UV region. The luminescence of both YAP:Ce and LuAP:Ce is studied as a function of temperature up to 873 K, enabling the estimation of the position of the lowest excited *5d* level of Ce^{3+} relative to the bottom of the conduction band. The position of the *4f* levels is found to be consistent with the predictions of Dorenbos theory and DFT calculations. However, the pressure downshift of the *5d* energy levels of Ce^{3+} relative to the free Ce^{3+} ion, as calculated according to the Dorenbos theory, does not agree with experimental data. This disagreement is resolved by calculating the downshift relative to the bandgap energy of YAP and LuAP, which also allows for the correlation of the observed changes in the *5d* state energies under pressure in LuAP with the pressure–induced changes in the average cation–anion distances. Additionally, alternative hypotheses are considered. The high–pressure Raman experiment identifies a soft mode with an energy of 455.4 cm^{-1} at ambient pressure, the energy of which decreases with increasing pressure.

The study also investigates the photoluminescence properties of $CsPbBr_3$, a promising material for use in photovoltaic devices. Low–temperature and high–pressure photoluminescence measurements are conducted, revealing a complex luminescence spectrum with three main groups of lines: (i) direct (free) and indirect (Rashba) excitons and their phonon replicas, (ii) a broad defect band, and (iii) an unknown line at around 540 nm. The study shows that the sample's structure fluctuation affects its luminescent properties, with fluctuations responsible for the

increase in Rashba splitting and the quenching of defect luminescence with the temperature increase from cryogenic to room temperature. For the first time, low–temperature high–pressure luminescence was measured, which allowed for the resolution of free and Rashba excitons under high pressure. The analysis of the results shows that the free and Rashba excitons are competing deexcitation paths. Additionally, the study revealed blue emission from the bulk $CsPbBr_3$ under high pressure, which was explained by the rapid expansion of the $CsPbBr_3$ band gap at high pressures.

The work comprises ten sections, including a Preface, Abstracts, List of publications, Acknowledgments, Introduction, Experimental techniques, Results and discussion, Conclusions, Appendixes, and References. Chapter V. Introduction provides a literature review, while chapter VI. Experimental techniques outlines the experimental techniques employed in the study. Chapter VII. Results and discussion presents and discusses the experimental results, and chapter VIII. Conclusions summarizes the findings and outlines future research directions.

Overall, this work contributes to our understanding of the luminescent properties of perovskite materials and may prove to be a valuable resource for researchers working in scintillation and photovoltaic research.

II.2. Streszczenie

Ta praca przedstawia kompleksową analizę właściwości luminescencyjnych dwóch różnych typów perowskitów: glinowych perowskitów z ziemiami rzadkimi ($RAlO_3$, gdzie *R* reprezentuje Gd, Tb, Lu, Y lub ich mieszaninę) z domieszkami Eu^{3+} i Ce^{3+}, oraz bromku ołowiowo cezowego ($CsPbBr_3$). Do zbadania centrów luminescencyjnych i właściwości pasmowych materiałów wykorzystano techniki spektroskopowe, z naciskiem na badania spektroskopowe pod wysokim ciśnieniem za pomocą komórki diamentowej (DAC).

Jedna część badań skupia się na właściwościach luminescencyjnych Eu^{3+} w *R*AP (*R* = Gd, Tb, Y, Lu lub ich mieszaninie), które mają zastosowanie w detektorach scyntylacyjnych. Wartość K, która reprezentuje stosunek intensywności przejść $^5D_0 \rightarrow {}^7F_2$ i $^5D_0 \rightarrow {}^7F_1$ Eu^{3+}, została zbadana w funkcji ciśnienia. Wyniki pokazują, że w YAP niektóre linie Eu^{3+} wykazują nietypowe przesunięcie ku wyższej energii przy wzroście ciśnienia, a wartość K jest mniejsza w porównaniu do innych materiałów. W LuAP zachowanie wartości K pod wpływem ciśnienia odzwierciedla wpływ interakcji centrów Eu^{3+} z defektami, które objawiają się jako szerokie pasmo i są przypisywane dimerom Pb^{2+}. Stąd, parametr K zależy od kilku czynników, w tym od parametrów sieci perowskitów, symetrii struktury lokalnej, stężenia defektów i siły oddziaływania między defektami a centrami Eu^{3+}.

Kolejna część badań dotyczy właściwości luminescencyjnych LuAP i YAP domieszkowanych Ce^{3+}. Wartości przerwy wzbronionej YAP i LuAP wynoszą odpowiednio 7,63 eV i 7,86 eV, co zostało ustalone na podstawie pomiarów absorpcji w bliskim UV. Luminescencja YAP:Ce i LuAP:Ce została zbadana w funkcji temperatury do 873 K, co umożliwiło oszacowanie położenia najniższego poziomu wzbudzonego *5d* Ce^{3+} względem dolnej krawędzi pasma przewodnictwa. Położenia poziomów *4f* są zgodne z teorią Dorenbosa i obliczeniami DFT. Jednakże, przesunięcie w dół poziomów energetycznych *5d* Ce^{3+} w stosunku do swobodnego jonu, obliczone zgodnie z teorią Dorenbosa, nie zgadza się z danymi eksperymentalnymi. Tę niezgodność można jednak skorygować poprzez uznanie za poziom odniesienia wielkość przerwy energetycznej YAP i LuAP, co pozwala również na skorelowanie zaobserwowanych zmian w energii stanów *5d* pod wpływem ciśnienia w LuAP z ciśnieniowo–indukowanymi zmianami średniej odległości kation–anion. Dodatkowo rozważane są też alternatywne hipotezy. W eksperymencie wysokociśnieniowym Ramana zidentyfikowano miękki mod z energią 455,4 cm^{-1} przy ciśnieniu atmosferycznym, którego energia maleje wraz ze wzrostem ciśnienia.

Badania dotyczą również właściwości fotoluminescencyjnych $CsPbBr_3$ jako obiecującego materiału do zastosowań w urządzeniach fotowoltaicznych. Wykonano pomiar fotoluminescencji w niskiej temperaturze i wysokim ciśnieniu, ujawniając złożone widmo luminescencji z trzema głównymi grupami linii, pochodzącymi od: (i) prostych (swobodnych) i skośnych ekscytonów (ekscytonów Rashby) i ich replik fononowych, (ii) szerokiego pasma defektów, i (iii) nieznanej linii w okolicy 540 nm. Badanie pokazuje, że fluktuacje struktury sieci krystalicznej próbki wpływają na jej właściwości luminescencyjne, przy czym fluktuacje są odpowiedzialne za wzrost rozszczepienia Rashby oraz za wygaszanie luminescencji defektowej wraz ze wzrostem temperatury od kriogenicznej do pokojowej. Po raz pierwszy wykonano pomiary fotoluminescencji przy niskiej temperaturze i wysokim ciśnieniu, co pozwoliło na odseparowanie swobodnych ekscytonów i ekscytonów Rashby w wysokim ciśnieniu. Analiza wyników pokazuje, że ekscytony swobodne i ekscytony Rashby to konkurencyjne ścieżki deekscytacji. Ponadto, badania ujawniły niebieską emisję z objętości $CsPbBr_3$ w wysokim ciśnieniu, co zostało wyjaśnione przez szybkie rozszerzanie się przerwy wzbronionej $CsPbBr_3$.

Praca składa się z dziesięciu sekcji, w tym Wprowadzenia (Preface), Streszczeń (Abstracts), Listy publikacji (

List of publications), Podziękowań (Acknowledgments), Wstępu (Introduction), Opisu Technik Doświadczalnych (Experimental techniques), Wyników i dyskusji (Results and discussion), Wniosków (Conclusions), Dodatków (Appendixes), i Odnośników (References). Rozdział V (Introduction) zawiera przegląd literatury, podczas gdy rozdział VI (Experimental techniques) przedstawia zastosowane techniki eksperymentalne. Rozdział VII (Results and discussion) prezentuje i omawia wyniki eksperymentów, a rozdział VIII (Conclusions) podsumowuje wyniki i przedstawia kierunki dalszych badań.

Autor wyraża przekonanie, że praca ta przyczyni się do naszego zrozumienia właściwości luminescencyjnych materiałów perowskitowych i może okazać się istotnym źródłem informacji dla badaczy zajmujących się badaniami materiałów scyntylacyjnych i fotowoltaicznych.

III. List of publications and participation in conferences

This thesis is based on the following publications:

1) **Bulyk L.–I.**, Somakumar A. K., Przybylińska H., Ciepielewski P., Zorenko Y., Zhydachevskyy Y., Kudryavtseva I., Gorbenko V., Lushchik A., Brik M. G., Syrotych Y., Witkiewicz Łukaszek S., Fedorov A., Suchocki A. Influence of High Pressure on Ce^{3+} Luminescence in $LuAlO_3$ and $YAlO_3$ Single Crystals and Single Crystalline Layers. *J. Luminescence*. 2022, **252**, 119276, doi: 10.1016/j.jlumin.2022.119276.
2) **Bulyk L.–I.**, Zorenko Y., Gorbenko V., Suchocki A. Influence of High–Pressure on Eu^{3+} Luminescence in Epitaxial $RAlO_3$ (R = Gd, Tb, Lu, $Gd_{0,6}Lu_{0,4}$, or Y) Single Crystalline Films. *J. Luminescence*. 2020, **220**, 116991, doi: 10.1016/j.jlumin.2019.116991.

Other publications of the author:

3) Zhydachevskyy, Y.; Mykhaylyk, V.; Stasiv, V.; **Bulyk L.–I.**; Hreb, V.; Lutsyuk, I.; Luchechko, A.; Hayama, S.; Vasylechko, L.; Suchocki, A. Chemical Tuning, Pressure, and Temperature Behavior of Mn^{4+} Photoluminescence in Ga_2O_3−Al_2O_3 Alloys. *Inorg. Chem.* 2022, **61**, 18135−18146, doi: 10.1021/acs.inorgchem.2c02807.
4) **Bulyk, L.–I.**; Gamernyk, R.; Chornodolskyy, J.; Malyi, T.; Vistovskyy, V.; Demkiv, T.; Shtablavyi, I.; Voloshinovskii, A. Influence of the degradation processes on luminescent and photoelectrical properties of $CsPbBr_3$ single crystals. *J. Alloys Compd.* 2021, **884**, 161023. doi: 10.1016/j.jallcom.2021.161023.
5) Mykhaylyk, V. B.; Kraus, H.; **Bulyk, L.–I.**; Lutsyuk, I.; Hreb, V.; Vasylechko, L.; Zhydachevskyy, Y.; Wagnera, A.; Suchocki, A. Al_2O_3 co–doped with Cr^{3+} and Mn^{4+}, a dual–emitter probe for multimodal non–contact luminescence thermometry. *Dalton Trans.* 2021, **50**(41), 14820–14831. doi: 10.1039/d1dt02836g.
6) **Bulyk, L.–I.**; Antonyak, O. T.; Chornodolskyy, Y. M.; Gamernyk, R. V.; Demkiv, T. M.; Vistovskyy, V. V.; Suchocki, A. Conductivity of $CsPbBr_3$ at ambient conditions. *J. Phys. Stud.* 2021, **25**(4), 4801–1–4801–5. doi: 10.30970/jps.25.4801.
7) **Bulyk L.–I.**, Vasylechko L., Mykhaylyk V. B., Tang C., Zhydachevskyy Ya., Hizhnyi Y. A., Nedilko S. G., Klyui N. I., Suchocki A., Mn^{2+} luminescence of $Gd(Zn, Mg)B_5O_{10}$ pentaborate under high pressure, *Dalton Trans.* 2020, **49**, 14268, doi: 10.1039/d0dt01851a

8) Kaszewski, J., Rosowska, J., Witkowski, B. S., Wachnicki, Ł., Wenelska, K., Mijowska, E., **Bulyk, L.–I.**, Włodarczyk, D., Suchocki, A., Kozankiewicz, B., & Godlewski, M. Shape control over microwave hydrothermally grown Y_2O_3:Eu by europium concentration adjustment. *Journal of Rare Earths*. 2019, **37**(11), 1206–1212. doi: 10.1016/j.jre.2019.04.011.

9) Włodarczyk D., **Bulyk L.–I.**, Berkowski M., Glowacki M., Kosyl K. M., Kaczmarek S. M., Kowalski Z., Wittlin A., Przybylinska H., Zhydachevskyy Y., Suchocki A., High–pressure low–temperature optical studies of $BaWO_4$:Ce, Na crystals, *Inorg. Chem.* 2019, **58**(9), 5617–5629, doi: 10.1021/acs.inorgchem.8b03606.

10) Demkiv T., Halyatkin O., Chylii M., Malyi T., Vistovsky V., **Bulyk L.–I.**, Demkiv L., Voloshinovskii A., Luminescence of SrF_2–Ce nanoparticles under optical and X–ray excitation, *J. Phys. Stud.* 2019, **23**(3), Article 3705, doi: 10.30970/jps.23.3705.

11) Demkiv T., Halyatkin O., Chylii M., Malyi T., Vistovsky V., **Bulyk L.–I.**, Demkiv L., Voloshinovskii A., Luminescence peculiarities of polystyrene composite with embedded YVO_4:Eu nanoparticles, *J. Phys. Stud.* 2018, **22**(4), Article 4301, doi: 10.30970/jps.22.430

Participation in conferences:

1) High pressure studies of Ce^{3+} luminescence in epitaxial $LuAlO_3$ single crystalline film, **Lev-Ivan Bulyk**, Ajeesh Kumar Somakumar, P. Ciepielewski, Yu. Zorenko, Ya. Zhydachevskyy, I Kudrjavtseva, V. Gorbenko, A. Lushchik ,M. G. Brikc, Y. Syrotych, K. Paprocki, A. Fedorov and Andrzej Suchocki, ustne, *International Conference on Oxide Materials for Electronic Engineering – fabrication, properties and application (OMEE)*, Lviv, Ukraine, 28 września – 2 października, **2021**.

2) Appearance of blue luminescence of $CsPbBr_3$ under high pressure, **Lev-Ivan Bulyk**, Ya. Chornodolskyy, T. Demkiv, R. Gamernyk, V. Vistovskyy, A. Suchocki, A. Voloshinovskii, ustne, *LumDeTr*, Bydgoszcz, Poland, 12 – 17 września, **2021**.

3) Conductivity of $CsPbBr_3$ at ambient Conditions, **Lev-Ivan Bulyk**, T. Demkiv, O. Antonyak, T. Malyi, R. Gamernyk, V. Vistovskyy, A. Voloshinovskii, A. Suchocki, ustne, *XXII International Seminar on Physics and Chemistry of Solids (eISPCS'20)*, Lviv, Ukraine, June 17-19, **2020**.

4) Eu^{3+} luminescent centers in RE=Y, Gd, Tb aluminum perovskites under high pressure, **Lev-Ivan Bulyk**, Andrzej Suchocki1, V. Gorbenko, Yu. Zorenko, ustne, *Europhysical Conference on Defects in Insulating Materials (EURODIM)*, Bydgoszcz, Polska, 8-13 lipca, **2018**.

IV. Acknowledgments

I would like to express my deep gratitude to Prof. Dr hab. Andrzej Suchocki for providing me with the opportunity to pursue my Ph.D. in his group and for his unwavering support throughout the years. His conscientious guidance, vast scientific insights, unwavering patience, and valuable comments have been instrumental in shaping my understanding of my research topic and this thesis. I am also thankful for his kindness, constant encouragement, trust in me, and the valuable freedom he has given me.

I am deeply grateful to Prof. Y. Zorenko from Kazimierz Wielki University in Bydgoszcz (Poland) for his encouragement, inspiring suggestions, and productive cooperation which has contributed significantly to this work.

I also extend my heartfelt appreciation to Prof. Mikhail G. Brik for his expertise in theoretical physics and for his highly valuable calculations that have significantly enriched this work.

I am also grateful to Prof. Yaroslav Zhydachevskyy and Prof. Agata Kamińska for their valuable advice and guidance during my Ph.D. study. I appreciate the great help and support they provided me with.

My sincere thanks also go to the present and past members of my group, including Volodymyr Tsiumra, Damian Włodarczyk, Vasyl Stasiv, Yaroslav Zhydachevskyy, Kamil Koroński, Ajeesh Kumar Somakumar, Saranya Narayanan, Syed Shabhi Haider, Piotr Sybilski, Serhiy Kobyakov, Markiyan Kushlyk, and Yongjie Wang, for their friendship, kindness, and support throughout my journey. I cherish the memories we created and the time we spent together.

Also, I would like to express my gratitude to Serhiy Kobyakov for the tutoring and assistance at the beginning of my path as a Ph.D. student. His valuable advice and support were helpful during my research work.

Separate thanks from me go to the OpenAI company for creating the AI. The free version of ChatGPT was used to correct and revise the English language of this work.

Lastly, I extend my gratitude to IP PAS and all the people who have provided me with various forms of support throughout my research, enabling me to conduct my measurements and achieve my goals.

Also, this work was supported by Polish National Science Center programs: 2019/33/B/ST8/02142, and SHENG2 of Poland–China cooperation, project number: 2021/40/Q/ST5/00336.

V. Introduction

This work focuses on the study of two types of perovskites using spectroscopic methodologies. Perovskites are a class of materials with a unique crystal structure and have gained significant attention in recent years due to their potential applications in fields such as solar cells, LEDs, lasers, and scintillation.

The first type of perovskite studied in this work is a class of oxide perovskites ($R\text{AlO}_3$, R represents Gd, Tb, Lu, Y, or a mixture) with potential applications as scintillators. The efficiency of the scintillator depends on various factors such as the symmetry of the luminescent centers and the location of the dopant levels in the band gap. To study these properties, the samples doped with Eu^{3+} and Ce^{3+} ions, which are effective dopants for scintillation applications, are studied.

The second perovskite of interest in this study is cesium lead bromide (CsPbBr_3), which has shown great promise as a material for photovoltaic applications. Despite the popularity of this material in the scientific community, there are still some open questions regarding its photoluminescence properties. In this work, we use low–temperature and high–pressure photoluminescence methods to investigate the origin of the luminescence in CsPbBr_3.

V.1. Perovskite structure

The formula for a perovskite can be represented as ABX_3. In this formula, A and B are cations that are typically metals with different ionic sizes. The X–site can be occupied by haloid or, if occupied by oxygen, the perovskite becomes a complex oxide. Typically, the cations occupy dodecahedral (A–site) and octahedral (B–site) sites, surrounded by either haloid or oxygen ions [1].

The term "perovskite structure" is derived from the mineral CaTiO_3 and can take on different forms such as cubic ($Pm\bar{3}m$), orthorhombic (Amm2), tetragonal (P4mm), rhombohedral (R3m), or even monoclinic (C2/m). The sizes of the A and B cations must be relatively large and have a specific ratio, which is represented in the Goldschmidt factor (as shown in equations (1) and (2)). If these criteria are met, the perovskite will have a cubic structure. However, if the ratio of the radii of the A and B cations deviates from the required proportion, the lattice will deform, leading to a phase with lower symmetry instead of the cubic structure. This is often caused by rotations of the $[\text{BX}_6]$ octahedra. These rotations can also reduce the coordination number of the A cation from 12 to 8. An example of a perovskite is barium titanate, which is known to display all possible symmetries of the perovskite structure, depending on the temperature [2].

The stability of perovskite structures can be evaluated using the Goldschmidt factor, which is represented by the formula:

$$\mathrm{t} = \frac{r_A + r_X}{\sqrt{2}(r_B + r_X)} \tag{1}$$

Here r_A, r_B, and r_X are ionic radii of A, B, and X ions. The Goldschmidt factor, t, calculated from equation (1), predicts the symmetry of a perovskite compound. A value of $t > 1$ results in a hexagonal or tetragonal structure, $0.9 < t < 1$ predicts a cubic structure, $0.71 < t < 0.9$ indicates an orthorhombic/orthohedral structure, and $t < 0.71$ predicts a different structure [3]. The factor was first described by V. M. Goldschmidt in 1926 [4] and is used to evaluate perovskite stability, as well as ilmenite structure [3].

The Goldschmidt factor has been improved in the work [5] with a new modification, resulting in a more accurate calculation of 92% compared to the unmodified version's accuracy of 74%. This new modification is given by the equation:

$$\tau = \frac{r_C}{r_B} - n_A \left(n_A - \frac{r_A/r_B}{ln(r_A/r_B)} \right) \quad (2)$$

Here r_A, r_B, and r_C are ionic radii of A, B, and X ions, n_A is the oxidation state of the A ion. Equation (2) defines perovskites as having $r_A > r_B$ and $\tau < 4.18$ [5]. The definition has been further refined by Toyoto Sato and others, who expanded its application to any ionic compounds [6] and demonstrated its significance in the formation of double perovskites [7].

Perovskites can be grouped into four categories based on the ionic charge of A and B ions:

- $\mathrm{A^{+}B^{2+}X^{3-}}$, or 1:2 perovskites;
- $\mathrm{A^{2+}B^{4+}}X_3^{2-}$, or 2:4 perovskites ($CsPbBr_3$ – studied in this work);
- $\mathrm{A^{3+}B^{3+}X_3^{2-}}$, or 3:3 perovskites (Y/Gd/$LuAlO_3$ – studied in this work);
- $\mathrm{A^{+}B^{5+}X_3^{2-}}$, or 1:5 perovskites.

In addition to regular perovskites, there are also layered, double, and even triple and quadruple perovskites. Layered perovskites are made up of 2D layers of a general formula ABX_3. These layers are separated by intermediate layers that differ from the main layer structure [1].

Double perovskites have an additional ion, C, in their structure. This makes the unit cell two times larger than that of regular perovskites. Double perovskites have the same architecture as regular perovskites, with 12 coordinate A sites and 6 coordinate B and C sites. Two cations are ordered on the B and C sites in a 3D chessboard structure [1].

Summarising: The perovskite structure can be represented as ABX_3. The term "perovskite structure" is derived from the mineral $CaTiO_3$ and can take on different forms such as cubic, orthorhombic, tetragonal, rhombohedral, or monoclinic. The stability of the perovskite structure can be evaluated using the Goldschmidt factor, which predicts the symmetry of a perovskite compound. The Goldschmidt factor has been modified for improved accuracy. Perovskites can be grouped into four categories based on the ionic charge of A and B ions, including 1:2 perovskites, 2:4 perovskites, 3:3 perovskites, and 1:5 perovskites. In addition to regular perovskites, there are also layered, double, triple, and quadruple perovskites. Layered perovskites are made up of 2D layers separated by intermediate layers. Double perovskites have an additional ion in their structure and have a 3D chessboard structure.

V.2. Yttrium aluminum oxide perovskites

Yttrium aluminum oxide can form three distinct structures, which are perovskite, garnet, and monoclinic, and they all remain stable under ambient conditions. There is another hexagonal crystallographic structure that can be formed by the binary system of Y_2O_3 and Al_2O_3, but this structure is extremely rare and unstable [8]. When doped with a transition metal or rare–earth ions, Yttrium aluminum perovskite (YAP) exhibits excellent properties for various optical applications. The specific application depends on the type of dopant ion used. YAP can be synthesized in the form of nano–powder, micro–powder, thin film, or single crystal, and the properties of YAP can also be altered by partially or fully substituting the Y ion with rare–earth ions.

V.2.1. Single crystal films of rare–earth aluminum oxide perovskites

The $RAlO_3$ (*R*AP, where *R* represents Gd, Tb, Lu, Y, or a mixture) compounds are considered promising materials for applications such as scintillation screens in high energy ray micro–imaging [9], dosimetry [10], and others. These materials can be obtained in different forms such as crystals, powder, or single crystal films (SCF) on specific substrates using various synthesis methods. Among these forms, the epitaxial SCF is believed to be the most suitable for micro–imaging applications.

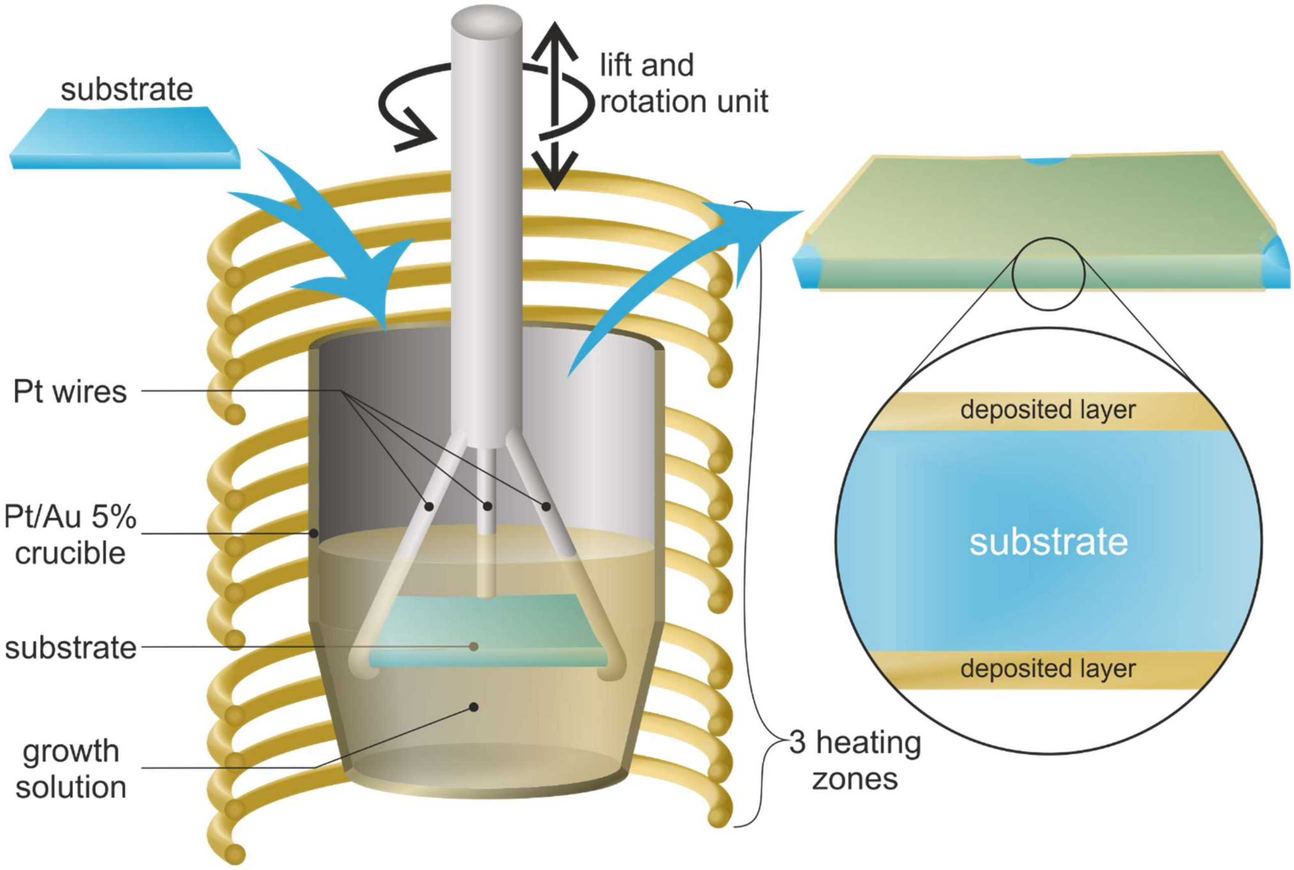

Fig. 1. Liquid phase epitaxy scheme (following Fig. 31.6 from [11])

The thickness of the film is a crucial factor as it impacts the device's performance. To enhance the resolution of the device, the film needs to be as thin as possible, but as the thickness decreases, X–ray absorption also decreases, which reduces the total sensitivity of the device. Thus, an optimal thickness must be determined to balance high resolution and high sensitivity. To achieve this, a thin film with high absorption and effective energy transformation properties must be used. Increasing the X–ray absorption can be achieved by incorporating heavier rare–earth ions, which increases the effective density of the layer. After absorbing the X–rays, the energy must be efficiently converted into luminescence with minimal loss. Therefore, a material with a high light yield (LY) is preferred. Defects in SCFs can influence the LY and either deteriorate or improve it. The impact of defects on *R*AP properties is therefore studied experimentally [12] and theoretically [13].

One of the quickest methods of creating single crystal films (SCFs) is through liquid phase epitaxy (LPE), which is depicted in Fig. 1. During the process, a substrate is placed in a melt and the deposited material is dissolved in the melt, which is kept close to the equilibrium between dissolution and decomposition. The LPE method results in fast and uniform deposition and is much faster compared to molecular–beam epitaxy. It is crucial to choose the appropriate substrate for the synthesis process. To avoid internal tensions, the thermal expansion coefficients of the substrate and precipitated crystals should be similar or equal. Both amorphous and crystalline materials can be used as a substrate. If crystalline materials are used, their lattice parameters should be close or equal to that of the deposited crystal. In this study, YAP (yttrium aluminum perovskite) was used as a substrate due to its wide availability and suitable thermal coefficient and lattice parameters.

V.2.2. Aluminum perovskites doped with Eu^{3+}

The degree of lattice distortion in a material can be monitored by introducing certain dopants. Trivalent europium is a well–known optical sensor of local symmetry. The ratio of the intensities of $^5D_0 \rightarrow {}^7F_2$ and $^5D_0 \rightarrow {}^7F_1$ transitions of Eu^{3+} is often used to quantify this distortion and is referred to as the K–value [14] (although different names for this value are used in different works, this is the most common one). When yttrium in YAP is partially substituted by a different rare–earth ion, the lattice constant of the new material can be changed due to the appearance of so–called "chemical pressure". If the ionic radii of the rare–earth ion used to substitute for yttrium are larger, the resulting pressure is positive. The presence of this pressure results in a change in the local symmetry of the rare–earth ions. In [9], it was demonstrated that the local symmetry in perovskites can be influenced by the ionic radii of the rare–earth ions. This presents an opportunity to exert control over the local symmetry, and thus the luminescent properties, of the material by substituting yttrium with a rare–earth dopant with a specific ionic radius. In solid solutions like $R^1_xR^2_{1-x}AlO_3$, where R^1 and R^2 are two different rare–earth ions, the lattice constant can also be controlled. However, some statistical disorder appears in such materials and needs to be considered, as it can result in the creation of different luminescent centers, luminescence broadening, etc.

Another method of changing the lattice constant is applying hydrostatic pressure using a diamond anvil cell (DAC). In this case, real physical pressure can be changed gradually to adjust the lattice parameters as needed. After achieving the desired properties of the material, real physical hydrostatic pressure can be replaced by its analogous "chemical pressure". Therefore, by performing high–pressure measurements, time can be saved in synthesizing multiple samples, like $R^1_xR^2_{1-x}AlO_3$, with different values of x.

Rare–earth and transition metals are commonly used as luminescent dopants in a wide variety of materials, including hundreds of different compounds [9, 13, 14, 15]. In this work, Eu^{3+} is used as a dopant and symmetry sensor. High–pressure spectroscopy is utilized to investigate the effects of changes in lattice parameters on the local symmetry of the rare–earth in $RAlO_3$.

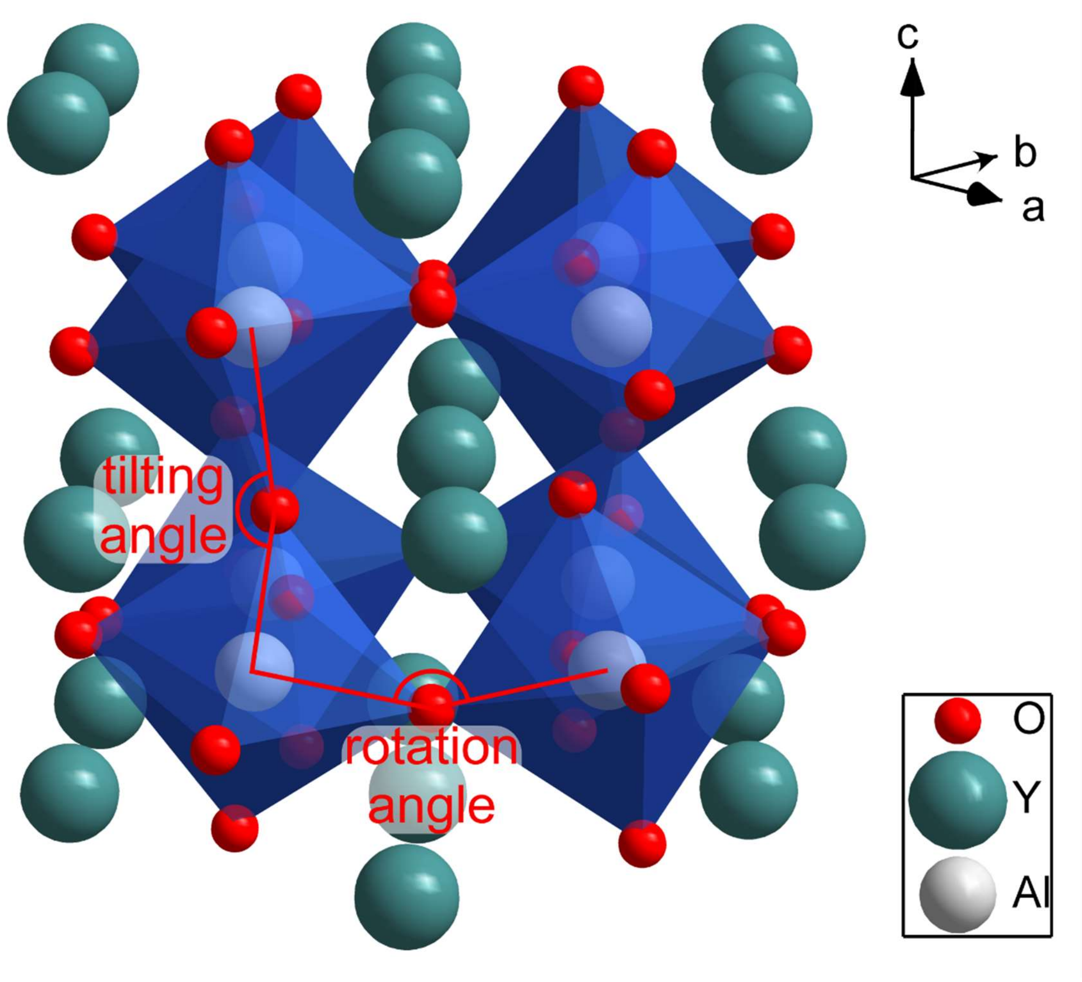

Fig. 2. Perovskite structure of $YAlO_3$ (following [16])

A study of the crystallographic structure of YAP as a function of high pressure is presented in [16]. The structure of YAP is depicted in Fig. 2, following [16]. The authors of [16] report that both rotation and tilting angles increase as the applied pressure increases (see Fig. 2), and afterward, a phase transition occurs at around 80 GPa. GdAP, TbAP, $Gd_{0.6}Lu_{0.4}AP$, and LuAP have similar structures at ambient pressure. Since Eu^{3+} is rare–earth, it likely occupies the position of another rare–earth ion (R) in *R*AP. Therefore, it is assumed that Eu^{3+} possesses D_1 point group symmetry, which lacks an inversion center.

It is well established that Eu^{3+} luminescent transition $^5D_0 \rightarrow {}^7F_1$ is allowed by the magnetic–dipole mechanism, while transition $^5D_0 \rightarrow {}^7F_2$ is allowed by the forced (or induced) electric–dipole mechanism [14]. The relative intensity of these transitions is used to measure local symmetry by Eu^{3+}. Magnetic–dipole transition is present in any local symmetry and serves as a benchmark. In contrast, electric–dipole transition is forbidden for free ions or ions in a site with symmetry inversion. However, if there is some deviation from the centrosymmetric positioning of Eu^{3+}, the electric dipole is induced, and $^5D_0 \rightarrow {}^7F_2$ transition becomes allowed. The intensity of the $^5D_0 \rightarrow {}^7F_2$ transition increases with the formation of a stronger crystal electrical field, which occurs when the deviation from the centrosymmetric position is larger. Therefore, the ratio of $^5D_0 \rightarrow {}^7F_2$ to $^5D_0 \rightarrow {}^7F_1$ transitions, commonly referred to as the K–value, can be used to measure the deviation of local symmetry from the site with inversion [13].

The K–values for the materials studied in this work were previously established at ambient pressure in [9], where the authors also investigated the dependence of K–values on the Lu content in Gd–Lu mixed aluminum perovskite. Their results suggest that K–values are higher for pure LuAP and GdAP, with a minimum value expected for one of the mixed perovskites. Specifically, for $Lu_xGd_{1-x}AP$, the K–value decreases, reaches a minimum, and then starts increasing again as x decreases from 1 to 0. Additionally, since Gd has a smaller ionic radius than Lu, the lattice parameters of the material decrease as the ionic radius decreases. Therefore, conducting high–pressure (HP) measurements provides an opportunity to replace the "chemical pressure" resulting from the partial replacement of Gd with Lu with actual hydrostatic pressure. It is likely that a point with a minimum K–value will be found during these HP measurements. A few perovskite SCFs were selected and studied. The results are published in [17], as well as presented and discussed in this thesis. Intuitively, the dependence of the K–value on the pressure should correlate with the dependence of the K–value on ionic radii.

V.2.3. Yttrium and lutetium aluminum oxide perovskites doped with Ce^{3+}

Yttrium and lutetium aluminum oxide perovskites, $YAlO_3$ (YAP) and $LuAlO_3$ (LuAP), respectively, have been extensively studied as optical materials. Scintillators based on these materials are a prominent application of LuAP, especially cerium–doped LuAP [18], which has a high light yield, high crystal density, and short decay time. Materials with high crystal density are the most suitable for scintillator applications, due to efficient γ–ray absorption. Despite having the same crystal structure and similar properties, LuAP seems to be more promising than YAP for scintillator applications because it is havier, and therefore should absorb γ–ray more effectively. Both materials are also being explored for solid–state laser applications and for a better understanding of their fundamental properties [19, 20].

LuAP is less studied than YAP due to difficulties in the growth process related to non–congruent melting at higher temperatures than YAP. The location of Ce^{3+} states in the band gap of the host is crucial to understanding the mechanisms of $LuAP:Ce^{3+}$ luminescence. Theoretical investigations of Ce^{3+} levels in the YAP band gap have been performed [19], but these results have not yet been confirmed experimentally.

Various growth methods, such as Czochralski, sol–gel, solid–state reaction, liquid phase epitaxy (LPE), and others, can be used to produce both YAP and LuAP. Materials grown by LPE contain fewer defects [21, 22], and in the case of LuAP, LPE is easier to apply than Czochralski because it requires much lower temperatures [23, 24, 25] due to growth from flux. With LPE, single–crystalline films of high structural quality can be grown for use in X–ray micro–imaging applications [25, 26].

Despite their extensive studies and applications, some basic properties of YAP and LuAP remain unknown, such as their accurate band gaps. Doping with Ce^{3+} in these materials is also not well characterized, with Dorenbos' estimations sometimes differing from experimental observations by a few tenth parts of eV [27]. High–pressure studies of these materials have also not been conducted, despite their potential impact on their optical properties. Thus, *this work aims to fill these gaps and provide general observations about the influence of high pressures on the energetic structure of* Ce^{3+} *in various materials.*

V.3. Cesium lead perovskites

All–inorganic metal halide perovskites with the general formula $CsPbX_3$ (X = Cl, Br, I) were first studied about 60 years ago [28]. However, these materials have recently garnered significant interest (see Fig. 3) due to their unique and promising properties, making them attractive for a wide range of optoelectronic applications including photovoltaics, LEDs, photodetectors, laser media, solar cells, and scintillators. One important feature of inorganic perovskites is their higher stability [29] compared to their organic–containing (hybrid) analogs. Through bandgap engineering, perovskites can cover the entire visible spectrum, making them excellent candidates for multi–junction solar cells, LEDs, and laser applications [30].

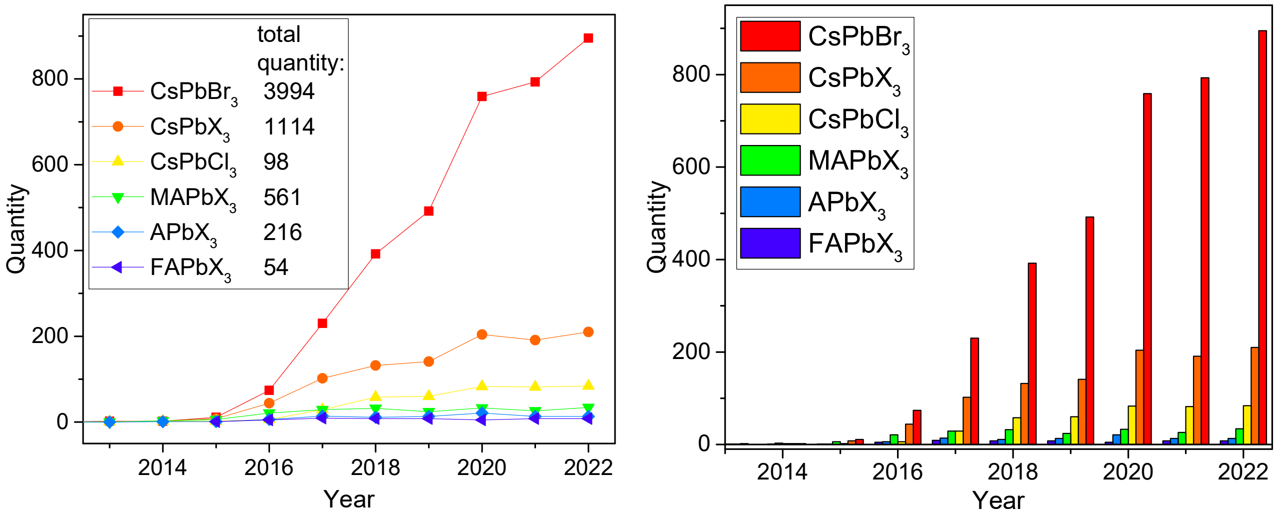

Fig. 3. Scopus search results of articles, searched by "TITLE–ABS–KEY (compound)", where compound = "CsPbBr3", "CsPbX3", "APbX3", "CsPbCl3", "MAPbX3", and "FAPbX3", in the period from 2013 up to 2022. Statistic was created in April 2023

Despite the recent surge in perovskite research, some questions remain unanswered. The role of different types of defects in perovskites and their impact on material properties are not well studied and understood. The origin of luminescence is as well a reason for many debates in scientific society. The luminescence of $CsPbBr_3$ is dependent not only on the size of the crystal (especially in the case of nano–sized particles due to the quantum confinement effect) but also on the quality of the samples [31], density of the excitation power [32, 33], and other parameters. This complexity adds to the challenge of interpreting and identifying the luminescence lines.

To properly implement perovskite materials into various applications, a comprehensive understanding of their properties and mechanisms of formation is necessary. Although hybrid perovskites ($ACsX_3$, where A = MA (CH_3NH_3 – methylammonium), FA ($HC(NH_2)_2$ – formamidinium), X = Cl, Br, I) are known for their superior properties, fully inorganic perovskites have garnered attention for their higher stability at ambient conditions. This has led to high–pressure spectroscopic studies being conducted on these materials. *This work aims to lead to conclusions about the origin of the many–line luminescence of $CsPbBr_3$ at low temperatures by studying the behavior of the luminescence at high pressure.*

The field of solar cell applications is one of the most rapidly evolving and promising areas of research today. According to a diagram created by The National Renewable Energy Laboratory (NREL) in the USA (see Fig. 4), multi–junction solar cells are the most efficient. In a study published in [34], the authors estimated that a triple–junction solar cell device could achieve a PCE of 26.7%. Although the investigation was focused on organic–mixed perovskites, it serves as a good example of the potential implementation of perovskites in the most effective solar cell technologies currently available. The diagram in Fig. 4 also shows the efficiency of perovskite solar cell development over the past few years, which is represented by orange circles filled with yellow.

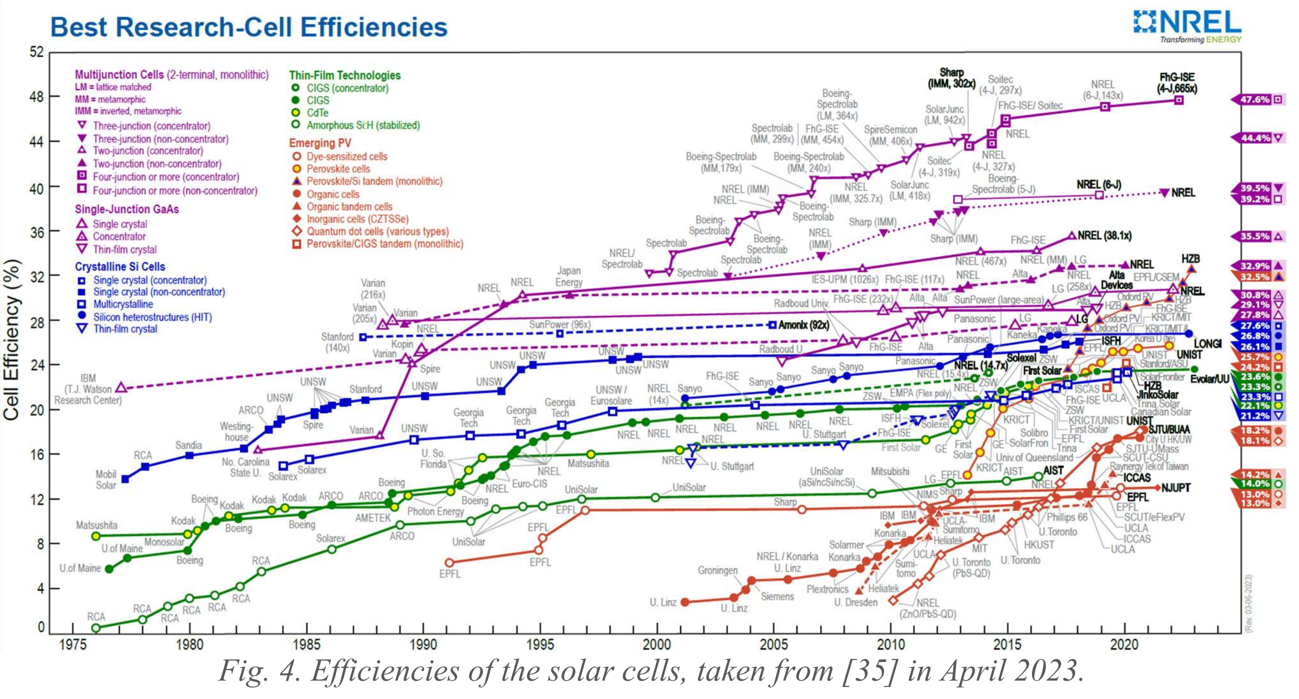

Fig. 4. Efficiencies of the solar cells, taken from [35] in April 2023.

Another promising application for perovskites is in the field of light–emitting diodes (LEDs). The implementation of $CsPbBr_3$ in green LEDs has already been demonstrated in several studies [36, 37]. However, one challenge in improving the quantum efficiency of LEDs is the strong luminescence quenching that can occur at the PEDOT:PSS/$CsPbBr_3$ interface [38]. To address this issue, some researchers have introduced an additional layer of PEDOT:PSS, which has been found to enhance the light extraction efficiency by improving carrier mobility, energy level alignment, and reducing photon loss [38].

Even though $CsPbBr_3$ is more stable than organo–mixed perovskites, it is still prone to interacting with water and undergoing phase changes as a result. Proper storage is necessary to avoid the influence of moisture. Even exposure to humidity in the air can cause phase transition or defect passivation, resulting in changes in luminescence [39, 40]. In a study by Szemjonov et al. [40], the influence of oxygen on the electronic properties of triple–cation perovskites ($FA_{0.79}MA_{0.15}Cs_{0.06}Pb(Br_{0.15}I_{0.85})_3$) was investigated. The authors performed theoretical and experimental investigations of I–vacancies and I–vacancies occupied by O_2 molecules in the material. It was shown that the I–vacancy creates an additional level in the band gap close to the conduction band minimum, while an energetic level close to the valence band maximum is typical for the I–vacancy occupied by oxygen molecules. The authors also found that luminescence intensity is higher when oxygen is present in the lattice. The appearance of additional levels in the band gap suggests the possibility of band gap reduction.

In collaboration with the group from Lviv National University of I. Franko, single crystals of $CsPbBr_3$ were obtained. This scientific group conducted their first study of $CsPbBr_3$ and $CsPbCl_3$ Raman spectroscopy in 1981 [41]. In a subsequent study by Voloshynovskii et al. [42], the luminescence of $CsPbBr_3$ at 14 K was investigated, revealing at least three relatively sharp peaks and one relatively broad peak. The sharp peaks were assigned to the free exciton's transitions and the phonon replica of the free exciton line, while the broad peaks were attributed to excitons localized on defects (details about defect luminescence – will be discussed in chapter V.3.6.2, page 32). The last sharp line was identified as the Rashba exciton (details about the Rashba effect and Rashba exciton – in chapters V.3.5, page 29, and V.3.6.1, page 32).

V.3.1. Structure of $CsPbBr_3$

V.3.1.1. As a function of temperature

The phase transitions of $CsPbBr_3$ with temperature have been well–studied, and it is known to undergo a transition from orthorhombic (62, Pnma or another notation Pbnm) to tetragonal (99, P4/mbm) and then to cubic (221, $Pm\bar{3}m$) as the temperature is increased [43, 44]. This transition is believed to be caused by the condensation of the zone–boundary phonons associated with the rotations of the $[PbCl_6]$ octahedra around the principal axis, leading to a decrease in the space group [45]. Similarly, the phase transitions of $CsPbBr_3$ at 88 and 130°C can be explained by the same mechanism. The condensation of the zone–boundary modes in $CsPbCl_3$ was first mentioned in literature in [46].

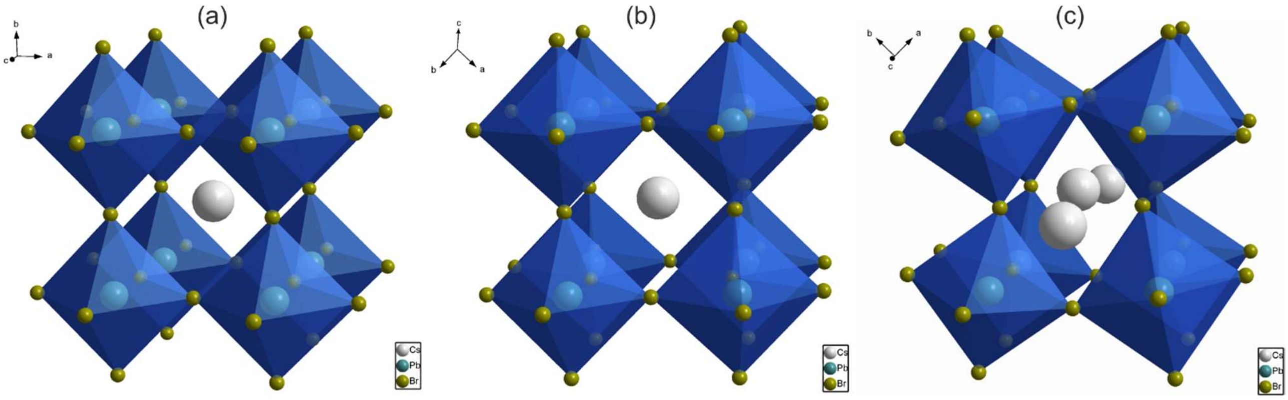

Fig. 5. Crystallographic structure of $CsPbBr_3$ at ambient conditions, where it has orthorhombic Pnma (Pbnm) structure (c), tetragonal P4/mnb (b), and cubic $Pm\bar{3}m$ (a) perovskite structures (present after phase transitions at 88 and 130°C correspondingly).

Different forms of $CsPbBr_3$, such as single crystals and quantum dots, may exhibit phase transitions at different temperatures. For instance, a study on $CsPbBr_3$ quantum dots [47] observed temperature ranges for the first and second phase transitions between 108–117°C and 50–59°C, respectively. The underlying cause for this difference in temperature transitions is not well understood, but it highlights how samples of varying forms can have different properties. Another potential explanation for this phenomenon is the stabilization of the crystal structure by defects, a phenomenon that has been suggested to occur in LuAP (as discussed in chapter VII.2.5.1, page 64).

The first phase transition, from the cubic to tetragonal phase, is a first–order transition, while the second transition, from the tetragonal to orthorhombic phase, is a second–order transition [48, 49]. The structure parameters changing during these transitions also contribute to the differences between the two phase transitions. In the cubic phase (see Fig. 5a), [$PbBr_6$] octahedra are positioned symmetrically and have maximum symmetry.

	SC [43, 44]	QDs [47]
Cubic phase (221, $Pm\bar{3}m$)	>130°C	>117°C
Phase transition (Ist order [48, 49])	~130°C	108°C – 117°C
Tetragonal phase (99, P4/mbm)	88°C – 130°C	59°C – 108°C
Phase transition (IInd order [48, 49])	~88°C	50°C – 59°C
Orthorhombic phase (62, Pnma/Pbnm)	<88°C	<50°C

Table 1. Phase transitions of $CsPbBr_3$ on temperature with types of transitions for different forms of the sample

During the first phase transition, which occurs due to the condensation of the zone–boundary phonons, the [$PbBr_6$] octahedra rotate along one of the principal axes (see Fig. 5b) [45]. This rotation results in a change in the rotation angle from 180° to a smaller value. The rotation angle is defined identically to the rotation angle in YAP (see Fig. 2). During the Ist phase transition, phonons corresponding to the vibrations associated with the rotation of the [$PbBr_6$] octahedra are condensed. In the newly formed phase, different axes are used as the principal axes, which causes the position of the principal axes to differ from that in Fig. 5b.

During the second phase transition, the rotation of the [$PbBr_6$] octahedra increases, and additional tilting and deformation of the octahedra occur (see Fig. 5c). The tilting of the octahedra is related to a change in the tilt angle from 180° to a smaller value. The tilt angle is defined identically to the tilt angle in YAP (see Fig. 2). This transition is associated with the condensation of other types of phonons. In [46], the authors identified the types of the zone–boundary modes as R_{25} and M_3, which condense along the directions {111} and {110}, respectively, leading to the first and second phase transitions.

V.3.1.2. Structure of $CsPbBr_3$ as a function of pressure

Perovskite materials are known to exhibit a variety of phase transitions under pressure. In a study [50], XRD measurements were conducted as a function of pressure for nano–sized $CsPbBr_3$. The results showed that the material had an orthorhombic structure with Pnma symmetry at ambient pressure (see Fig. 5c). As the pressure was increased in the range from 1.2 to 1.7 GPa, the sample underwent a phase transition to a high–pressure phase, which persisted up to the highest (in work [50]) pressure of 15 GPa.

However, a different behavior was observed for $CsPbBr_3$ single crystals under high pressure in a study [51]. The authors measured the high–pressure dependence of Raman and XRD spectra and identified an orthogonal phase with space group Pbnm, which is a different notation of the Pnma symmetry reported in [50, 43]. This phase, named phase I, persisted up to 1.4 GPa, after which an isostructural phase transition occurred to phase II, which existed up to 2.1 GPa. Finally, the sample began to amorphize near 2.9 GPa, and the main Raman peak trace in the vicinity of 72 cm^{-1} became almost untraceable at 10.8 GPa, leading the authors to conclude that the sample had become fully amorphous.

However, in a different study referenced as [52], the authors reported that $CsPbBr_3$ does not undergo amorphization under pressure but instead undergoes a structural phase transition to different types of orthorhombic Pnma structure, which they named Pnma_2. The previous observations of amorphization were explained by the agglomeration of the grain boundaries in powder samples, such as nanoparticles and nanoplates. *These discrepancies highlight the need for further detailed investigations of the phase transitions of $CsPbBr_3$ under pressure.*

V.3.2. The band gap of the perovskites

The properties of materials depend strongly on the band structure of the material. It is important to know the density of states as a function of energy, which states form the conduction band minimum (CBM) and valence band maximum (VBM). Knowing the band structure helps to understand material properties. A combined experimental–theoretical study of metal halide perovskites is presented in [53]. As many works have shown (e.g. [53, 51]), the CBM and VBM are mainly formed by the *p* and *s* electrons of Pb and Br. Therefore, the band gap energy is mostly dependent on the PbBr sublattice and is almost independent of the Cs sublattice. $CsPbBr_3$ has a direct band gap, as reported in many works [44, 50, 43, 54].

Measuring absorption spectra is one of the most broadly used ways to experimentally determine the band gap of a material. The edge of the fundamental absorption in absorption spectra differs depending on the type of band–to–band transition: whether it is direct or indirect, allowed or forbidden. Details can be found in many articles, books, and other literature. For example, in [55], specific relations are derived (equations taken from the same [55]):

- For a direct band gap: absorption is proportional to the square root of the energy of absorbed light:

$$\alpha(h\nu) = \mathrm{A} * \left(h\nu - E_g\right)^{\frac{1}{2}} \tag{3}$$

- For an indirect band gap: absorption is proportional to the square of the energy of absorbed light:

$$\alpha(h\nu) \sim \left(h\nu - E_g\right)^2 \tag{4}$$

These relations are very widely used. Additionally, modifications of these relations, such as Tauc's plots, are sometimes used [56]. Zanatta proposes a new approach to fitting absorption spectra in his work [57]. He fits absorption spectra with equations (3) and (4) for direct and indirect band gaps, as well as with the Boltzmann function. The fitting has been performed for both crystalline and powder samples of Ge, Si, and GaAs absorption spectra. The use of the Boltzmann function is somewhat questionable since there is no physical justification for its use. The main reason it is used is that the results obtained from the Boltzmann function are identical to those obtained using Tauc's plot methods. Furthermore, it is sometimes easier to use the Boltzmann function than the Tauc's plot approach because the absorption spectra and the Boltzmann function have a similar shape.

Therefore, Zanatta proposes fitting absorption spectra with the Boltzmann function given by the following equation:

$$\alpha(E) = \alpha_{max} + \frac{\alpha_{min} - \alpha_{max}}{1 + e^{\frac{E - E_0}{\Delta E}}} \tag{5}$$

Here α_{max} and α_{min} are the maximum and minimum values of the absorption coefficient in the vicinity of the band gap, respectively. E_0 is the energy at which the absorption coefficient is halfway between its minimum and maximum values. ΔE is related to the slope of the sigmoid curve. This approach is completely empirical. Zanatta gives an intuitive interpretation of the parameters from equation (5). For example, E_0 is the point on the Boltzmann function where $d\alpha/dE$ has the highest value, so it can be interpreted as the band gap at 0 K if the density of states in the valence and conduction bands were a step function. Due to the smoothness of the density of states, temperature influence, and other mechanisms (such as blurring related to the Urbach states), absorption is smoothed around E_0. The parameter ΔE is related to the width of the transition region, where the absorption coefficient changes from its minimum to its maximum value (although the maximum value is dependent on the experimental parameters of the measuring system, and is not dependent on the sample properties).

V.3.2.1. Influence of electron–phonon interaction on the band gap width

The band gap of most materials is expected to decrease with the temperature increase due to the electron–phonon interaction. The decrease can be analyzed using equations such as the Varshni equation [58] or the equation proposed by L. Vina et al. [59].

The Varshni equation (6) is based on theoretical arguments, which suggest that the band gap should decrease proportionally to T^2 at temperatures much lower than the Debye temperature (T_D) and proportionally to T at temperatures much higher than T_D [58]:

$$E_g(T) = E_0 - \frac{\alpha T^2}{T + \beta} \tag{6}$$

Vina et al. proposed another approach that adds a term to the fundamental absorption at zero temperature (see Eq. (7)). This term corresponds to band gap shrinking, proportional to Bose–Einstein statistical factors for phonon emission [59]:

$$E_g(T) = E_0 - \frac{2a}{e^{\frac{h\nu_{ph}}{k_B T}} - 1} \tag{7}$$

Although the approaches and mathematical expressions are different, the geometrical shape of both curves is very similar.

V.3.2.2. Linear expansion of the band gap

The temperature dependence of the band gap in the lead–like perovskites, which are perovskites containing lead or other heavy ions with *p*–electrons on the outer shell (such as Sn), is not typical. In many lead–like perovskite materials, it has been shown that the band gap linearly increases with temperature. In some cases, such as $CsPbBr_3$, the linear increase in the band gap continues in specific temperature regions, while in other cases, such as $CsSnI_3$, it was observed for all studied temperature ranges. These results have been reported in experimental, theoretical, and mixed works. For example, in [60], authors have shown linear band gap expansion for $CsSnI_3$, in [61], band gap expansion is predicted theoretically for different phases of $MAPbI_3$, and in [62], band gap expansion is confirmed for $MA/FA/CsPbBr_3$.

Explanations for this behavior can be found in many works, for example [60, 61, 62, 63, 64]. As mentioned earlier in chapter V.3.2, page 20, and in studies [53, 51], the VBM and CBM are mainly formed by *s* and *p* electrons of Br and Pb, respectively. The band gap energy depends on the overlap of the wave functions of Pb and Br electrons, where a higher overlap leads to a decrease in the band gap. This is caused by the antibonding interaction between Pb and Br. The overlap is affected by the structural parameters such as the interionic distance and the angle between bonds. This relationship is schematically shown in Fig. 6, where it is demonstrated that the smaller the interionic distance and the closer the Pb–Br–Pb angle is to 180°, the higher the overlap of the wave functions is, and the bigger the band gap is, due to the antibonding interaction between Br and Pb.

Additionally, from Fig. 5 and Fig. 6, it is clear that the tilting and rotation angles of [$PbBr_6$] octahedra strongly correlate with the Pb–Br–Pb angle (the definition of the tilting and rotation angles is identical to the tilt and rotation angles in YAP, see Fig. 2). Therefore, two main conclusions can be drawn:

- The band gap increases as the distance between the lead–like ion and its neighbors increase (until the ions are too far apart for the wave functions to overlap).
- The band gap decreases as the rotation and tilting angles of [$PbBr_6$] octahedra increase.

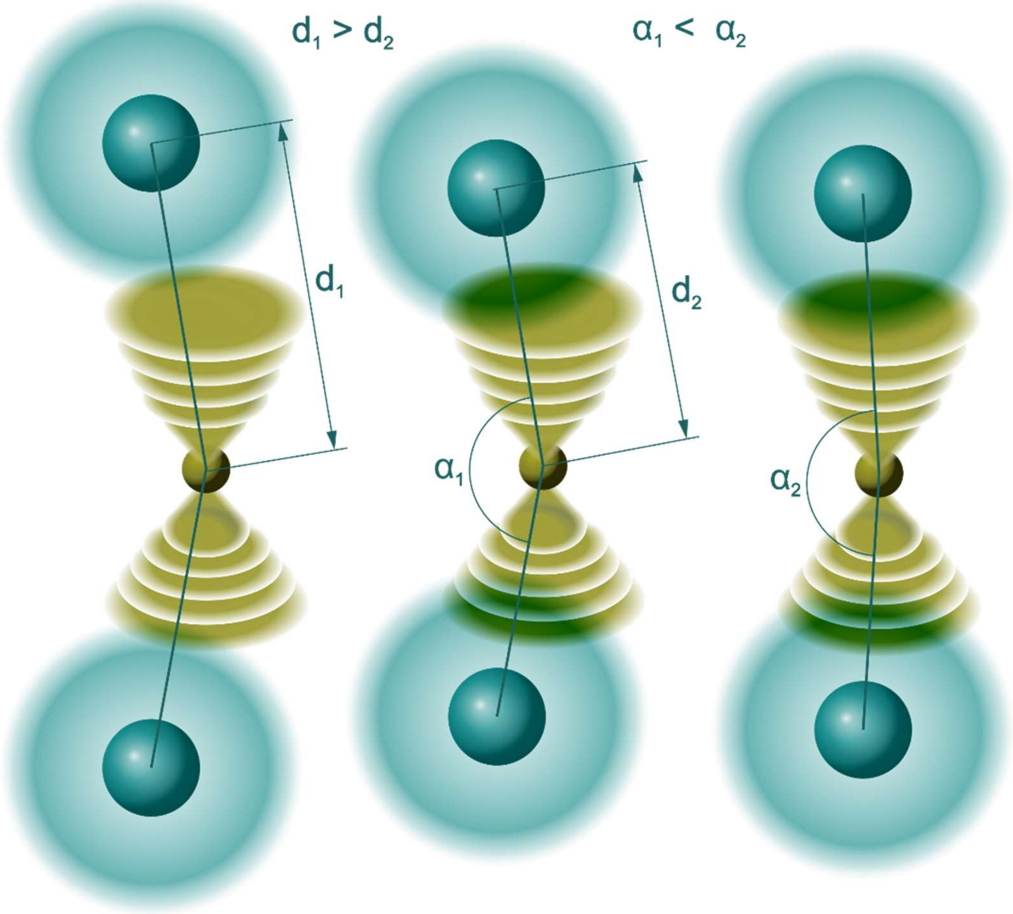

Fig. 6. Demonstrates overlap of the wavefunctions of Pb (bluish spheres) and Br (brownish spheres) electrons, depending on interionic (Pb–Br) distances and Pb–Br–Pb angles (this figure is drawn following Fig. 2 from [63])

In other words, these are the two main structural changes that lead to changes in the band gap. When a phase transition occurs, the interplay between these two factors will cause the band gap to change. Depending on the direction of the parameter change and which change is more significant, the band gap will either increase or decrease.

V.3.2.3. Discussion

The band gap of $CsPbBr_3$ is known to be direct and shows a non–typical dependence on temperature. When studying the band gap dependence on temperature, regular electron–phonon interaction, and a linear expansion that is typical for perovskites (but non–typical in general) should be taken into account. This is done for CsPbBr$_3$ in [65], from which the equation is adopted:

$$E_g(T) = E_0 + BT - \frac{2a}{e^{\frac{h\nu_{ph}}{k_B T}} - 1} \text{ – often used in this form}$$
$$E_g(T) = (E_0 + a) + BT - \frac{2a}{e^{\frac{h\nu_{ph}}{k_B T}} - 1} \text{ – exact equation as in [65]} \qquad (8)$$

Here, E_0 is the band gap energy at zero temperature (unrenormalized band gap); the second term corresponds to the thermal expansion of the band gap with a rate of B; and the third term includes electron–phonon interaction. In the last term, a is the weight of the electron–phonon interaction, $h\nu_{ph}$ is the phonon energy, and k_B is the Boltzmann constant. In [65], equation (8) has one additional term, a, which is added to E_0, and this term takes into account the presence of the phonons at zero temperature.

V.3.3. Structure fluctuation of CsPbBr$_3$

Studies of the local structure of selected organic–inorganic perovskites have shown that the CsPbBr$_3$ lattice can be deconvoluted into three sublattices [66, 67]. The sublattice formed by Pb ions is the most stable in CsPbBr$_3$, while Bromine ions fluctuate around their equilibrium positions much more than Pb ions. Cs ions can be described as free ions, and their motion is confined by the Br$_{12}$ dodecahedra [66, 67]. The schematic representation of the structure fluctuation for CsPbBr$_3$ is shown in Fig. 7. For organic–inorganic perovskites with MA (MA = CH$_3$NH$_3$ – methylammonium) or FA (FA = HC(NH$_2$)$_2$ – formamidinium), the free rotation of the organic molecules was confirmed experimentally back in 1985 by NMR measurement on MAPbX$_3$ crystals [68]. However, in the case of Cs ions, its rotation is irrelevant due to the Cs ion has a spherically symmetrical shape. Despite this, the strong fluctuation of the Cs ions causes significant local structure fluctuation even in CsPbBr$_3$.

In [54], the authors investigate CsPbBr$_3$ using first–principles molecular dynamic simulations and show the distribution of a few lattice parameters in the temperature range of 50 K to 300 K. As the temperature increases, the Pb–Br–Pb angle distribution broadens and becomes asymmetric, which supports the suggestion of increased fluctuation. At 300 K, the percentage of the Pb–Br–Pb angle equal to 180° is already significant. The authors of [54] estimated that the domains with tetragonal phase fraction increased from 0.1 to 0.34 as the temperature increased from 50 K to 300 K, suggesting the coexistence of different fluctuating phases or domain structure with the stable phases in separate domains. These conclusions confirm the important role of dynamic structure fluctuation, as reported in many works (e.g., [66, 67, 68, 69]). Other experimental effects also support dynamic structure fluctuation, including the liquid–crystal duality of CsPbBr$_3$, Urbach states below the band gap, a central peak in Raman spectra, and active Raman signal in high–temperature cubic phase of CsPbX$_3$ perovskites. These effects are discussed in the following subsections.

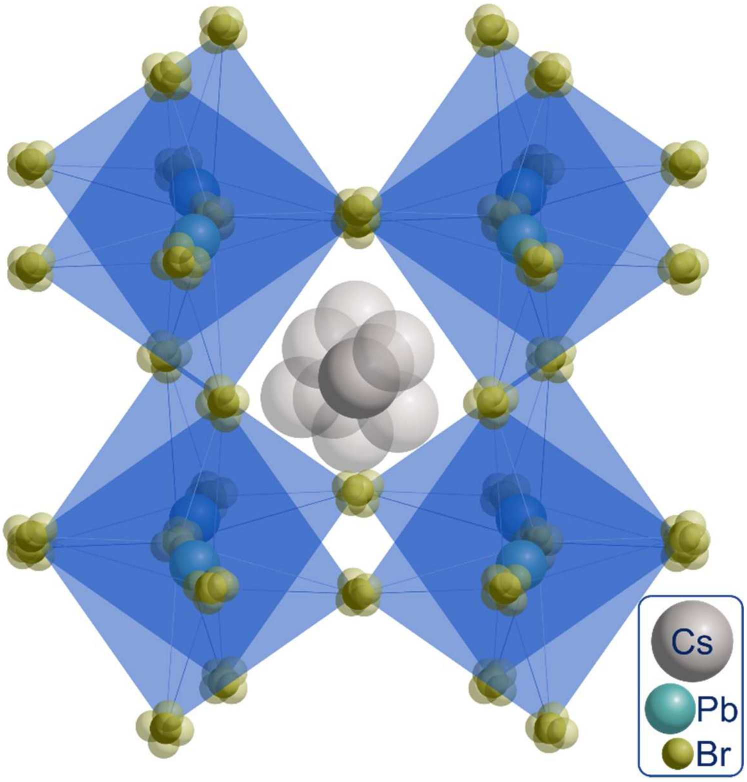

Fig. 7. Schematic visualization of the $CsPbBr_3$ structure fluctuation

It is important to note that structure fluctuation is often referred to as structural disorder. In this work, the term "structure fluctuation" is used to emphasize the dynamic nature of the phenomenon. The structural disorder can also be understood as a static domain structure or an inhomogeneous distribution of defects. In the case of $CsPbBr_3$, structure fluctuation is a dynamic effect related to the fluctuation of the position of Pb and Cs ions (see Fig. 7).

V.3.3.1. Liquid–crystal duality of $CsPbBr_3$

Above, it was mentioned that the lattice of $CsPbBr_3$ can be deconvoluted into three sublattices, with Pb forming the most stable sublattice, Br ions fluctuating around their equilibrium positions, and Cs ions acting as free ions, with their motion confined by Br_{12} dodecahedra. However, when considering the properties of $CsPbBr_3$, it is more appropriate to speak of two sublattices: PbBr and Cs. In the work [69], the authors discuss various properties of $CsPbBr_3$ and suggest that the PbBr sublattice is mainly responsible for electrical transport, while the Cs sublattice (or the A^+ anion sublattice for $FA/MAPbBr_3$) is responsible for heat transport.

Due to the strongly fluctuating Cs sublattice's role in heat transport, it often exhibits liquid–like properties. The liquid–crystal duality of perovskites means, that the solid materials exhibit properties that liquids have. For example, [69] reports that $CsPbBr_3$ has properties, which are indicative of liquid–like behavior.

V.3.3.2. Urbach states

Many semiconducting materials exhibit defect levels below the bottom of the conduction band, which can form a continuous exponential distribution of levels known as Urbach states [55, 70]. The origin of these states can vary, and one possible cause is the structure fluctuation. In $CsPbBr_3$, Urbach states can arise due to fluctuations of the Br ions within the PbBr sublattice, which affects the band gap.

Urbach tails in absorption spectra are well–known features of perovskites. In one study, researchers investigated Urbach tails in $MAPbI_3$ and compared them with those of GaN, GaAs, and InP [71]. In other studies, the Urbach tails of $CsPbBr_3$ were investigated for different forms of the samples [72, 73].

V.3.3.3. Raman activity and a central peak

The Raman activity of $CsPbBr_3$ and similar perovskites has been studied in many works, including [45, 74, 75]. According to [45], for $CsPbCl_3$ (which is structurally identical to $CsPbBr_3$), there are three doubly degenerated TO_i phonons in cubic symmetry. However, if the symmetry is lowered, the degeneracy is lifted, and two separate lines should be visible in the Raman spectrum (as is the case for the orthorhombic perovskite structure). The positions of the $CsPbBr_3$ phonon lines are reported to be 52 and 67, 74 and 81, and 129 and 133 cm^{-1} for the TO_1, TO_2, and TO_3 doublets, respectively [75]. Another relatively weak and broad band around 309 cm^{-1} is also usually reported [45, 74, 76]. This band corresponds to the second order of the LO phonon, located around 155 cm^{-1} [77, 78].

The so–called central peak is another effect observed in Raman spectra, which is caused by structural fluctuations. This peak is a relatively broad band positioned exactly where the excitation laser is [67, 75]. Yaffe et al. reported and explained this peak in their measurement of the low–frequency Raman spectra [67]. It is assigned to the local polar fluctuations in $CsPbBr_3$, which are associated with the structural fluctuations [66, 92]. The intensity of the central peak increases with temperature, and phonons interact with the local crystal field fluctuations [67]. The Raman central peak in $CsPbBr_3$ is caused by head–to–head Cs motion coupled with the perpendicular outward motion of Br [67]. The presence of the zero frequency line in both $MAPbBr_3$ and $CsPbBr_3$ is strong evidence that structure fluctuation is related not only to MA rotation but also to its movement, indicating that $CsPbBr_3$ has properties similar to those of $MAPbBr_3$.

However, in work [79], the central peak is associated with the order–disorder phase transition in $CsPbCl_3$. It is possible to combine these findings by noting that, at low temperatures, the vibrations associated with the central peak are quenched due to the low temperature. As the temperature increases, vibrations of the head–to–head Ce motion, which originates from quantum non-zero-point movement, start to appear, resulting in an increase in the central peak and a putative (although still controversial) order–disorder phase transition. With further temperature increase, the continuous increase of the "central peak vibrations" eventually leads to the first and second phase transitions through the order–disorder mechanism. In other words, the "central peak vibrations" become so strong that $CsPbBr_3$ can be considered to fluctuate among many noncubic phases in a way that appears to be cubic on average.

V.3.3.4. Raman active modes of $CsPbX_3$ cubic perovskite

As mentioned in the previous chapter (V.3.3.3, page 26), the Raman spectra of $CsPbX_3$ perovskites in the cubic phase contain doubly degenerate TO_i phonons [45].

According to factor group analysis, these TO vibrations should be Raman–inactive in the cubic phase of $CsPbBr_3$ [45]. However, both [67] and [75] report Raman activity in the high–temperature cubic phase. In [67], the authors suggest that the perovskite fluctuates among many non–cubic phases at high temperatures in a way that appears to be cubic on average, and the Raman signal comes from non–cubic, fast–fluctuating phases. The full width at half maximum of the $CsPbBr_3$ Raman lines increases rapidly with temperature, providing experimental evidence of this dynamic fluctuation concept.

V.3.3.5. Discussion

In chapter V.3.1, page 25, it was mentioned that the phase transitions of $CsPbBr_3$ at 88°C and 130°C are related to the condensation of the zone–boundary phonons with a decrease in temperature. Additionally, the structure fluctuation of the perovskite is mainly due to $PbBr_6$ octahedra rotation, tilting, and deformation, resulting from a relatively stable Pb–sublattice and a more fluctuating Br–sublattice (as discussed in chapter V.3.3, page 26). Based on these observations, it can be suggested that at low temperatures, $CsPbBr_3$ perovskite has an orthorhombic phase because most of its phonons related to $[PbBr_6]$ octahedra rotation and tilting are “condensed”. As the temperature increases, these phonons start to “evaporate”, leading to an increase in structural dynamic disorder (structural fluctuation), eventually resulting in phase transitions. This suggestion is confirmed by work [47], where it was concluded that orthorhombic to tetragonal and tetragonal to cubic phase transitions occur through order–disorder mechanisms. The [47] study was conducted on quantum dots of $CsPbBr_3$.

The terminology of “condensation” and “evaporation” of phonons is allusive and is used mainly to emphasize the connection between the increase of phonon activity with temperature and the “condensation of the zone–boundary phonons” mentioned in chapter V.3.1.1, page 18, and previous studies [44, 43]. In essence, “condensation” should be understood as the freezing of phonons at low temperatures. For example, if we imagine the rotational vibration of $[PbBr_6]$ octahedra in $CsPbBr_3$, an equilibrium angle of 170° could exist, with the vibration occurring in the angle range from 165° to 175°. “Condensation of the zone–boundary phonons” would then be the disappearance (freezing) of phonons at low temperatures, with the lattice having a new equilibrium angle equal to the boundary condition of the vibration (e.g., 165°). The temperature increase would result in a higher vibration amplitude. The increase of the vibration would cause the lattice to be on average in the phase with an increasing angle (the higher the temperature, the closer the angle to 180°). This model can explain the temperature–related phase transitions of $CsPbBr_3$, its structural fluctuation, Urbach states, Raman activity in cubic $CsPbBr_3$, and the central peak in Raman spectra. However, further theoretical studies are required to refine this naive assumption and build a theoretical framework, which is beyond the scope of this work. Nonetheless, experimental results have been published that provide evidence for this assumption.

In particular, the structure fluctuation of perovskites has been detected not only in organo–mixed perovskites [66, 67, 68] but also in fully inorganic perovskites [54, 67]. Therefore, liquid–crystal duality is present in fully inorganic perovskites and is associated with the A–cation movement, which is associated with the structure fluctuation.

The same structure fluctuation gives rise to the Urbach states below the bottom of the conduction band of the perovskites. Furthermore, this structure fluctuation is responsible for the central peak in the Raman spectra and the active Raman in the cubic phase of the perovskites, where it should be inactive. This provides a good explanation for the fast broadening of the Raman lines with temperature. Regular TO_i phonons interact with the structure fluctuation, and part of the phonon energy is dissipated. Therefore, the fast broadening of the Raman lines with temperature can be explained by the increase of the structure fluctuation with temperature.

V.3.4. The twin domains in perovskites

Semiconductors can contain different types of defects, which can be divided into three main groups: (i) point defects (such as vacancies, interstitials, and antisites), (ii) linear defects (such as dislocations), and (iii) planar defects (such as grain or phase boundaries). Among the defects found in $CsPbBr_3$, point defects have been studied the most thoroughly, including V_{Br}, V_{Cs} (vacancies), Br_i, Cs_i (interstitials), and Pb_{Br} (antisite) [80, 81]. Linear and planar defects have been studied less, but in one study, the domain structure of $CsPbBr_3$ was observed, which is a type of planar defect. Twin domains in $CsPbBr_3$ have been proven to exist in [82] using XRD, POM (polarized optical microscopy), and TEM (transition electron microscopy). Twin domains are domains with the same crystallographic structure but rotated at some angle to the neighboring domains. Similar domains have been studied for mixed–ion lead halide [84] and the review of the metal halide perovskites is done in [83].

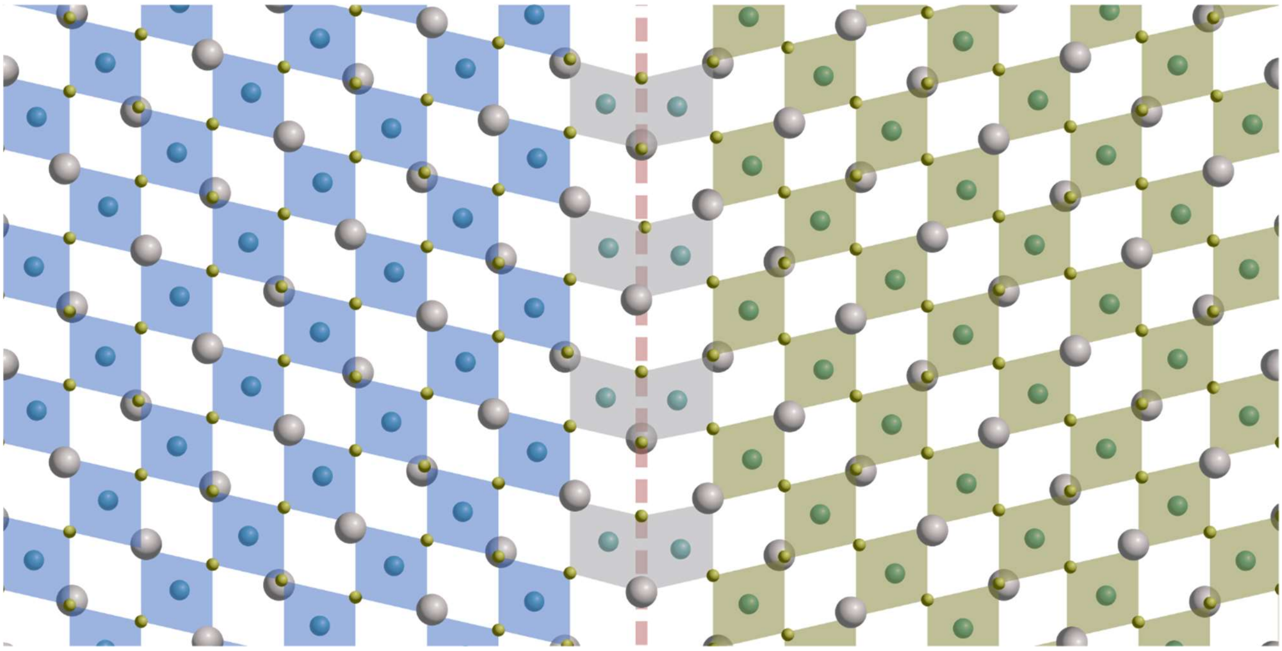

Fig. 8. Schematic picture, that shows the domain structure of $CsPbBr_3$. Two mirror–reflected domains (yellowish and bluish) of the same crystallographic structure are shown with the transition layer between them (gray). The picture was drawn following Fig. 1a from [84]

Therefore, it appears that in $CsPbBr_3$, both domain structure and structural fluctuations coexist simultaneously (regarding the structure fluctuation, see chapter V.3.3). In [47], the existence of domains in $CsPbBr_3$ quantum dots was investigated using synchrotron X–ray diffraction. The authors concluded that the precision of the fit of the data strongly depends on the size of the excited portion of the sample, which is explained by the presence of the domain structure of the sample. According to [84], a general idea of the domain structure of $CsPbBr_3$ with the transition layer between the twin domains is schematically shown in Fig. 8. The domains of $CsPbBr_3$ have the same crystallographic structure, and the only difference is in the orientation of the principal axes. In [82], the authors showed that the two twin domains that are dominant in $CsPbBr_3$ are {121} reflection and 90° rotation around {101}.

V.3.5. The Rashba effect

Emmanuel Rashba, a theoretical physicist of Jewish origin, was born in Kyiv, Ukraine in 1927 (at that time Ukraine was a part of the Soviet Union). He became famous for his works on the effect named after him, which were published in 1959 [85, 86]. These works were published in Russian and are difficult to find on the internet. Therefore, translations of his works have been made available [87] in the supplementary information of a related work [88].

V.3.5.1. General theory, comparison with the Jahn–Teller effect

The Rashba effect and the Jahn–Teller effect share some similarities, but they arise from different origins. The Jahn–Teller effect occurs in molecules or crystals when electrons occupy degenerate energy levels with close or overlapping wavefunctions [89]. This leads to electron repulsion, which deforms wavefunctions and lifts the energetic degeneracy. The result is a loss of symmetry, which is energetically favorable, causing the molecule or crystal structure to change to a less symmetrical form. In solid semiconductors, this lead to a lowering of the band gap and splitting of the bottom of the conduction band in the wave vector space.

In contrast, the Rashba effect occurs in the crystals which have an inversion center, some electrons occupy degenerate states with non–repelling wavefunctions, which do not require any changes to lower the energy. To initiate the Rashba effect, the inversion center must be removed, which can occur through an external distortion, structural defect, or internal imperfection [90]. The removal of the inversion center causes the appearance of ions in the asymmetric crystal electric field, resulting in degeneracy lifting due to spin–orbit interaction [89, 90].

The Rashba effect occurs in ions positioned in sites without inversion symmetry, and it arises from the interaction of the ion's electron with the uncompensated component of the electrical field through spin–orbit coupling. It is more likely to be observed in $CsPbBr_3$, where Pb electron states form the bottom of the conduction band, due to the stronger spin–orbit coupling of ions with larger (see chapter V.3.2, page 20; [51, 53]).

V.3.5.2. Rashba effect in $CsPbBr_3$

The Rashba effect can occur in the vicinity of defects in $CsPbBr_3$, such as Br–vacancies. A schematic representation of this effect is shown in Fig. 9. The inset in Fig. 9a depicts a regular lattice with no defects, where the *p*–orbital of the Br ion has doubly degenerated spin. However, when a Br–vacancy appears in the vicinity, the degenerate *p*–orbital splits due to the spin–orbit interaction in a non–symmetrical electrical field E created by the vacancy, resulting in the split and lowering of the bottom of the conduction band (see Fig. 9b). This split of the *p*–orbital in space gives rise to an additional Rashba line in the luminescence spectra of $CsPbBr_3$. In the ideal structure, only free exciton luminescence should be present in the spectrum. However, with the appearance of distortions, such as Br–vacancies, the Rashba exciton appears.

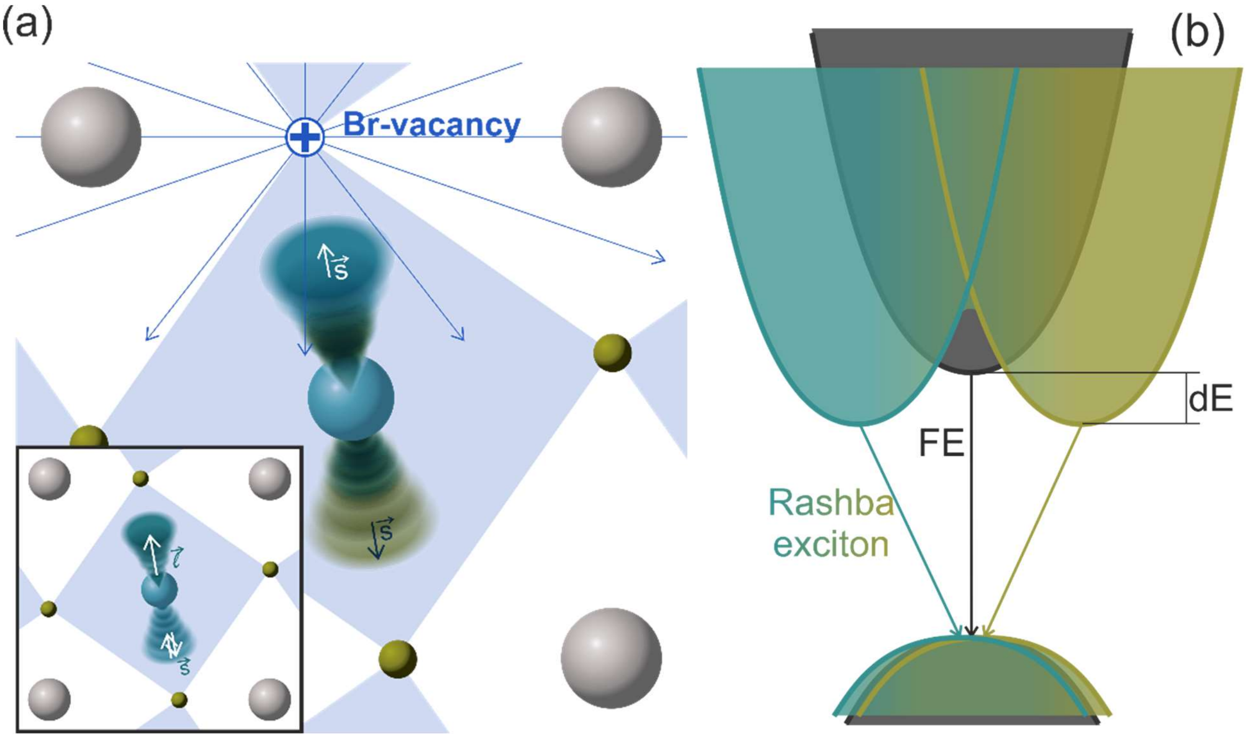

Fig. 9. (a) shows the p–orbital of Br ion, split due to the Rashba effect; the regular undisturbed lattice is shown in the inset, and (b) shows band gap lowering and splitting as a result of the Rashba effect

The intensity of the Rashba line is directly proportional to the concentration of the defects. Therefore, the higher the concentration of distortions, the higher the concentration of Rashba centers and the higher the intensity of the Rashba line. Furthermore, the position of the Rashba line depends on the strength of the electrical field created by the distorted lattice. The stronger the electrical field, the larger the energetic distance between the free and Rashba exciton (signed as *dE* in Fig. 9b).

At low temperatures, the luminescence of $CsPbBr_3$ consists of a few lines, typically two or three. In most interpretations of the origin of these lines, the line with the highest energy is assigned to the free exciton line, and the first or second line from the lower energy side is assigned to the so–called Rashba exciton [42, 92, 91]. There are many different defects present in $CsPbBr_3$, and each one could potentially be responsible for the Rashba centers. The Rashba effect can occur in the vicinity of point, linear, or planar defects, which provides a variety of possible origins. In addition, different types of structure fluctuations can also lead to the formation of Rashba centers.

The Rashba splitting can have either a static or dynamic origin. If the non–symmetrical environment is static, the effect is called the static Rashba effect. On the other hand, if it is dynamic, it is called the dynamic Rashba effect. The static Rashba effect can be caused by Br–vacancies or other static defects, while the dynamic Rashba effect can be caused by structure fluctuations.

In [91], luminescence measurements of $CsPbBr_3$ were conducted using transmissive and reflective geometries. The authors concluded that for $CsPbBr_3$ the Rashba splitting disappears below 50 K. They also observed an increase in the distance between the free and Rashba excitons with an increase in temperature, leading them to conclude that the Rashba effect has a dynamic nature and disappears below 50 K.

However, some works have reported both free and Rashba excitons in the $CsPbBr_3$ luminescence at low temperatures [92, 93]. Given the undeniable experimental confirmation of the Rashba effect in $CsPbBr_3$ (see, for example, [92, 94]), we assume that the mistake in the results of [91] lies in the relatively low resolution of the luminescence spectra and/or in the different approaches used to establish the free and Rashba band gaps. The authors of [91] determined the position of the direct band gap from the position of the free exciton emission because these two values coincide in their case, while they determined the position of the band gap lowered by the Rashba effect from the edge of the luminescence measured in transmissive geometry.

On the one hand, the full disappearance of the dynamic Rashba effect at low temperatures is theoretically acceptable due to the decrease in structure fluctuations, which are likely the source of the dynamic Rashba effect. On the other hand, as described in [88], a dynamic Rashba effect may be present in $CsPbBr_3$ at 0 K, originating from dynamic fluctuations arising from quantum zero–point motion. Nonetheless, the nature of the Rashba effect in $CsPbBr_3$ remains unclear and requires further investigation.

V.3.6. Luminescence as a function of temperature

Around 70–100 K, the luminescence behavior and shape of $CsPbBr_3$ and $CsPbCl_3$ change, indicating the possible presence of a phase transition. In a study [79], $CsPbCl_3$ was investigated using Raman spectroscopy, and the authors concluded that an order–disorder phase transition occurs around 193 K. Based on the similarity between $CsPbCl_3$ and $CsPbBr_3$, it can be assumed that the latter also undergoes an identical phase transition. Another study by [47] found that the high–temperature phase transitions of $CsPbBr_3$ (orthorhombic to tetragonal and tetragonal to cubic) occur via the order–disorder mechanism.

In many works [50, 51, 92, 95], luminescence measurements as a function of temperature are shown only down to 80–90 K, where the luminescence still has the same shape as at room temperature. At lower temperatures, additional sharp lines usually appear. In [42], the origin of these lines is attributed to free excitons, their phonon replicas, and Rashba excitons, with a wavelength change in the low–energy direction. However, there are many other works with different assignments of the luminescence lines. For example, in [96], the luminescence peaks of $CsPbBr_3$ have been assigned to the free, localized excitons and the donor–acceptor pairs (DAP). The debate over the origin of $CsPbBr_3$ luminescence is still ongoing, with various studies proposing different explanations. This topic is discussed in more detail below.

V.3.6.1. Rashba exciton on temperature

Two lines in the $CsPbBr_3$ spectrum are usually considered, and the nature of these two peaks in $CsPbBr_3$ luminescence is controversial, with attempts to explain it having been done in many different ways, using a variety of different effects. In [92], authors mention almost ten possible explanations for the double–peak nature of luminescence. Afterward, the authors investigate the temperature dependence of the luminescence peak's positions and lifetimes. In the conclusions of their work, the authors say that the Rashba splitting effect is the best (if not only one possible) explanation for the double peak luminescence nature. Results of their investigation have revealed imperfections in all approaches but The Rashba effect. Many other studies support the Rashba effect presence in $CsPbBr_3$ [97, 98]. However, the exact nature of the $CsPbBr_3$ luminescence peaks is still controversial, and even if accepting the Rashba effect, it is not clear if it is a dynamic or static Rashba effect. The simultaneous coexistence of both peaks is explained by the coexistence of two luminescent centers: (i) regular orthorhombic lattice with inversion symmetry, and (ii) point, linear, or even planar defects, where inversion symmetry is broken.

The origin of the distortion, due to which the Rashba effect occurs, is a big question too. In work [91], the authors concluded that the origin of the Rashba effect has a dynamic origin for $CsPbBr_3$. With the temperature increase, structure fluctuation increases, as well as the distance between free and Rashba exciton increases, which is an indirect confirmation of the dynamic origin of the Rashba effect.

To further elucidate this matter and deepen our understanding of the fundamental nature of $CsPbBr_3$ luminescence, it would be beneficial to conduct low–temperature and high–pressure luminescence measurements. Such investigations hold the potential to enhance our understanding of the origin and behavior of the $CsPbBr_3$ luminescence.

V.3.6.2. Defect luminescence on temperature

At low temperatures, $CsPbBr_3$ exhibits multiple lines and a band in its luminescent spectrum. In [42], the authors concluded that a broad band above 542 nm (with a maximum position around 560 nm) has a defect origin, but the specific type of defects responsible for this band was not identified. Another research group investigated $FAPbI_3$ and attributed a similar broad luminescence band below the free exciton to an exponential distribution of states below the band gap, resulting from structure fluctuations [99]. Given the similarities between the broad bands observed in $FAPbI_3$ and $CsPbBr_3$, it is worth investigating the possibility of defect formation in $CsPbBr_3$ due to structure fluctuations.

In a separate study, [99], authors demonstrated that defect band luminescence is typically asymmetrical, and its decay time increases as the emission wavelength increases within the band itself. These are key properties that can help identify the defect luminescence band with an exponential distribution of states. Other indicators of this band include temperature and excitation power density, which are dependent on the defect band.

Furthermore, the authors of [99] suggested that the most prominent candidate for the structure fluctuation in $FAPbI_3$ is the rotation of FA molecules. However, since the Cs ion in $CsPbBr_3$ is spherically symmetrical, its rotation is irrelevant. Nonetheless, structure fluctuations in $CsPbBr_3$ can arise from other sources, such as Cs head–to–head motion (as discussed in chapter V.3.3, page 24). Therefore, it is important to investigate the sources of structural fluctuations in $CsPbBr_3$ to better understand the nature of defect luminescence in this material.

V.3.7. Luminescence as a function of high–pressure

Several measurements of luminescence as a function of pressure have been conducted [50, 51, 95]. All of them suggest that the luminescence of $CsPbBr_3$ disappears in the pressure range of approximately 2 GPa. Most of the results indicate a shift of the luminescence towards lower energies with increasing pressure up to around 1 GPa, and towards higher energies with further pressure increases [50, 51]. This behavior of the luminescence peak correlates with the dependence of the $CsPbBr_3$ band gap on pressure. In [64], the authors performed a first–principles study of the atomic and electronic structure of halide perovskites. They showed that the band gap reduces below 1 GPa and further expands with increasing pressure. These changes occur due to the same mechanisms described in chapter V.3.2.2, page 22 for the band gap expansion with increasing temperature. With increasing pressure, the Pb–Br distance and Pb–Br–Pb angle decrease. At pressures below 1 GPa, the reduction of Pb–Br distance dominates over the Pb–Br–Pb angle decrease, resulting in band gap closure. After 1 GPa, it becomes increasingly difficult to compress the lattice further, resulting in slower reductions of the Pb–Br distances. This indicates an isostructural phase transition where the material's phase remains the same, but structural parameters change differently. As a result, after 1 GPa, the reduction of Pb–Br–Pb angles dominates over Pb–Br distance reduction, resulting in the band gap increasing.

Another interesting finding is presented in [51]. In this work, the authors showed that as amorphization begins in the pressure range from 2.0 GPa to 2.5 GPa, the band gap rapidly shifts from ~520 nm to ~440 nm. Up to the highest pressure reached in [51] – 11 GPa, the band gap continues to shift towards higher energies. Similar results were obtained in investigations of $CsPbBr_3$ nanocrystals [100]. Considering the blue shift of the band gap, it can be assumed that under high pressures and UV excitation, $CsPbBr_3$ may exhibit blue luminescence. As shown in some works (e.g., [101]), nano–sized samples of $CsPbBr_3$ do exhibit luminescence in the blue region due to the quantum confinement effect. If the blue luminescence of $CsPbBr_3$ is observed under high pressure, its origin would be an interesting question.

Moreover, the behavior of the double peak studied in [92] has not yet been studied as a function of pressure. This means that *the luminescence of the Rashba and free excitons as a function of pressure has not been sufficiently studied. Comparing the behavior of free and Rashba excitons as a function of pressure may help to clarify the origin of the Rashba exciton.*

V.3.8. Luminescence as a function of the density of the excitation power

As mentioned previously, the luminescence of $CsPbBr_3$ depends on the power density of the excitation light, making it challenging to interpret the spectra. However, this dependence can also be a useful tool to distinguish between different lines in the spectra and facilitate their study.

To effectively study the various changes in the $CsPbBr_3$ spectra, it is important to resolve the luminescence lines. This can be achieved through low–temperature measurements due to the smaller half–width of the lines and temperature quenching of some lines. For example, in a study by [33], two peaks in the luminescence of $CsPbBr_3$ were observed at temperatures below 80 K. By conducting an excitation power study of the lines, the authors concluded that the sharper peak with higher energy (around 540 nm) originates from free excitons, while the broader peak with lower energy (around 550 nm) originates from excitons localized on some defects (from defect band). As the temperature increased, the defect band quenched rapidly and disappeared completely around 80 K, which is consistent with other works (e.g., [42]). Although the reason for the different positions of the free exciton (540 nm in [33] and 534 nm in [42]) is not clear. The general temperature and excitation power dependence of the luminescence correlates with the study [99], where defect luminescence is studied in great detail for $FAPbI_3$. In [99], the authors attribute the origin of the defects to the band with the exponential distribution of the defect levels under the bottom of the conduction band.

In another study [32], the $CsPbBr_3$ sample was excited with a higher density of the excitation power, than in above mentioned works. The authors reported the appearance of two additional lines in the luminescence with lower energy than the one that was present initially. At low excitation power, a line around 527 nm was present at 100 K, which was assigned to the recombination of free carriers. This assignment is controversial, and this line can be as well assigned to the free exciton emission, taking into account the shifting of the free exciton line reported in [42]. Nevertheless, authors of [32] showed, that with the excitation power increase additional lines around 540 and 550 nm appeared. They were assigned to free exciton and bi–exciton emissions, respectively, but their origin is controversial.

In summary, the luminescence of $CsPbBr_3$ should exhibit three main lines: free exciton, exciton localized in the Rashba minimum created by some structure imperfections (static, like point defects such as Br–vacancies or planar defects like domain walls, or dynamic, like structural fluctuations), and exciton localized on defects that form an exponential distribution of states below the conduction band minimum. Some of these lines, or all of them, may also have phonon replicas, the intensity of which would depend on the strength of the particular phonon interaction with the corresponding quasi–particle (free exciton, Rashba exciton, or localized exciton). The bottom of the conduction band with the luminescent transition is shown schematically in Fig. 10. However, the exact type of defects that create the Rashba minimum or form an exponential distribution of levels is still not clear. Additional luminescence lines of yet another origin, bi–excitons, are expected to appear if the excitation power density is high enough.

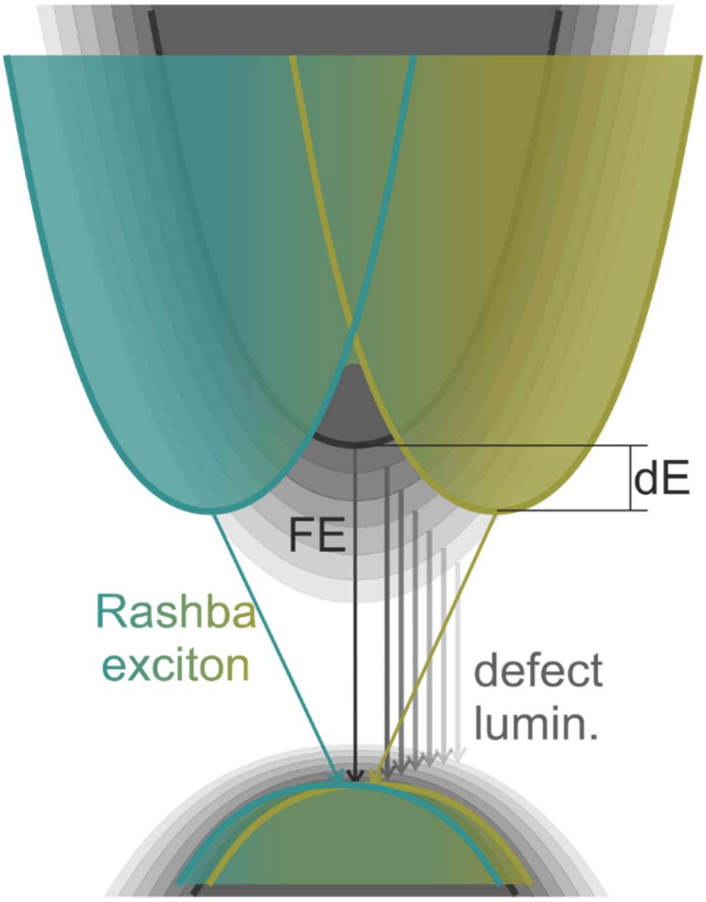

Fig. 10. Schematic picture, showing different types of the bottom of the CsPbBr₃ conduction band, from which luminescence may occur. Free exciton, Rashba exciton, and defect luminescence are schematically shown with arrows. Figure partially follows figure 4 from [92]

V.4. The goals of the work

The main goals of this work can be outlined as follows:

- Conduct a study of the luminescent site of the Eu^{3+} ion in $R\mathrm{AlO}_3$, which includes analyzing the dependence of the K–value (the ratio of the intensities of $^5D_0 \rightarrow {}^7F_2$ and $^5D_0 \rightarrow {}^7F_1$ transitions of Eu^{3+}) on pressure. Profound knowledge of the Eu^{3+} site symmetry will provide information on which $R\mathrm{AlO}_3$:Eu^{3+} are more promising and how to synthesize better ones.

- Investigate the influence of high pressure on the Ce^{3+} luminescence in perovskites. This will help to determine the position of the Ce^{3+} levels in the band gap structure of the host and provide a better understanding of the luminescence properties of these scintillators. It will also offer numerical experimental confirmation and modification to the theoretical Dorenbos model.

- Conduct additional research on the origin of the $CsPbBr_3$ luminescence, which despite being studied in detail, still has many unanswered questions. Conducting low–temperature high–pressure measurements of the $CsPbBr_3$ will provide a better understanding of the luminescence processes in the material and clarify the origin of the Rashba effect. Additionally, studying the high–pressure amorphization of the perovskite, the influence of mechanical treatment, and the influence of the power density of the excitation light on luminescence will help to understand the origin of the $CsPbBr_3$ luminescence.

VI. Experimental techniques

VI.1. Growth of the samples

VI.1.1. Rare–earth aluminum oxide perovskite

VI.1.1.1. Doped with Eu^{3+}

Perovskite SCF RAlO$_3$ (R = Gd, Tb, Lu, Gd$_{0.6}$Lu$_{0.4}$ or Y) doped with Eu^{3+} were synthesized using the LPE method and studied in this work. The samples were grown from the melt solution based on the PbO–B_2O_3 flux. All samples were grown on a YAP substrate with a specific orientation for each rare–earth ion to minimize lattice constant discrepancies. For YAP and TbAP SCF samples, substrates with (100) orientations were used, and for $Gd_{0.6}Lu_{0.4}AlO_3$ ($Gd_{0.6}Lu_{0.4}$AP), $LuAlO_3$ (LuAP) and $GdAlO_3$ (GdAP), (001) orientations were used. The substrate thickness was about 500 μm in all cases, and the thickness of the SCFs varied in the range of 4 to 12 μm. Due to the relatively large thickness of the SCFs, it was assumed that there were no internal tensions in the grown layers, and therefore their luminescent properties should be independent of thickness. Reagents of 4N purity were used for layer preparation, and the growth procedure and initial characterization of obtained samples were described in [9] by Gorbenko et al., from whom the samples were obtained.

VI.1.1.2. Doped with Ce^{3+}

Bulk crystals of YAP and LuAP studied for Ce^{3+} doping were grown by Czochralski and micro–pulling–down (μ–PD) methods. The Ce concentration was equal to 0.2%, 0.5% in YAP, and 0.15% in LuAP single crystals.

Ce^{3+} doped LuAP single crystalline films were grown by LPE on (001) oriented YAP substrates using a melt solution containing Lu_2O_3 (5N), CeO_2 (5N), and Al_2O_3 (4N) and a PbO–B_2O_3 (5N) flux. The growth temperature was in the 1020–1035°C range. The CeO_2 content in the melt was 20 mol%, however, microanalysis of the films has shown that the Ce concentration was only equal to 0.055 and 0.05 mol% at 1020°C and 1035°C growth temperatures, respectively. Thus, the estimated segregation coefficient of Ce ions in LuAP SCFs lies in the 0.0025–0.005 range. The concentration of Pb (from the flux) and Pt (from the crucible) impurities in the layers were estimated to be in the 50–60 ppm range, respectively, i.e., below the 10 ppm level reported in [102]. The optically and structurally perfect SCF sample, with about 22 μm thickness, was chosen for high–pressure investigations of the Ce^{3+} luminescence.

VI.1.2. Cesium lead bromide

Synthesized from the melt, $CsPbBr_3$ single crystals were grown using the vertical Bridgman–Stockbarger method. CsBr and $PbBr_2$ reagents of 99.99% purity were used as raw materials. Before the growth, the reagents were preliminarily cleaned using the zone melting method. A preliminary study of the obtained $CsPbBr_3$ was done by Dendebera et al. [42], from whom samples were obtained.

In another synthesis method, $CsPbBr_3$ crystals were synthesized from a solution. This was achieved by dissolving 0.02 mole of CsBr and 0.04 mole of $PbBr_2$ in 5 ml of dimethylformamide. To dissolve the reagents properly, the mixture was treated with ultrasound for 10 minutes. The solution was then left motionless for 30 minutes to allow some big undissolved parts to settle, after which the undissolved parts were filtered out. The solution was slightly heated to speed up the evaporation of the dimethylformamide. With the increase of the solution concentration, small crystals of $CsPbBr_3$ started to form. The dimensions of the crystals were about 1 mm, and the synthesized material had the appearance of bright brown sugar.

VI.2. Sample preparation for high–pressure measurements

For high–pressure measurements, the samples were polished to a thickness of about 25–28 μm. For bulk samples, both sides were polished, while for SCF on substrates, only one side was polished. During polishing, a mixture of diamond or aluminum oxide powder with water was used, with different size particles depending on the sample. For hygroscopic samples such as $CsPbBr_3$, which were prepared for DAC loading, they were either chopped or polished using a completely dry diamond powder.

VI.3. Measurements of luminescent properties

VI.3.1. Equipment, used at the IF PAN

Luminescence and optical studies were performed at the Division of Physics and Technology of Wide–Band–Gap Semiconductor Nanostructures, IF PAN. In our group's lab (ON4.1), we have access to various types of equipment for spectroscopic characterization, including:

1. Carry 5000 UV–Vis–NIR spectrophotometer
2. Horiba/Jobin–Yvon Fluorolog–3 spectrofluorometer with:
    a. various types of detectors:
        i. Hamamatsu R928P photomultiplier for UV–visible range
        ii. Hamamatsu R2658P photomultiplier for UV–vis–NIR range
    b. Optical cryostat Janis ST–100
3. Set–up for Raman spectroscopy Mono Vista CRS+ with three lasers: 785 nm, 532 nm, and 325 nm
4. Three set–ups for high–pressure fluorescence measurements at UV–Vis–NIR spectral regions
5. Four low–temperature diamond anvil cells (DAC) CryoDAC LT provided by easyLab Technologies Ltd. Diamonds, which we use have 0.45 mm, 0.75 mm, and 0.9 mm culets.

In the Raman set–up, lasers with wavelengths of 325 nm, 532 nm, and 785 nm can be focused on the sample through long working distance objectives with 50x (numerical aperture NA = 0.9) and 10x (NA = 0.23) magnification for experiments at ambient pressure. Objectives with 5x (NA = 0.13) and 5x (NA = 0.08) were used during high–pressure measurements.

For low–temperature measurements, one of four cryostats was used. Three of them were provided by Oxford Instruments, with temperature controllers, and one was from Janis Research Company (it is always used with the Jobin–Yvon Fluorolog). The most often used cryostats, provided by Oxford instruments, were the continuous flow cryostats CF102, CF200, and CF1204. The temperature was controlled using a temperature controller ITC–4, provided as well by Oxford Instruments. In addition to the cryostats, the Linkam Science FTIR600SP/3 device could be used for high–temperature spectroscopic measurements. The temperature range covered by this device extends from liquid nitrogen temperature up to 600°C. It can be used both with Raman and Fluorolog spectrometers, allowing for the measurement of high–temperature Raman spectra and high–temperature luminescence.

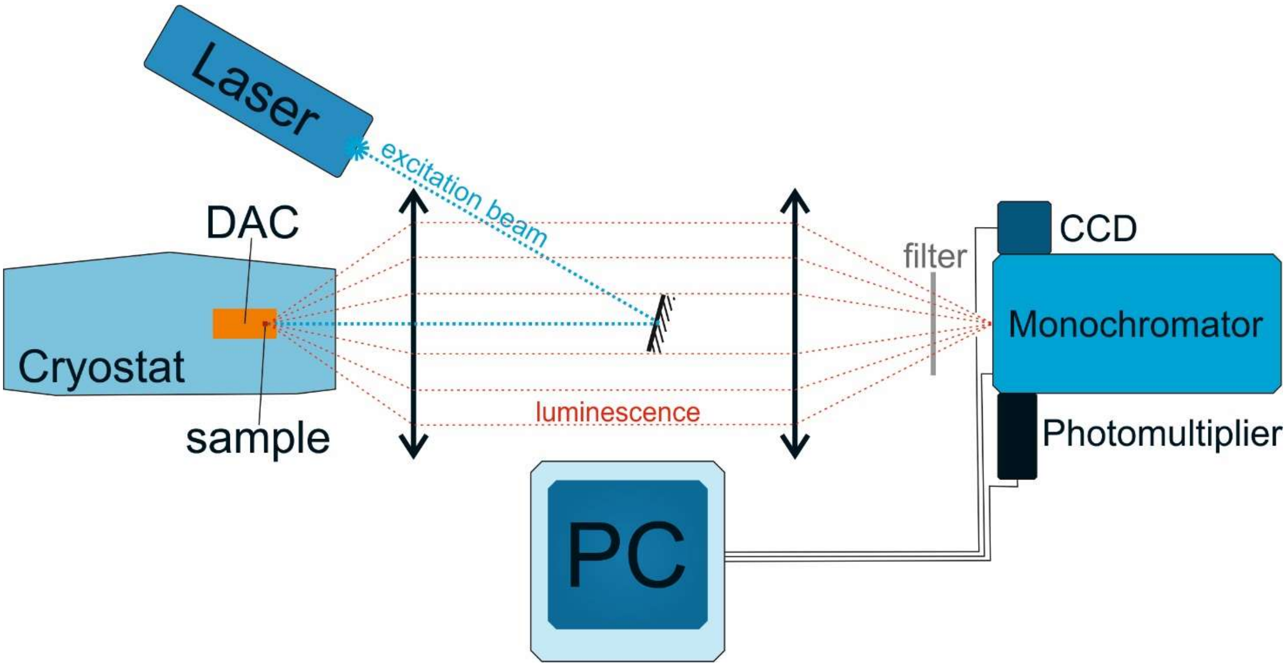

Fig. 11. A schematic picture of the typical set–up for high–pressure luminescence measurements.

High–pressure measurements are performed using set–ups built in backscattering geometry. A schematic of such a set–up is shown in Fig. 11. Different lasers can be used for excitation during high–pressure measurements, such as the Inova 400 Ar–ion laser (which generates wavelengths from 275.4 nm up to 514.5 nm), 325 nm from He–Cd laser, and several semiconductor lasers (405 nm, 440 nm, 532 nm, etc.). DPSS microchip pulse laser with 355 nm, 267 nm, and pulsed EKSPLA Nd:YAG laser with NT342 series optical parametric oscillator (OPO) can be used for kinetics measurements. The emission wavelength of the laser with OPO can be adjusted in the range from 210 nm up to approximately 2 μm.

If low–temperature (LT) measurements are required, the sample can be loaded into a cryostat after being mounted on a cold finger. Both room temperature (RT) and

LT high–pressure (HP) measurements can be done as well. If luminescence spectra are measured, a CCD camera is usually used to collect the signal, while a photomultiplier is used for decay kinetics measurements.

Information about the equipment available in the laboratory can be found at this address: http://info.ifpan.edu.pl/Dodatki/WordPress/on41pl/?page_id=9. Collaborating laboratories in the Institute of Physics, PAS, can provide access to additional characterization techniques, such as EPR, chemical analysis, and electron microscopy.

VI.3.2. Description of the equipment from other institutions

The optical absorbance spectra of YAP and LuAP were measured using a JASCO V 660 spectrophotometer with a double monochromator capable of measuring energies between 1.5 and 6.5 eV, as well as a laboratory setup that included a vacuum monochromator (VMR–2) and a hydrogen discharge light source capable of measuring energies between 5.5 and 11 eV. This equipment enabled us to measure absorption spectra in UV and vacuum UV (VUV) ranges. In the latter case, we achieved a constant number of exciting photons by varying the slit width of the monochromator and using the constant signal from sodium salicylate for normalization. These measurements were performed by I. Kudryavtseva at the Institute of Physics, University of Tartu in Estonia.

VI.4. Diamond anvil cell and high–pressure measurements

VI.4.1. Hydrostatic pressure and DAC’s history

Diamond anvil cells (DAC) provide quasi–hydrostatic conditions for high–pressure (HP) measurements, making them a powerful tool for studying phase changes and structural properties, and for predicting future synthesis. If a sample undergoes a phase transition under HP that results in desirable properties, different conditions or thin film deposition technologies can be used to synthesize samples with the HP–phase at ambient conditions.

From 1910–1950, high–pressure measurements were carried out in Bridgman cells, with the most commonly used devices being Bridgman anvils and piston–cylinder devices. These technologies allowed scientists to reach pressures of up to 10 GPa. Later, Drickamer and his colleagues developed diamond anvils, which enabled high–pressure resistance, XRD, and spectroscopy measurements, pushing the pressure limits up to a few tens of GPa.

DACs have been in use for more than 60 years, and have developed into a widely used high–pressure hydrostatic pressure device. The first spectroscopic measurements in DACs were performed in the IR (infrared) region in 1959 [103]. Due to its relative simplicity and small size, the DAC is convenient for manual usage. This device can reach hydrostatic pressures of up to 100 GPa, with a maximum absolute pressure of 400 GPa explained by the maximum strain that diamonds can withstand. To increase these pressure limits, toroidal diamond anvils were used in [104], and a few other similar high–pressure technologies have allowed for reaching pressures in the tera–pascal range.

VI.4.2. Modern DAC technology

The diamond anvil cell (DAC) is a powerful tool for measuring high–pressure conditions up to 100–200 GPa, with the possibility of reaching pressures up to 770 GPa. The DAC consists of two opposing diamonds that are compressed against each other with their polished tips, which are named culets. The sample is placed between the diamonds, and to obtain hydrostatic pressure, it is immersed in a pressure transmitting medium (PTM), which can be a liquid, gas, or sometimes a soft solid material. The sample, PTM, and pressure sensor are enclosed between the diamonds by a metal gasket. The pressure sensor can be made of any material with a well–known pressure dependence of one of its properties, such as ruby, whose fluorescence lines R_1 and R_2 are well–studied [105].

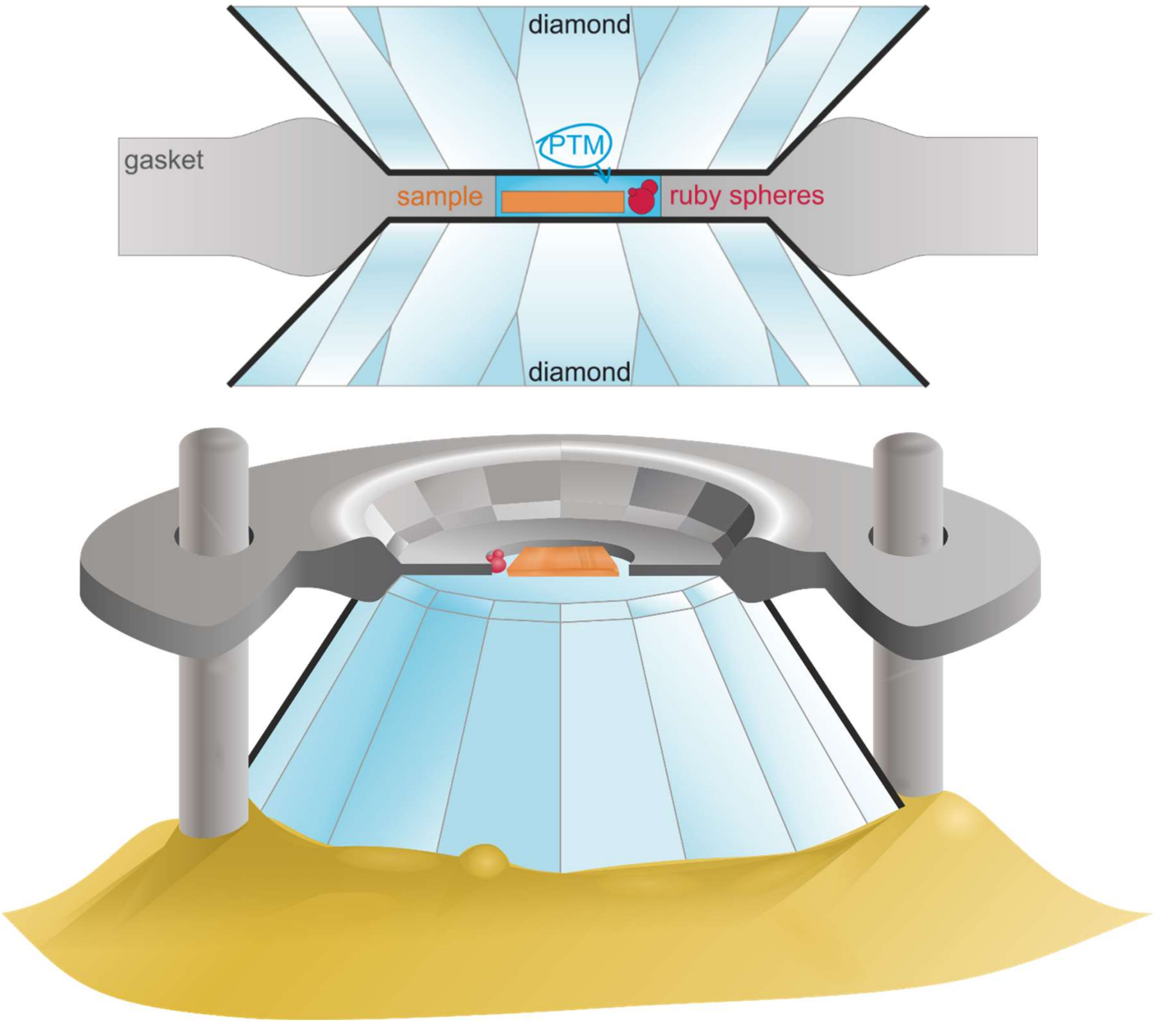

Fig. 12. A schematic representation of the diamond anvil cell (DAC) with a loaded sample and ruby spheres as the pressure sensor.

Nowadays, a sub–millimeter–sized sample can be characterized in great detail at pressures up to 100 GPa. Diamond is transparent over a wide spectral range, from infrared to visible and ultraviolet light, making it possible to use light as the excitation in DAC sample measurements [106]. XRD measurements of the sample placed between the diamonds are also possible.

To perform high–pressure measurements under hydrostatic conditions, the sample is immersed in a PTM, which must be carefully chosen as not all liquids transmit pressure hydrostatically, and some may solidify under high pressure, causing hydrostaticity loss. Inert gases, such as helium or argon, are commonly used as PTMs. To load DAC with these gases, it is immersed into the gas, and the system is cooled down to or below the condensation temperature while maintaining gas pressure. After the gas is liquefied, some pressure is applied to prevent PTM from escaping the cell during its heating up to room temperature. In some rare cases, solid substances, such as NaCl, can be used as PTMs. Solid PTMs are usually used during electrical measurements, where the sample is pressed with the solid PTM to the contacts.

The PTM is enclosed in a hole made in the gasket and placed between the diamonds during measurements. Gaskets are typically made of hard materials like CuBe, W, or stainless steel. During the measurement, the gasket is usually plastically deformed, so the sample should be thinner than the gasket to prevent issues with measurement readings or even the destruction of the diamond anvils. When the gasket becomes too thin, the diamond alignment becomes more crucial, and even small deviations from the perfect alignment can impact the measurement's accuracy. If the gasket is compressed to a thickness smaller than the sample, diamonds start pressing directly on the sample, and pressure is non–hydrostatic, making those measurements incorrect and incomparable with previous hydrostatic readings.

VI.4.3. Some technical observations about the DAC

Fig. 13 shows the dependence of pressure in the cell on the pressures on the driver during different measurements over a period of five years. The measurements were performed using several diamond anvil cells that were built identically but were slightly different devices. These were the CryoDAC LT low–temperature diamond anvil cells provided by easyLab Technologies Ltd., which had diamonds with culets diameters of 0.45 mm, 0.75 mm, and 0.9 mm. To differentiate between the cells, they were labeled I, II, III, and IV, which will be used in this chapter. Since there may be differences between the cells due to defects or imperfections, they were assigned numbers. As shown in Fig. 13, the pressure in the cell remains almost constant initially and then increases linearly for both pressure transmitting media (PTM), ethanol/methanol mixture, and argon gas. However, in the case of argon gas PTM, the values are more scattered than when using the methanol/ethanol mixture, which can be explained by the lower stability of the DAC system when argon is used. The red oval in Fig. 13b shows the outliers that belong to a single measurement, and they may have been caused by non–hydrostatic pressure in the cell, such as direct pressurizing of the Ruby by diamonds.

Fig. 14 compares the measurements performed with the methanol/ethanol mixture and argon as PTMs. Fig. 14a shows the data for DACs with diamonds of 0.45 mm culets, and Fig. 14b shows the data for DACs with diamonds of 0.75 mm culets. As seen in both figures, the average pressure in the cell for a particular pressure in the driver does not depend on the PTM. However, almost twice the pressure was reached for all measurements with liquid PTMs compared to those with Ar. In most cases of the measurements with Ar, it was impossible to further increase the pressure due to the deformation of the hole in the gasket. Additionally, spherical deformation of the diamond culet was observed at high pressures when liquid PTMs were used (see Fig. 15), which was never observed in the measurements with Ar as the PTM. These observations suggest that Ar is much more compressible than liquid PTMs.

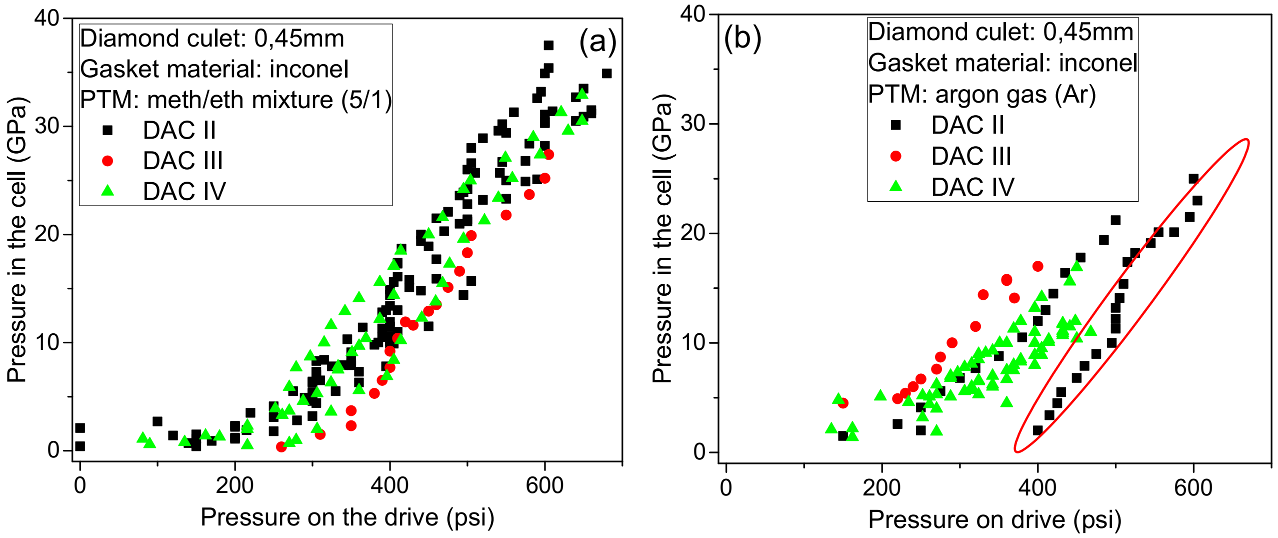

Fig. 13. Dependences of pressure in the cell on the pressure on the drive for different cells. In (a) – measurements were done with a methanol/ethanol mixture (with the 5/1 volume ratio) as PTM, and in (b) – measurements were done with argon gas.

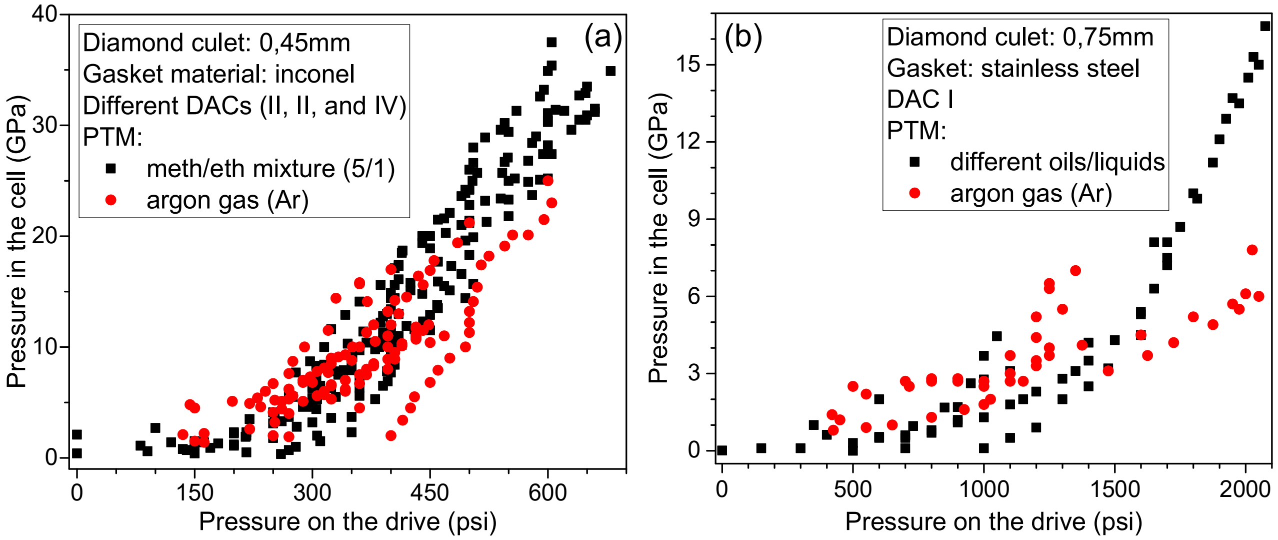

Fig. 14. Dependences of pressure in the cell on the pressure on the drive for different cells. In (a) – measurements were done on diamonds with 0.45 mm, and in (b) – measurements were done on diamonds with 0.75 mm culets.

In Fig. 15, the size of the surface reflecting light suggests that the flat culet of the diamond undergoes deformation into a spherical–like shape under pressure. At 4 GPa, almost half of the culet reflects light because it is almost completely flat. As pressure increases, the curvature of the diamond's culet increases, resulting in a smaller portion of the rounded surface reflecting light into the camera. At higher pressures, if the light source illuminating the culet is moved, a different portion of the culet will reflect the light. This is demonstrated in the video provided in [107].

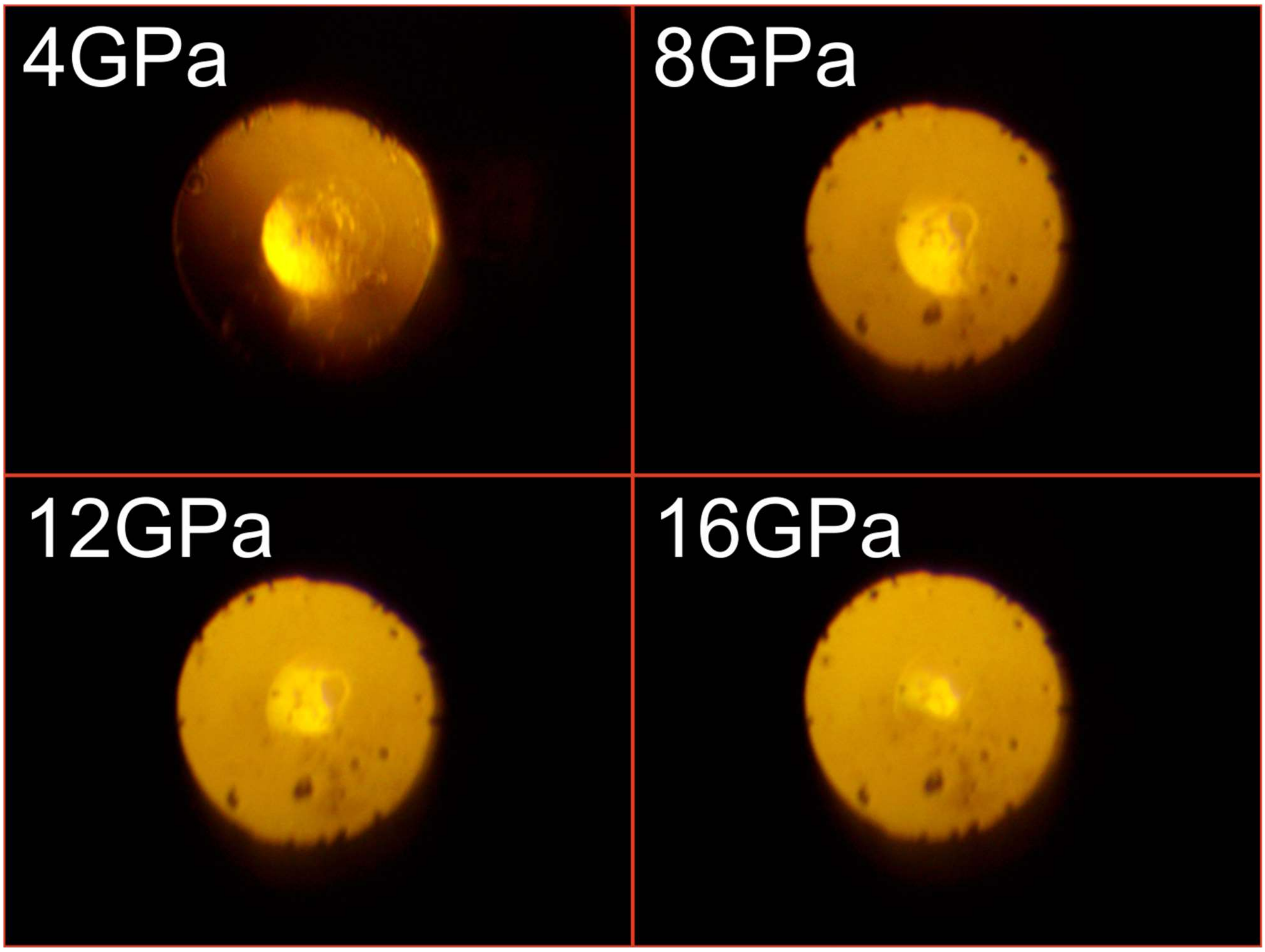

Fig. 15. Photos of the DAC at different pressures, demonstrating the diamond deformation under pressure. The reflection of the light from the gasket, pressed by the culet of the diamond, has the shape of the reflection from the curved (close to spherical) surface.

The ability to reach high pressure is often crucial in high–pressure (HP) measurements, as it offers a wider range of experimental possibilities. Sometimes, a recycling method is used to reach a higher pressure. The method involves releasing the pressure and then reapplying it, which is believed to enable higher pressure in the cell to be achieved at the same pressure values on the driver.

Fig. 16 shows a few measurements where recycling was used. Fig. 16a shows examples of recycling where Ar was used as a PTM, but some additional factors were present in all these cases. First of all, all these measurements were performed at liquid helium temperatures. In two cases shown in Fig. 16a, the pressure was released, and the DAC was heated from ~8 K up to 60–80 K and then cooled down, and the pressure increased again. These cases are labeled as “heated.” Another case is labeled as “click & jump”. In these cases, the characteristic noises could be heard during pressure increase at low temperatures, which can be described as a metal clicking sound. Usually, this click is accompanied by a jump in the pressure in the cell without any pressure change on the driver. The louder the clicking noise, the higher the pressure jumps. Sometimes the pressure jumps too high, in which case the pressure can be reduced if a measurement at a lower pressure is desired.

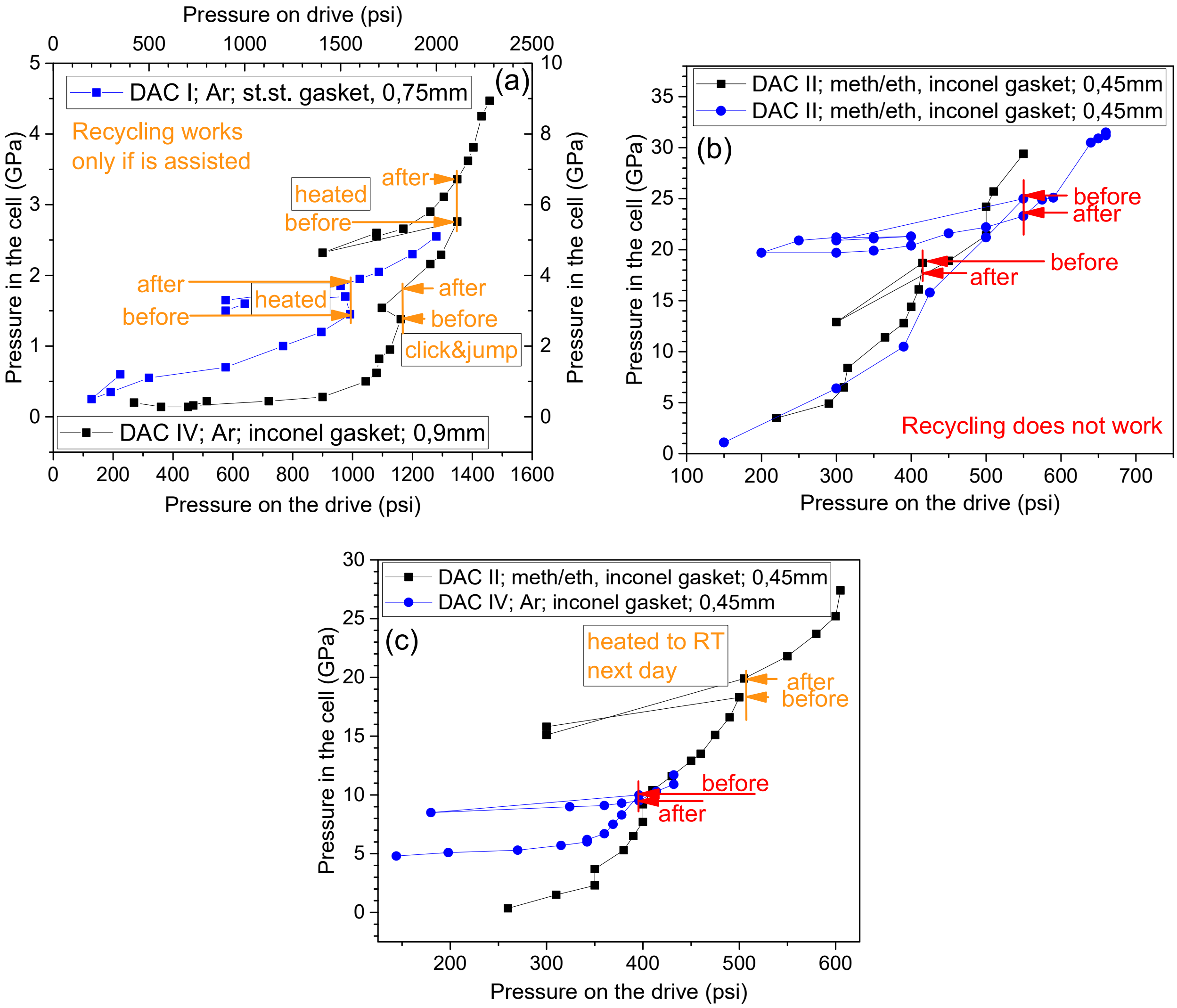

Fig. 16. Few measurements, in which recycling was used.

A few examples of recycling attempts with a methanol–ethanol mixture that were not successful are shown in Fig. 16b. Two more examples of recycling attempts, with different PTMs, are shown in Fig. 16c. In these cases, recycling did not result in higher pressure, or was accompanied by another factor. The measurement was stopped for the night and the cell was heated to room temperature. The pressure was then released before heating the cell and reapplied afterward.

VII. Results and discussion

VII.1. Study of Eu^{3+} in *R*AlO_3 (*R* = Gd, Tb, Lu, $Gd_{0.6}Lu_{0.4}$, or Y)

VII.1.1. Luminescence at ambient conditions

Before conducting HP measurements, ambient pressure luminescence spectra of the examined materials were measured. The results are presented in Fig. 17. All samples except GdAP exhibited clear and highly intense luminescence of Eu^{3+}. In terms of relative intensities and quantity of lines, TbAP and GdAP exhibited very similar luminescence. This observation suggests that Eu^{3+} predominantly occupies the same sites in these SCFs. Based on the prevailing $^5D_0 \rightarrow {}^7F_2$ transitions for these samples, it is hypothesized that Eu^{3+} is located in a site with no inversion symmetry or that this site is dominant. The difference in Eu^{3+} luminescence in YAP indicates a different site positioning of the Eu^{3+} ion in YAP than in TbAP and GdAP. In the case of YAP, $^5D_0 \rightarrow {}^7F_1$ transitions dominate, which suggests a mainly centrosymmetric positioning of the Eu^{3+} ion. These results are in good agreement with [9].

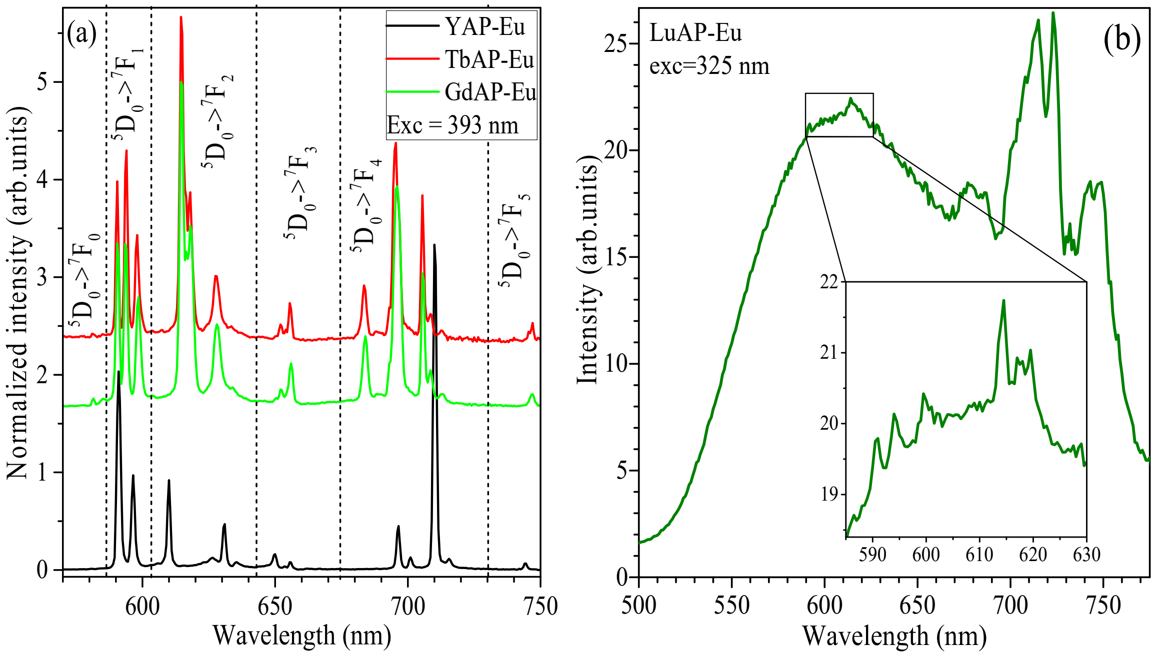

Fig. 17. Luminescent spectra of Eu^{3+} ion in YAP, TbAP, GdAP (a), and LuAP SCFs at ambient pressure (b)

The luminescence of LuAP is presented in Fig. 17b, which shows that the broadband luminescence is almost overwhelming the Eu^{3+} luminescence. This result differs from what was reported in [9], where the broadband luminescence was assigned to certain defects and additional uncontrolled dopants in the YAP substrate. However, considering the thickness of the LuAP SCF (4–12 μm) and the thickness to which the sample was polished (approximately 25–28 μm), YAP luminescence should not be as prominent as it is. Therefore, the broadband luminescence is assigned to defects in the LuAP SCF itself. The samples were grown in PbO–B_2O_3 flux, so part of the broadband luminescence may originate from Pb^{2+} impurities (see, e.g., [108]). Another part of the luminescence is related to the other defects in residuals of the YAP substrate. Nevertheless, this interpretation and broadband luminescence are in good agreement with [12], where the emission of one– and two–electron–charged isolated and aggregated oxygen vacancies are studied in detail. The presence of these defects in SCF is less expected due to the relatively low temperature of SCF crystallization (about 930–950°C).

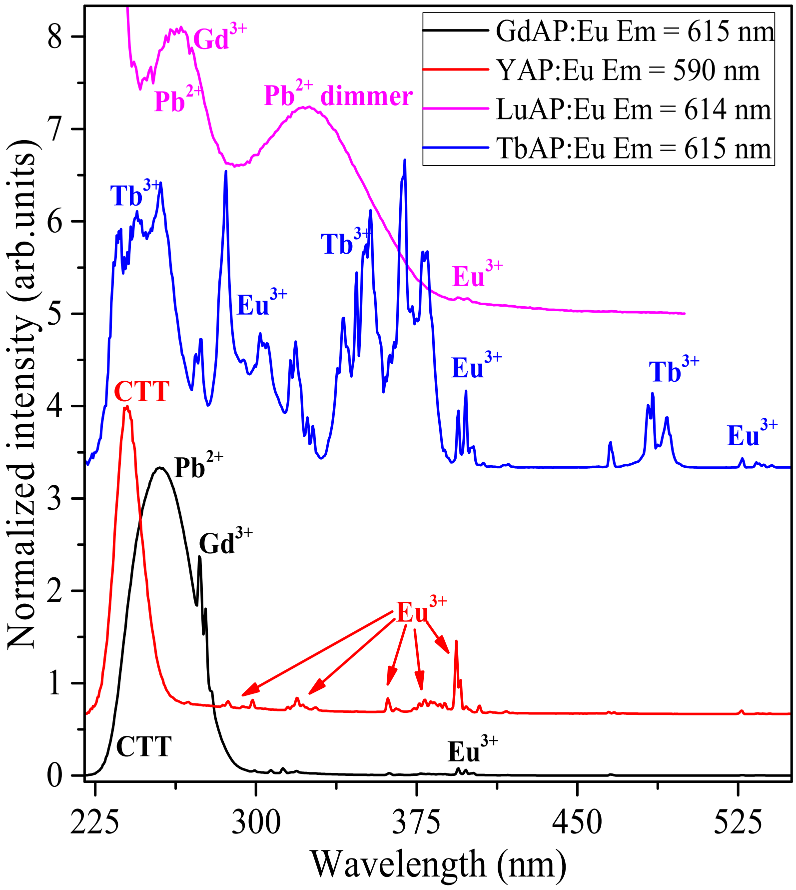

Fig. 18. Excitation spectra of Eu^{3+} luminescence (PLE) in SCFs of RAP:Eu (R = Gd, Tb, Y, Lu) perovskites

The normalized spectra of photoluminescence excitation (PLE), measured at ambient pressure, are presented in Fig. 18, which show sharp lines typical of trivalent europium in all spectra. However, in the case of LuAP, these sharp lines are the weakest. PLE spectra of YAP and GdAP exhibit broad bands at approximately 240 and 256 nm, respectively, which were assigned to charge transfer transitions from O_2 to Eu^{3+} [14]. The broad band in GdAP is much broader than in YAP, possibly due to overlapping with the excitation band assigned to Pb^{2+} ions present in GdAP, resulting from its crystallization from PbO–B_2O_3 flux. The PLE spectrum of LuAP contains broad bands at 265 nm and 325 nm, which were assigned to Pb^{2+} single and Pb^{2+} dimers, respectively, following [9]. Notably, TbAP exhibits Tb^{3+} excitation lines along with Eu^{3+} excitation sharp lines (see Fig. 18). All excitation sharp lines and broad bands in the spectra were assigned according to [9].

VII.1.2. High–pressure measurements

VII.1.2.1. Eu^{3+} sharp lines

High–pressure measurements were conducted on GdAP, TbAP, $Gd_{0.6}Lu_{0.4}AP$, and LuAP SCFs at room temperature, and the results are presented in Fig. 19.

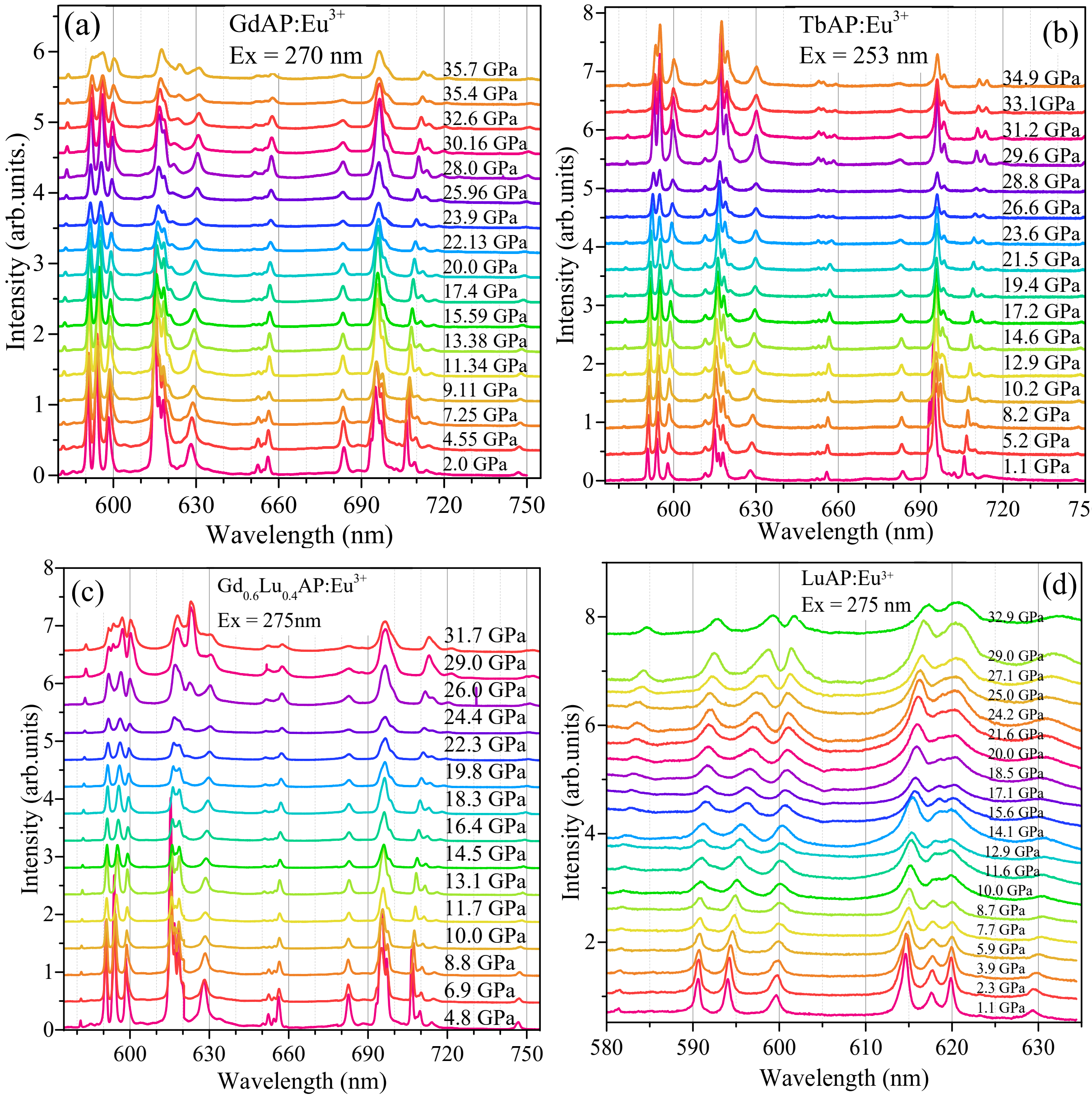

Fig. 19. Room temperature high–pressure Eu^{3+} luminescence spectra of GdAP:Eu (a), TbAP:Eu (b), $Gd_{0.6}Lu_{0.4}AP$:Eu (c), and LuAP:Eu (d) SCFs under excitation at 270 nm, 253 nm, 275 nm, and 275 nm, respectively.

The luminescent spectra of Eu^{3+} in all perovskites are very similar, which is expected considering the shielding from the external crystal electric field of the Eu^{3+} *4f* electrons by the *5s* and *5p* shells. For all samples in Fig. 19, luminescence originating from the $^5D_0$ to $^7F_2$ transition is dominant. As pressure increases, there are no evident changes in Eu^{3+} luminescence in LuAP SCF. This luminescence still has a relatively broad band, which was subtracted as the background for the results presented in Fig. 19d. On the contrary, an additional sharp line appears at high pressures in $^5D_0$ to $^7F_1$ luminescence transition of GdAP and $Gd_{0.6}Lu_{0.4}AP$ SCFs. In the case of Eu^{3+} luminescence in TbAP, no additional lines appear, but neighboring lines start merging at high pressures.

A few luminescence lines of Eu^{3+} were chosen, and their positions were defined. Pressure dependences of these positions are plotted in Fig. 20. Positions of all lines are changing linearly towards lower energies with the increase in pressure.

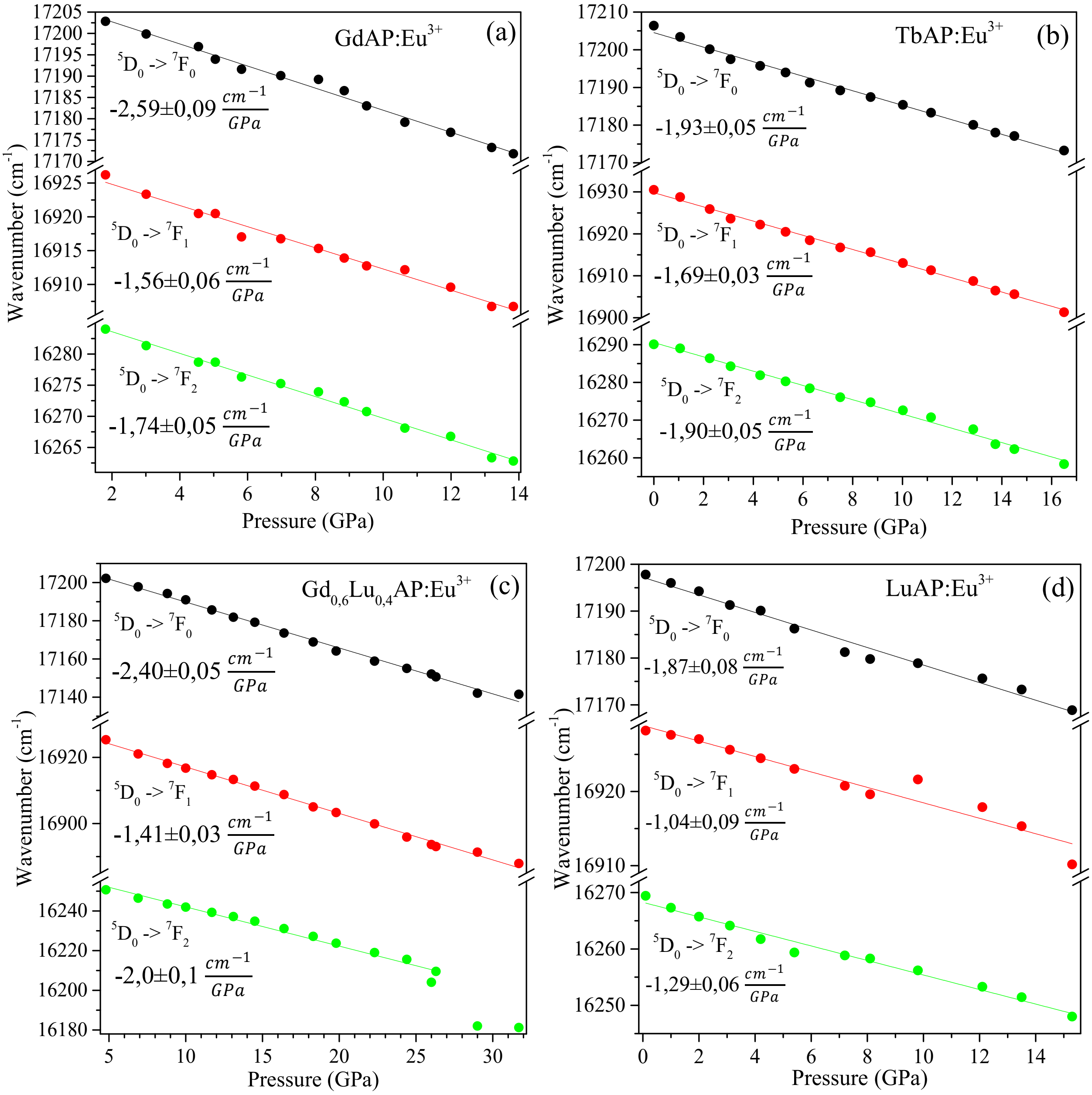

Fig. 20. Dependences of Eu^{3+} lines energy positions on pressure. Lines of Eu^{3+} luminescence, which correspond to $^5D_0 \rightarrow$ 7F0, $^5D_0 \rightarrow {}^7F_1$, and $^5D_0 \rightarrow {}^7F_2$ for GdAP (a), TbAP (b), $Gd_{0.6}Lu_{0.4}AP$ (c), and LuAP (d).

To calculate K–values next steps have been undertaken. First, the background has been subtracted from each spectrum of every sample. As a second step, the area under the luminescence curves for each line set of particular transitions (for $^5D_0 \rightarrow {}^7F_1$ and $^5D_0 \rightarrow {}^7F_2$ transitions separately) have been integrated. And finally, the K–value has been calculated, as the relation of integrated intensities. According to [14], the bigger is distortion from the centrosymmetric site, the higher the K–value should become. K–values, obtained in this work, and for comparison K–values from [9], are given in. As can be seen from the table, K–values are in good agreement with [9]. Slight differences between values, obtained in this work and in [9], are most probably due to the usage of the different excitation wavelengths.

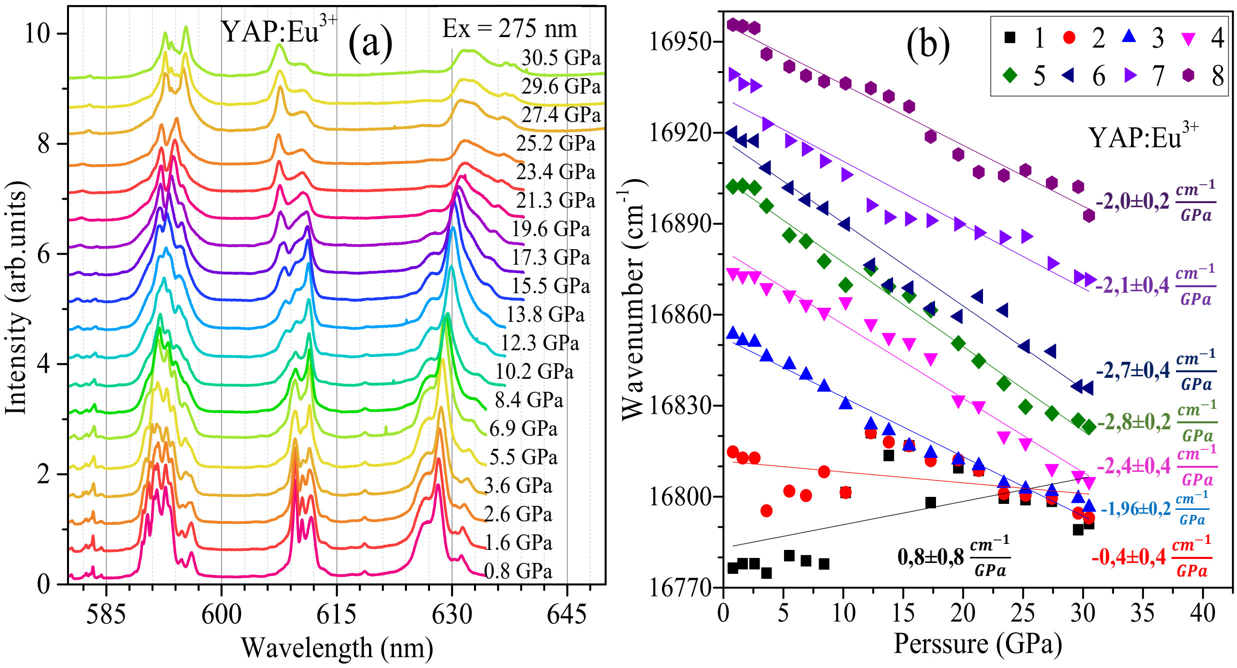

Fig. 21. High–pressure luminescence spectra of Eu^{3+} in YAP (a) and positions of lines, which originate from $^5D_0$ to $^7F_1$ transition (b). Numbers from 1 to 8 denote lines, which at ambient pressure have the following wavelengths: 1 – around 596 nm, 2 – around 594.7 nm, 3 – 593.3 nm, 4 – 592.6 nm, 5 – 591.6 nm, 6 – 591 nm, 7 – 590.3 nm, 8 – 589.8 nm.

Ion (R)	Ionic radius (by Shannon) (Å)	K–value from [9]	K–value, this work
Eu^{3+}	1.066	–	–
Gd^{3+}	1.053	1.7–1.88	1,77–1,84
Tb^{3+}	1.04	1.79–1.83	1,79–1,82
$Gd_{0.6}Lu_{0.4}{}^{3+}$	1.0226	1.74–1.84	1,81–1,87
Y^{3+}	1.019	0.347–0.405	0,69–0,71
Lu^{3+}	0.977	1.51–2.0	1,74–1,81

Table 2. Ionic radii of ions, on which perovskite SCF are based, and ambient pressure K–values of the Eu^{3+} luminescence from this work, and from [9]. For $Gd_{0.6}Lu_{0.4}$ “Ionic radius” means a weighted value of Gd and Lu ionic radii with corresponding concentration coefficients.

To calculate K–values, the background was first subtracted from each spectrum of every sample. As a second step, the area under the luminescence curves for each line set of particular transitions (for $^5D_0 \rightarrow {}^7F_1$ and $^5D_0 \rightarrow {}^7F_2$ transitions separately) was integrated. Finally, the K–value was calculated as the relation of integrated intensities. According to [14], the higher the distortion from the centrosymmetric site, the higher the K–value should become. K–values obtained in this work and from [9] for comparison are given in Table 2. As shown in the table, K–values are in good agreement with [9]. Slight differences between the values obtained in this work and in [9] are most likely due to the use of different excitation wavelengths.

Fig. 21a shows that there are numerous lines in YAP:Eu^{3+} luminescence. Therefore, it was measured at 10 K to resolve those lines better. All other samples were measured at room temperature (Fig. 21). In all samples, Eu^{3+} luminescent lines originating from $^5D_0$ to $^7F_1$ transition are shifting towards lower energy as pressure increases (Fig. 20). In the case of YAP, the situation is different (see Fig. 21). Some lines are shifting towards higher energies, and some are shifting towards lower energies. Moreover, the lines shifting towards lower energies are shifting at different rates than the other lines. This is not typical for Eu^{3+}. For many different materials, Eu^{3+} lines should shift towards lower energies with the increase in pressure (e.g., lithium borate glasses [109], silicates and vanadates [110], oxides [111]).

VII.1.2.2. Broadband luminescence

The broadband luminescence peak, with a maximum of around 600 nm, is observed under 325 nm excitation in the LuAP sample (see Fig. 17b), and its origin is attributed to the Pb^{2+} flux dopant centers [112]. Fig. 22 shows the luminescence spectra of undoped LuAP SCF, grown from PbO–based flux, and a similar broadband luminescence is evident. The origin of this broad band luminescence is studied in detail in [108, 112], where it is described as the luminescence of an exciton localized at single and paired Pb^{2+} centers.

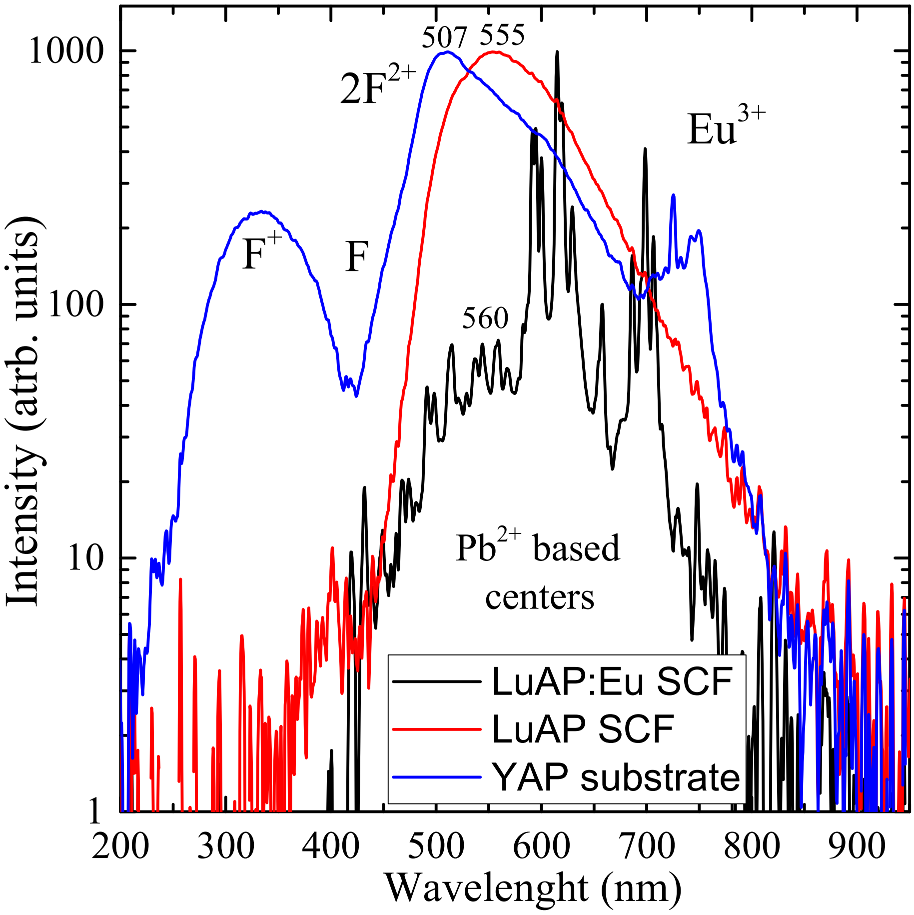

Fig. 22. CL spectra (in log scale) of LuAP:Eu SCF in comparison with the spectra of nominally undoped LuAP SCF, grown from PbO–based flux, and YAP substrate. The spectra were normalized to the same intensity at the maximum.

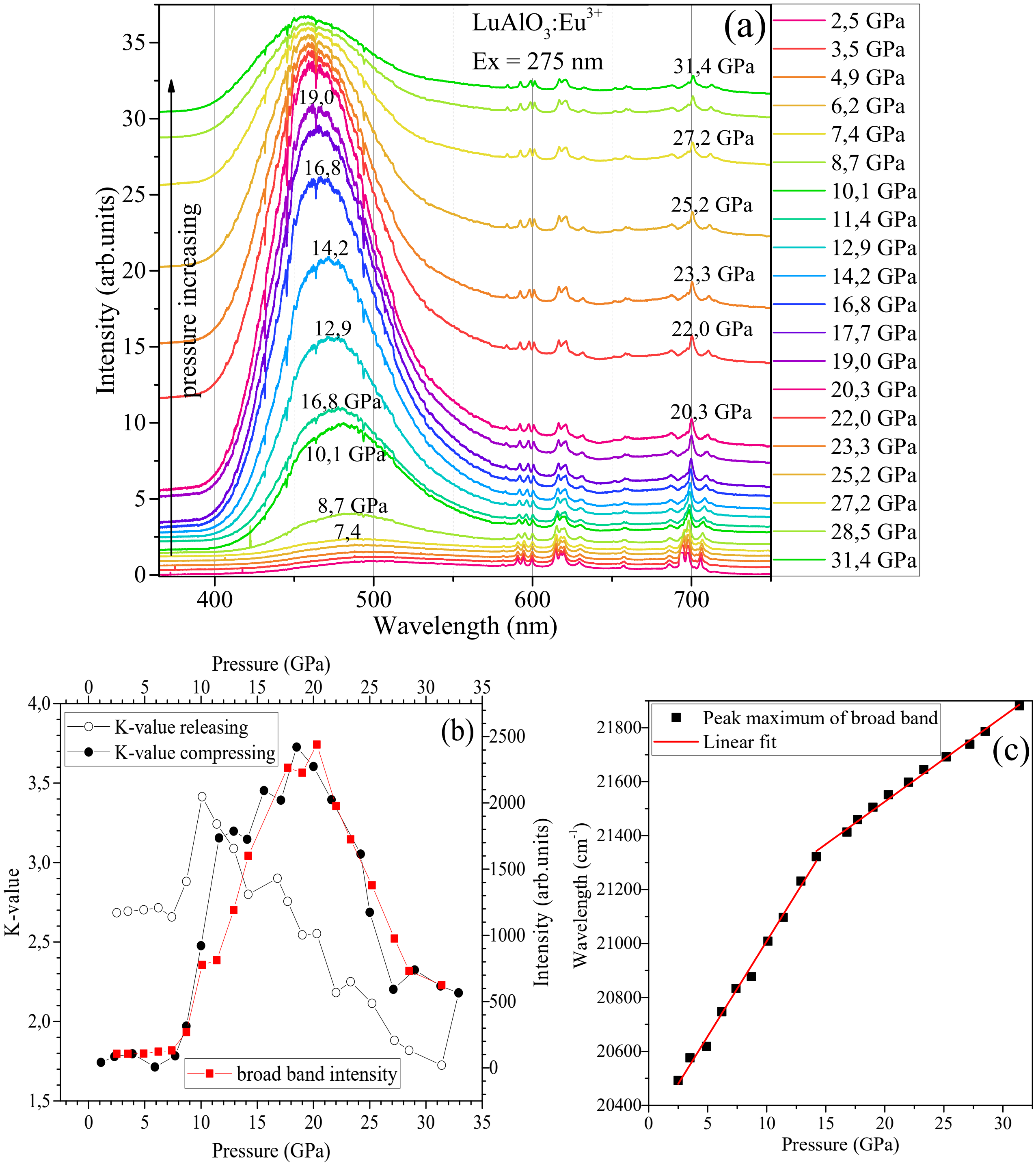

Fig. 23. Broad luminescence band of LuAP:Eu SCF under high–pressure (a). Comparison of pressure dependence of K–value with pressure dependence of the intensity of broadband of visible luminescence (b). The dependence of peak maximum of broad luminescence band on pressure (c).

When excited at 275 nm, LuAP:Eu^{3+} exhibits another broad band around 490 nm with high intensity (see Fig. 23). This broad band probably has two strongly overlapped components. As pressure increases, the intensity of this luminescence increases, reaches its maximum at around 23 GPa, and then decreases (see Fig. 23b). The position of this peak shifts towards higher energies with pressure, but the shifting rate changes before and after 15 GPa (see Fig. 23c). The shifting rate before 15 GPa is 71 ± 2 cm^{-1}/GPa, and after 15 GPa, it reduces to 31.6 ± 0.8 cm^{-1}/GPa.The most probable explanation for the change in the shifting rate is the different pressure behavior of the two components of this band. A similar broadband luminescence at ambient pressure peaked at 497 nm was previously reported for YAP crystals [12]. In the cathode–luminescence (CL) spectra of the YAP substrate, similar broadband luminescence (peaked at 507 nm with a bump around 600 nm) is also present (see Fig. 22). The nature of the defects related to this YAP luminescence in the visible range is still unknown. There are two probable candidates for the role of these defects: (i) doubly charged oxygen vacancies (F–centers); (ii) dimers of oxygen vacancies with trapped electrons ($2F^{2+}$ centers).

The dependence of the intensity of the broadband luminescence on pressure strongly correlates with the K–value dependence on pressure (see Fig. 23b), suggesting that the defects are located in the closest vicinity to the Eu^{3+} centers. The influence of contamination by Pb^{2+} ions (due to the use of PbO–based flux) is studied in detail in [12, 113].

VII.1.2.3. K–value on pressure

The dependencies of K–values on pressure for all samples are shown in Fig. 24. K–values of GdAP, TbAP, $Gd_{0.6}Lu_{0.4}AP$, and YAP decrease linearly with pressure (Fig. 24a). The K–values of all samples have similar numerical values, but YAP has a smaller K–value, which agrees with [9]. At the lowest pressures, the K–values of the samples are around 1.8, while the smaller YAP K–value is about 0.7. All K–values' dependencies were normalized to 1.8 at the lowest pressure, and the obtained data are plotted in Fig. 24b. Normalized K–values decrease linearly at approximately the same rate for all samples, as described in [16], where the authors study the dependence of the rotational and tilting angles (see Fig. 2) on pressure. As pressure increases, both angles approach 180°, and Eu^{3+} sites change to sites with inversion symmetry, confirmed by the K–value decreasing.

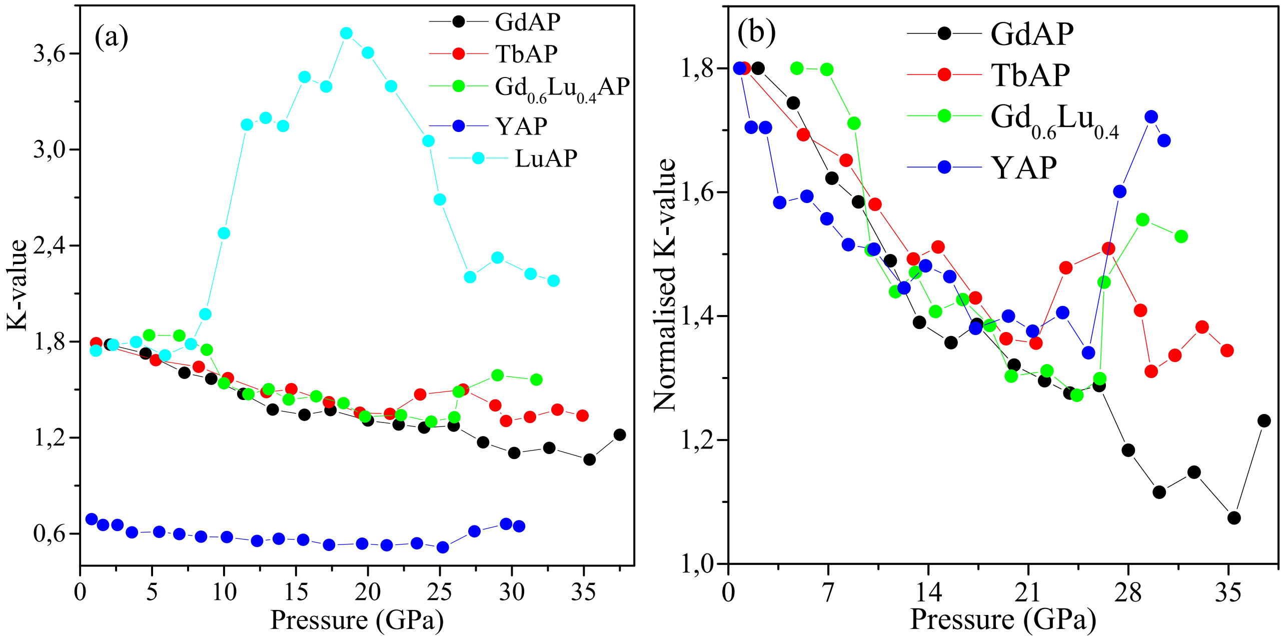

Fig. 24. K–value dependence on pressure for all samples – a. Normalized K–value for all samples – b.

However, the K–values start jumping almost randomly at higher pressures, which may be attributed to a loss of hydrostatic conditions. While this can be explained by various factors, such as thinning of the gasket or a loss of hydrostatic properties in the transmitting media (PTM) [114].

The LuAP sample has a different pressure dependence for the K–value (see Fig. 24a), likely due to the interaction between Eu^{3+} centers and defects in LuAP SCF. A broadband luminescence that most likely originates from these defects was observed under 325 nm excitation (see Fig. 17b), in PLE spectra (see Fig. 12), and in CL spectra (see Fig. 22) at ambient conditions. Under 275 nm excitation at high pressure, another high–intensity broadband peak was discovered with a maximum of around 500 nm. As shown in Fig. 23, the position of this broadband luminescence shifts towards higher energies as pressure increases. Fig. 23b shows that the K–value of LuAP is strongly correlated with the integrated intensity of broadband luminescence, providing additional evidence of the interaction between Eu^{3+} luminescence centers and LuAP defects.

VII.2. Study of Ce^{3+} in LuAP and GdAP

VII.2.1. Structure check by SEM and X–Ray

The single crystallinity and high quality of LuAP:Ce SCF are confirmed by SEM and X–ray diffraction. The crystalline phase of the prepared LuAP:Ce/YAP epitaxial structures is characterized in the 2θ range from 20° to 100° with a step of 0.02° using a modified DRON 4 spectrometer (Cu $K\alpha_1$ X–ray source). The SEM image in Fig. 25a reveals very few pits, hills, square holes, scratches, or brighter spots on the SCF surface. In Fig. 25b, the XRD scan shows the (004) reflexes of the LuAP film and YAP substrate, which allows for the determination of the misfit between the lattice constants of the YAP substrate and the LuAP SCF. The misfit, m = [(ascf – asub)/ascf] × 100%, is equal to 1.255%.

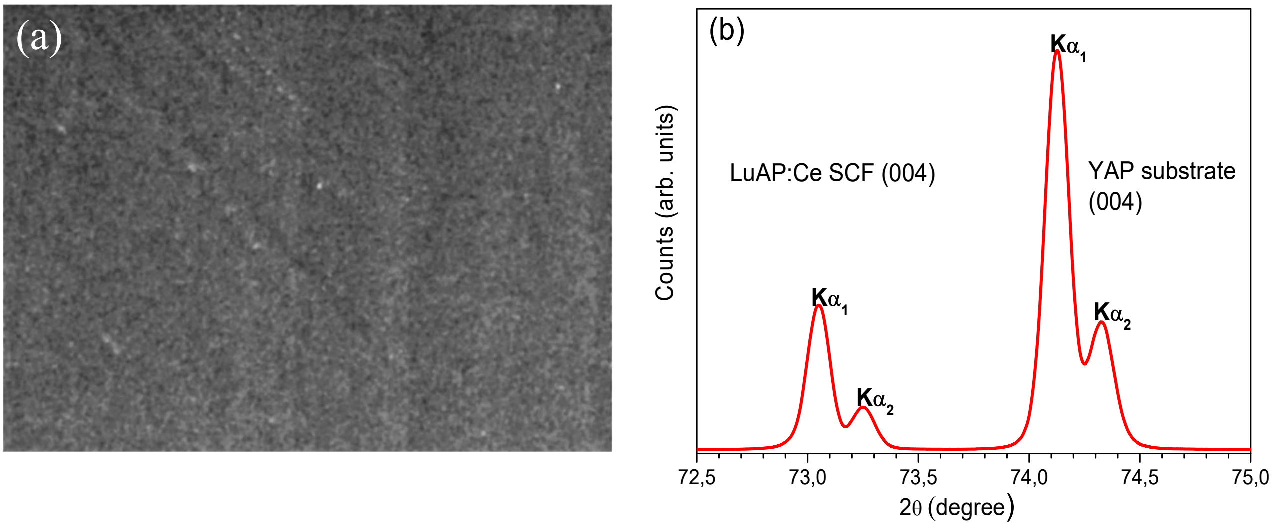

Fig. 25. (a) SEM image of the LuAP:Ce SCF surface under 700 magnification. (b) XRD pattern of the (004) reflexes of the LuAP:Ce film and the YAP substrate

Due to the large difference between the lattice constants of LuAP:Ce SCF and the YAP substrate, huge mechanical stress is exerted on the film–substrate interface, which can affect the optical properties of the LuAP:Ce film [115, 116].

The relaxation of the stress between the film and substrate may cause the SCF structure to crack. The propagation of such stress within the volume of SCF can cause gradual changes in the cation–anion distances, resulting in notable changes in the optical spectra of both the LuAP host and dopants. Similar observations have been made in LuAG:Ce SCFs, grown by the LPE method on top of YAG substrates, where the misfit between the respective garnet lattices was about 0.7% [117].

VII.2.2. Absorption spectra

The room temperature absorption spectra of Ce–doped YAP and LuAP single crystals are presented in Fig. 26a and Fig. 26b, respectively. The square of the absorption coefficients of undoped YAP and thin Ce–doped LuAP single crystals in the 5–8 eV spectral range are shown in the insets, along with linear fits to the data near the fundamental absorption edges. The fits provide precise values of the energy gaps of YAP (7.63 eV) and LuAP (7.86 eV) at room temperature, assuming direct band gaps. The fits assuming indirect band gaps yield slightly smaller band gaps (by about 0.2–0.3 eV). It is worth noting that the determined bandgap energy of the LuAP bulk crystal (7.86 eV) is lower than the previously reported value of 8.44 eV [118] for single crystalline films, as well as the estimated energy of 8.2 eV for bulk LuAP [12].

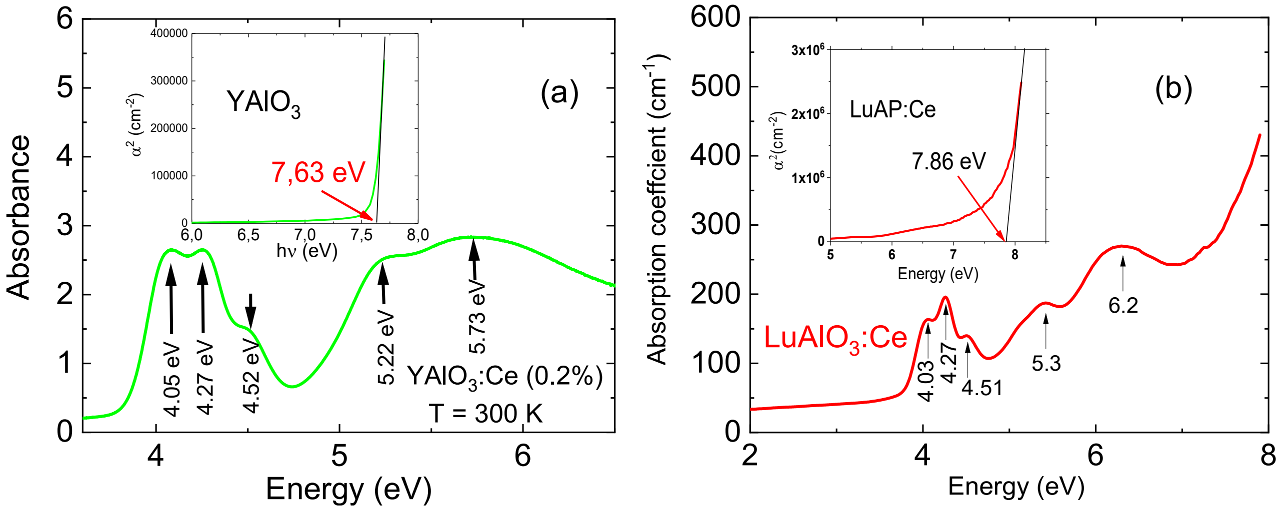

Fig. 26. Room temperature absorption spectra of YAP:Ce (a) and LuAP:Ce (b) single crystals. The positions of Ce^{3+} 5d levels in LuAP:Ce and YAP:Ce crystals are marked with arrows. In the insets, linear fits the square of the absorption coefficients near the fundamental absorption edges of YAP (a) and LuAP (b) are shown.

VII.2.3. Temperature dependence of the luminescence

VII.2.3.1. Luminescence spectra

The luminescence spectra of Ce^{3+} in bulk YAP and LuAP single crystals were measured as a function of temperature under 300 nm excitation. As shown in Fig. 27, the Ce^{3+} luminescence spectra in both samples are very similar. At low temperatures, the spectra consist of two broad bands corresponding to transitions from the lowest *d*–level to the spin–orbit split $^2F_{5/2}$ ground and $^2F_{7/2}$ excited states of the *4f* configuration (Fig. 27a). The relatively small crystal field splitting of the two *4f* levels is not observed in the *5d→4f* luminescence due to strong electron–phonon coupling of the *5d* levels and low transition probability to the high–energy component of the $^2F_{7/2}$ excited state [119].

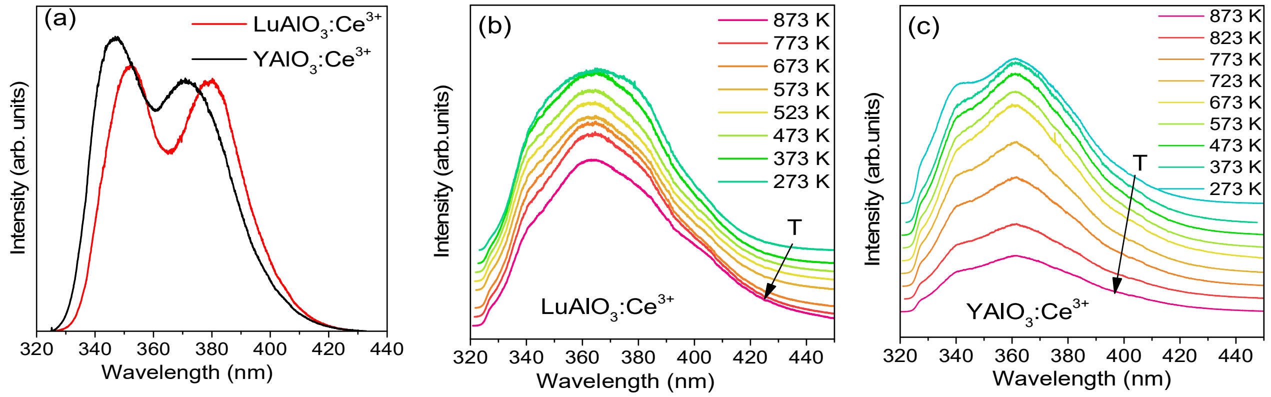

Fig. 27. (a) Luminescence spectra of Ce^{3+} in LuAP (red line) and YAP (black line) single crystals at 6 K. Temperature–dependent luminescence spectra of Ce^{3+} in LuAP (b) and YAP (c) single crystals. All spectra were detected under 300 nm excitation. The spectra in (b) and (c) are shifted in intensity scale.

As the temperature increases, the second– and third–lowest *d*–levels, which lie at 237 and 216 nm in YAP:Ce and 234 and 200 nm in LuAP:Ce (see Fig. 26), become thermally populated. Radiative transitions from this level lead to a slight blue shift of the emission spectra and an apparent smearing out of the double peak structure. Similar results were observed in [120]. The spectra collected at selected temperatures above 273 K in LuAP and YAP single crystals are shown in Fig. 27b and Fig. 27c, respectively.

VII.2.3.2. Dependence of the luminescence intensity

As shown in Fig. 27b, the luminescence intensity in the LuAP:Ce crystal remains constant with temperature up to 873 K, while in YAP, quenching of Ce luminescence occurs above 650 K (Fig. 27c). The integrated Ce luminescence intensities normalized to room temperature are presented in Fig. 28 for YAP (full symbols) and LuAP (open symbols).

To fit the dependence of the luminescence intensity on temperature, the following assumptions have been made. Firstly, the intensity of the luminescence originating from the transition from a single level to all possible ground states is assumed to be proportional to the population of that excited state. Therefore, the quenching increases as the probability of the thermal population of the conductive band increases, which causes a decrease in the population of the luminescent state.

$$I_i \sim \frac{g_i e^{-\frac{E_i}{kT}}}{\sum_i g_i e^{-\frac{E_i}{kT}}} = \frac{g_i e^{-\frac{E_i}{kT}}}{g_i e^{-\frac{E_i}{kT}} + g_{E_g} e^{-\frac{E_g}{kT}}} = \frac{1}{1 + \frac{g_{E_g}}{g_i} e^{-\frac{\Delta E}{kT}}} \qquad (9)$$

Here g_i is the degeneracy of the *i*–level, E_i is the energy of the *i*–level with respect to an arbitrary zero, E_g is the position of the bottom of the conduction band with respect to the same arbitrary zero, and *ΔE* is the energy distance between the *i*–level and the conduction band. If the arbitrary zero is chosen as the top of the valence band, then E_g becomes the band gap.

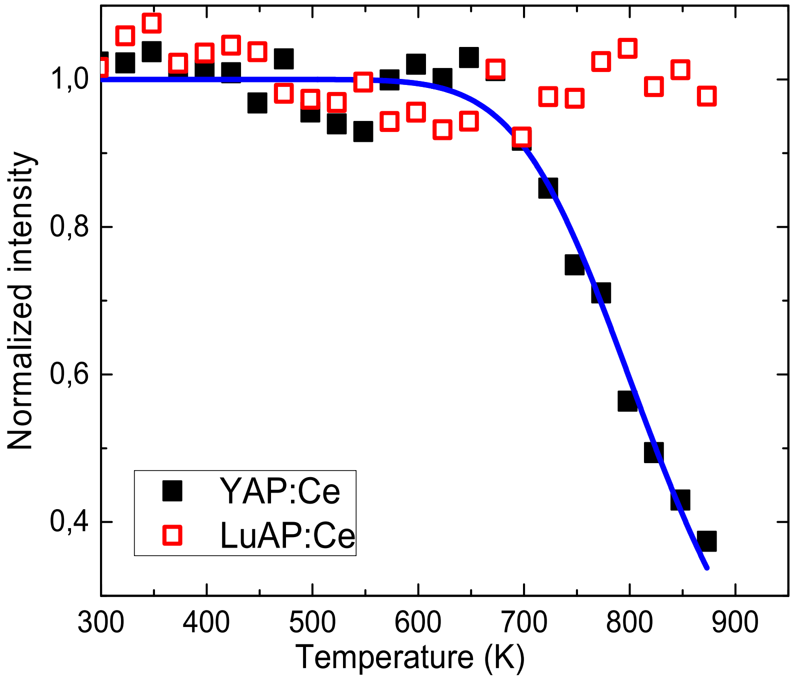

Fig. 28. Temperature dependence of the normalized, integrated intensity of Ce^{3+} luminescence in LuAP (open symbols) and YAP (full symbols). The solid line is a fit with Eq. (12).

If we consider only the lowest level, the dependence of the intensity on temperature can be described by the equation:

$$I(T) = \frac{I_0}{1 + \frac{g_{E_g}}{g_1} e^{-\frac{\Delta E}{kT}}} = \frac{I_0}{1 + a_1 e^{-\frac{\Delta E}{kT}}} \tag{10}$$

Alternatively, we can take into account the influence of the two lower excited levels of Ce^{3+}. The luminescence from both levels will affect the total intensity of the luminescence, so the sum of both individual transitions should be considered:

$$\begin{aligned} I(T) = I_1 + I_2 = I_0 \left(\frac{g_1 e^{-\frac{E_1}{kT}}}{\sum_i g_i e^{-\frac{E_i}{kT}}} + \frac{g_1 e^{-\frac{E_2}{kT}}}{\sum_i g_i e^{-\frac{E_i}{kT}}} \right) = I_0 \frac{1 + \frac{g_2}{g_1} e^{-\frac{E_{21}}{kT}}}{1 + \frac{g_2}{g_1} e^{-\frac{E_{21}}{kT}} + \frac{g_{E_g}}{g_1} e^{-\frac{\Delta E}{kT}}} \\ = I_0 \frac{1 + a_1 e^{-\frac{E_{21}}{kT}}}{1 + a_1 e^{-\frac{E_{21}}{kT}} + a_2 e^{-\frac{\Delta E}{kT}}} \end{aligned} \tag{11}$$

Similarly, if we consider three levels, the following equation can be used:

$$I(T) = I_0 \frac{1 + a_1 e^{-\frac{E_{21}}{kT}} + a_2 e^{-\frac{E_{31}}{kT}}}{1 + a_1 e^{-\frac{E_{21}}{kT}} + a_2 e^{-\frac{E_{31}}{kT}} + a_3 e^{-\frac{\Delta E}{kT}}} \tag{12}$$

Here, I_0 is the initial low–temperature luminescence intensity, *ΔE* is the energy distance between the lowest *5d* level and the bottom of the conduction band (treated as a fitting parameter), E_{21} is the energy distance between the lowest *5d* and second lowest *5d* level, and E_{31} is the energy distance between the lowest *5d* and third lowest *5d* level. The parameters α_1 and α_2 are ratios of the radiative recombination probabilities from the second and third *d*–level to that of the lowest *d*–level, while α_3 is the ratio between the ionization rate and the radiative transition probability.

The energy distances $E_{21} = 0.22$ eV and $E_{31} = 0.470$ eV are determined from the absorption spectra in Fig. 26a. The lowest excited level of Ce^{3+} is located at $\Delta E = 1.27$ eV below the bottom of the conduction band, as determined from the fit of Eq. (12) to the experimental data (presented as a solid line in Fig. 28), with fitting parameters $\alpha_1 = 7$, $\alpha_2 = 4400$, $\alpha_3 = 4 \times 108$, and $\Delta E = 1.27$ eV. The uncertainty of ΔE is less than 50 meV. We considered the three lowest levels because they are all located in the band gap, and therefore, they should be included. The fourth level from the bottom excited state is also located in the band gap, near the bottom of the conduction band. Nevertheless, we did not consider it in Eq. (12) to avoid adding more approximation parameters, which could make the fitting procedure less reliable. Besides, this level is close to the conduction band and is broad in absorption spectra.

The obtained data from fitting allowed for the estimation of the position of the ground *4f* state of Ce^{3+} in YAP crystal, which is a critical parameter in the Dorenbos model [121]. Recent theoretical DFT calculations supported the value of 3.5 eV as the position of the first *4f* level of Ce^{3+} above the top of the valence state [19]. Our results indicate that the ground *4f* level is located at 2.31 eV above the top of the valence band of YAP, based on the distance between the lowest *5d* level and the bottom of the conduction band (equal to 1.27 eV), the band gap energy (equal to 7.63 eV), and the energy of the absorption peak to the first *5d* level (4.05 eV). This gives rise to a difference of approximately 1.19 eV between the experimentally estimated position and the one obtained from Dorenbos theory and theoretical DFT calculations [19]. The remaining difference of 0.9 eV may be due to the temperature decrease of the band–gap energy, which is expected to occur between room temperature and 873 K. Although the temperature dependence of the band–gap energy of YAP has not been experimentally established, the expected changes in the band–gap energy are in the range of at least a few hundred meV [122]. Therefore, the theoretical predictions of the Dorenbos model and DFT calculations are consistent with our experimental findings, within the expected accuracy limits (about 0.3–0.5 eV) [123]. However, the theoretical energy value of 3.5 eV may be overestimated since Ce^{3+} luminescence quenching would then occur at cryogenic temperatures.

It is worth noting that the temperature quenching of Ce^{3+} luminescence is not observed in LuAP up to 873 K. This may be partly related to the larger bandgap of LuAP compared to YAP, although the relatively small difference between them (only 0.23 eV) indicates that the position of the ground state of Ce^{3+} in LuAP must be closer to the top of the valence band than in YAP.

VII.2.4. Raman spectra of the single crystalline film

Fig. 29a shows the Raman spectra of a LuAP:Ce single–crystalline film (SCF) with a thickness of approximately 21.5 µm, grown on a YAP substrate. The measurements were performed on a cross–section of the LuAP/YAP layer/substrate, and the distance of the position of the laser spot from the top of the LuAP SCF layer, denoted by *d*, is provided in Fig. 29a. Fig. 29b shows the SEM image of the cross–section, where the LuAP SCF layer, the LuAP/YAP interface, and the YAP substrate are indicated by the numbers 1, 2, and 3, respectively.

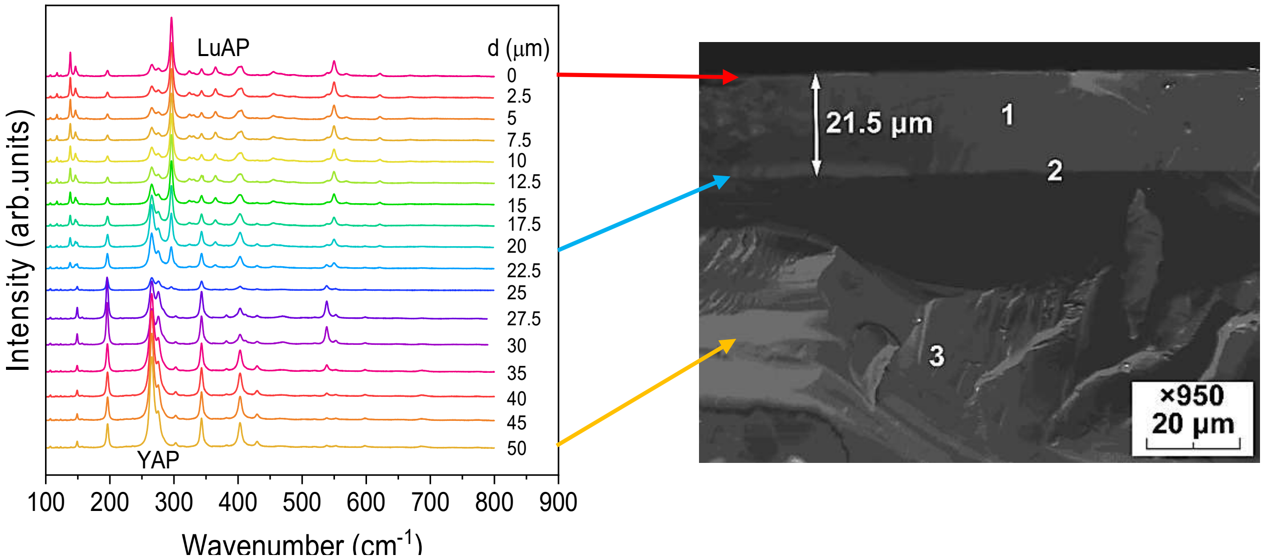

Fig. 29. (a) Raman spectra of the LuAP:Ce single crystalline layer with a thickness of about 22 µm grown on YAP substrates scanned along the YAP/LuAP cross–section. The distance of the laser focus from the top of the SCF layer for each spectrum is given in the legend. (b)–SEM picture of the YAP/LuAP cross–section.

The Raman spectra of the YAP substrate exhibit a similar pattern to the data reported in [115]. A total of 20 Raman peaks are observed for the YAP substrate, out of the 25 predicted by group theory. Within the LuAP layer, 28 modes are observed, although only 11 of them are unique to LuAP. Changes in the Raman spectra are observed when the laser spot moves across the border between the YAP substrate and the LuAP layer grown on it, occurring at a distance of approximately 22 µm from the top of the LuAP layer. The structure of the Raman lines registered for LuAP SCF is similar to that observed for YAP. Further theoretical studies are needed to assign the observed spectrum to vibrational modes expected for LuAP.

Table 3 provides a list of the observed Raman lines, along with their assignments. The Raman lines are assigned based on previous theoretical calculations of their positions [124], from which data has been taken for comparison.

Table 3. Results of Raman experiments on the 22 mm thick LuAP:Ce single crystalline layer grown on YAP substrate. The assignment of the modes predicted directional Raman activity and theoretical energies from DFT calculations are taken from [124].

Experimental (cm^{-1})					Line number, assigned in Fig. 30	DFT (cm^{-1}) [124]	Pressure coefficient (cm^{-1}/GPa)		Tentative assignment [124]	Line dominates in YAP or LuAP
YAP (on edge)	YAP (confocal)	LuAP (on edge)	LuAP (confocal)	[124]			below 10 GPa	above 10 GPa		
		117.6	117							LuAP
		138.3	138.7		0.1		1.42			LuAP
		146.3	146.8		0.2		1.11			LuAP
149	149.8	149.2	150	149		156.5			Y → b–axis; τ (O$_h$)	YAP
156.7		156.8		156		158.3			Y → a–axis; τ (O$_h$)	YAP
				194		190.6			Y → c–axis; τ (O$_h$)	absent
196.4	196.7	196.3	196.6	196	1	193.1	1.62	1.13	Y → a–axis; τ (O$_h$)	YAP
215.8				216		218.6			Y → b–axis; τ (O$_h$)	YAP
235						230.3			Y → c–axis; τ (O$_h$)	YAP
265		265.7	266.8	264	2	258.9	1.17	1.13	τ (O$_h$)[ab–axes]	YAP
275.5	276.5	275.9	276.5	276		272.1			τ (O$_h$)[bc–axes]	YAP
284.6				284	2.1	286.8	–0.04		ρ(O$_h$)	YAP
		296.2	296.5		3		1.77	1.75		LuAP
		323.9	325.8							LuAP
		330	330							LuAP
343	343.6	343	343	344	4.3	343.5	1.31	1.15	ρ(O$_h$)	YAP

		364.9	365.2							LuAP
		372	371.5							LuAP
382.3	381					392.1			$\rho(O_h)$	YAP
403.1		401.5	402	402	4.1	405.8	3.29	2.95	$\rho(O_h)$	YAP/LuAP
412.1	411.9	404.8	404.5	412		407.8			δ(Al–O–Al)	YAP
429.7	428.7	430	433	417		412.9			δ(Al–O–Al)	YAP
		455.4	451		4.2	459.1	–0.07	–0.43	$\nu_{as}(O_h)$ (equa.)	YAP/LuAP
466	468.4			469		464.3			$\nu(O_h)$ (ax./equa.)	YAP
471		466	462	466		464.4			$\nu_{as}(O_h)$ (equa.)	YAP/LuAP
		486.6								LuAP
538	538.3	539	538	540	6.4	538.3	2.66		δ(Al–O–Al)	YAP (on edge)
		539	538	537		539.1			$\delta(O_h)$ (equa.)	YAP/LuAP
552	551.9	550	550	553	6.3	551.2	2.85		$\nu_{as}(O_h)$ (equa.)	YAP/LuAP
		569	569		6.2		2.75			LuAP
598	596	598		587	6.1	588.3	1.55		$\nu_s(O_h)$ (equa.)	YAP
		621.6	620		5		2.03	1.8		LuAP
		668.3								LuAP
687						679.5			$\nu_s(O_h)$ (ax.)	YAP
		708				701.4			$\nu_s(O_h)$ (equa.)	YAP/LuAP
735	736					733.1			$\nu_s(O_h)$	YAP
		771								LuAP

VII.2.5. Results of high–pressure spectroscopic measurements

VII.2.5.1. Luminescence under HP

Luminescence measurements were carried out on $LuAlO_3:Ce^{3+}$ bulk crystals and $LuAlO_3:Ce^{3+}$ single crystalline films (SCFs) (see Fig. 30a and Fig. 30b, respectively) under excitation with a 275 nm laser line, and the results were recorded as a function of pressure. The luminescence spectra of both samples were found to be very similar, showing an asymmetric band composed of at least two Gaussians. As pressure was increased, both luminescence peaks (Gaussians) shifted towards longer wavelengths and their intensity decreased. The decrease in intensity was attributed to the movement of the *5d* levels under pressure, while the excitation wavelength remained constant.

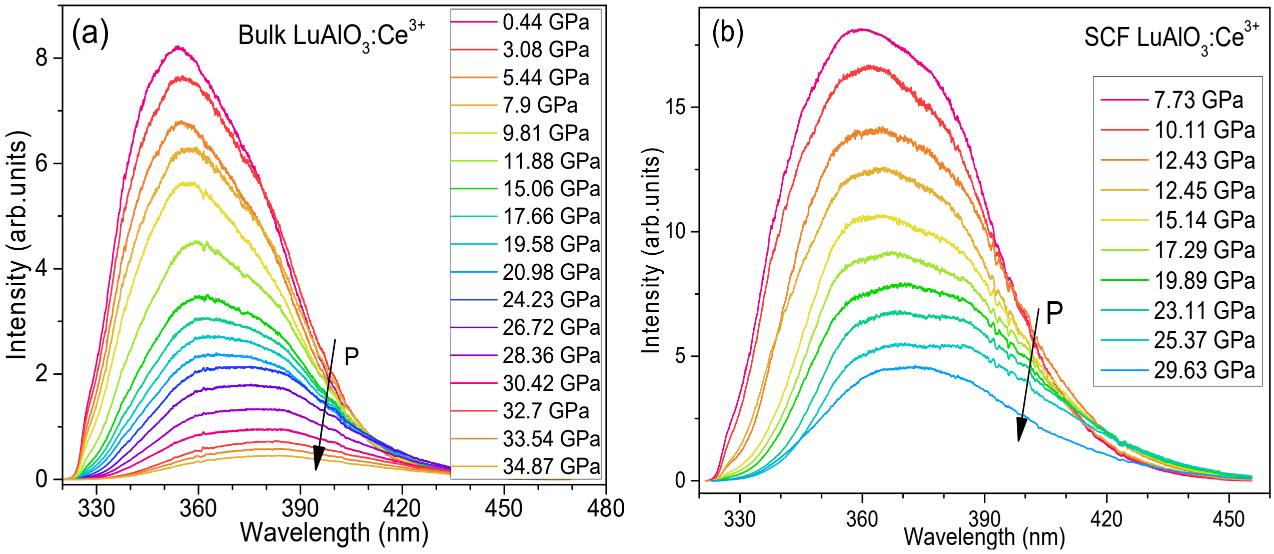

Fig. 30. Room temperature luminescence spectra of Ce^{3+} in $LuAlO_3$ single crystal (SC) (a) and single crystalline film (SCF) (b) under high pressure. The luminescence was excited with the 275 nm laser line and a 325 nm edge filter was used to cut off the laser excitation.

All spectra were fitted with two Gaussians, and the peak positions were plotted as a function of pressure for the SCF and SC samples (Fig. 31a and Fig. 31b, respectively). As the *4f* electrons are shielded from the crystal field, no significant changes in the level positions were expected. However, the *5d* electrons are much more affected by the crystal field, and therefore the pressure–induced changes in luminescence peak energies mainly reflected the changes in the *5d* level position, from which the emission originated. The energy distance between the two emission lines remained almost constant.

Both luminescence lines exhibited a red shift as pressure increased, with a distinct bending point observed above 15 GPa for the SCF sample (see Fig. 31a and Fig. 31b). The redshift of the peak energies in the bulk crystal could be approximated by two linear dependences with shift rates of 16 and 19 cm^{-1}/GPa below 20 GPa and 47 and 54 cm^{-1}/GPa above 20 GPa. The relative intensities of the higher to lower energy luminescence peaks decreased linearly with pressure up to about 15 GPa in the film and 20 GPa in the single crystal, after which the dependencies changed noticeably (see Fig. 31c and Fig. 31d). This trend was well–correlated with that of the peak positions. The presence of two Gaussians supported the observation that the emission arose not only from the lowest–lying *5d* band but also from the higher components of the excited *5d* states, which were thermally populated even at room temperature.

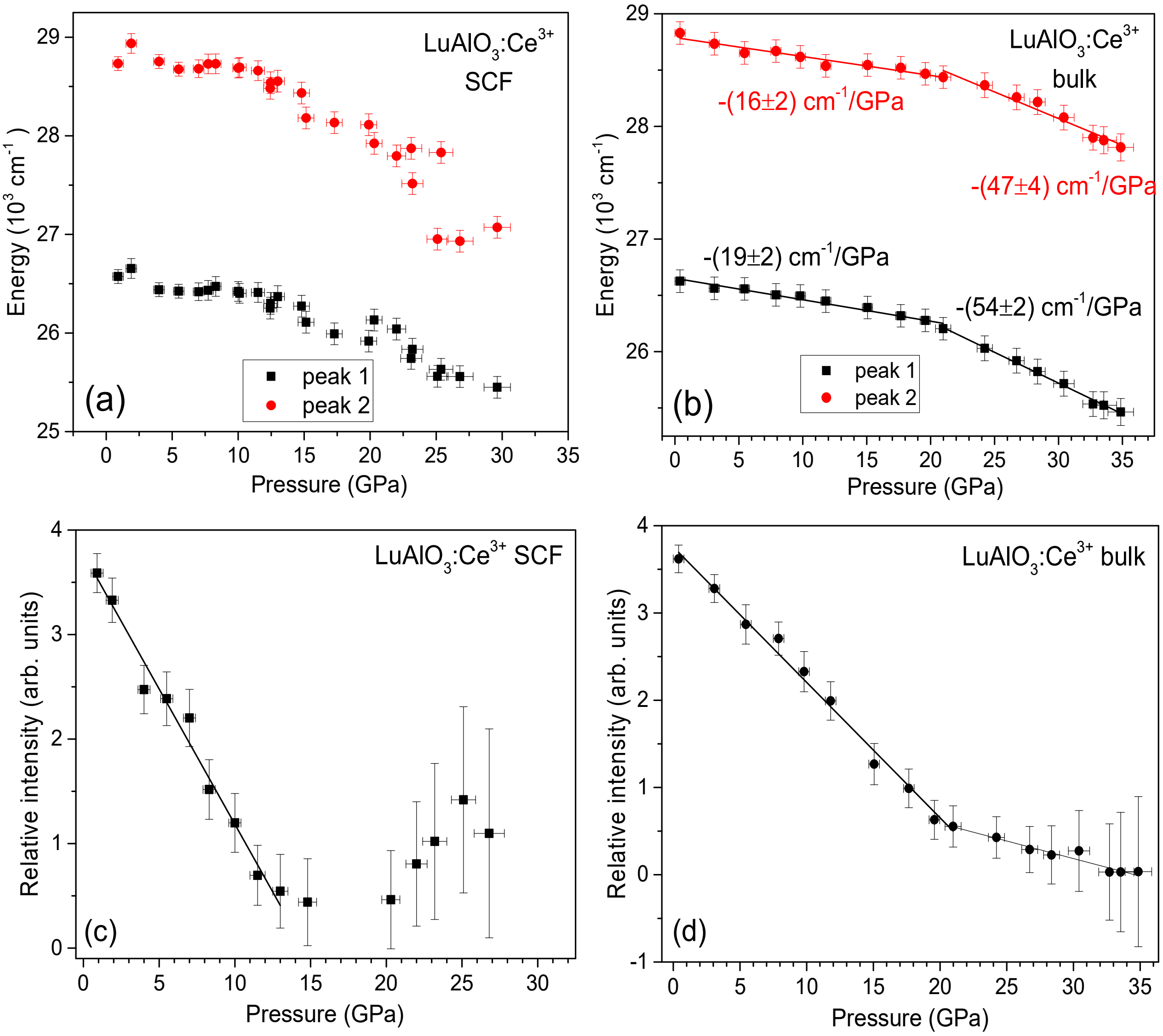

Fig. 31. Energies (a, b) and relative intensities(c, d) of Ce^{3+} luminescence peaks associated with the 5d→$^2F_{5/2}$ and 5d→$^2F_{7/2}$ transitions vs. pressure in SFC and SC samples, respectively. The linear fits of the slopes are given in (b).

The change in shift rates observed in both samples at different pressures (around 15 GPa in the SCF and around 20 GPa in the SC) suggested possible structural changes taking place. One possible explanation is a phase transition occurring in this pressure range. In the case of the SCF sample, the pressure dependences of the peak energies were not quite parallel, indicating some influence of pressure on the *4f* electronic states. This could lead to changes in the splitting of the *4f* states, as well as changes in the distance between the lowest–lying *5d* levels, which could affect the population of the *5d* states. As a result, the luminescence would be initiated from more than one level, especially at higher temperatures.

However, attempts to deconvolute the luminescence into more than two bands would increase the number of fitting parameters, making such a procedure less reliable.

The different pressures at which the change of shift rates is observed, around 15 GPa in SCF and around 20 GPa in SC samples, suggest that the bulk crystal is more pressure–resistant than the thin film. This difference in behavior could be related to the larger number of defects in the thin film, which appear to play a role in stabilizing the crystal structure. The lower defect concentration in the film than in the bulk crystal could be attributed to the much lower growth temperature. In fact, LuAP SCFs are known to be prone to stress relaxation due to differences in lattice parameters between the substrate and the overgrown layer, which can even lead to breaking.

VII.2.5.2. Raman spectra under pressure

The pressure–dependent Raman spectra of the LuAP single crystalline film are shown in Fig. 32a, with the particular lines grouped according to their similar pressure dependences and marked on the graph with numbers from 0.1 up to 6.4. At low pressures, the lines below 150 cm^{-1} overlap with the Raman signal from Ar, which was used as the pressure transmitting medium, but the low energy vibrations of LuAP are still distinguishable. As pressure increases, most of the lines observed on the cross–section of the YAP/LuAP structure remain visible, but some lines, such as those from groups 1 and 6, disappear above 10 GPa. Almost all lines exhibit shifts towards higher energies, and the rate of the shift changes at a pressure of about 10 GPa, coinciding with the behavior of luminescence. The pressure dependences of the Raman line energies are shown in Fig. 32b, and the shift rates are listed in Table 3 for pressures below 10 GPa and above 10 GPa. As shown in Table 3 and Fig. 32, the pressure coefficients of Raman lines decrease after 10 GPa.

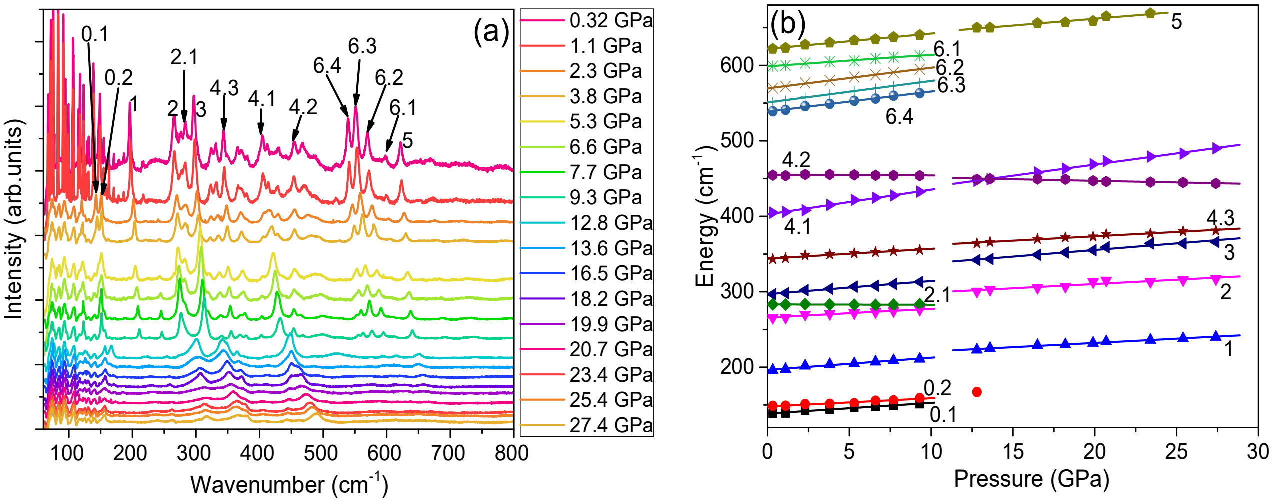

Fig. 32. Pressure–dependent Raman spectra of LuAP SCF. (b) Positions of Raman peaks as a function of pressure.

An exception to the typical behavior of increasing energy of Raman modes with applied pressure is exhibited by line 4.2, the energy of which decreases with increasing pressure. This behavior is shown in Fig. 33a, and the shift rates for this line also change at a pressure of about 10 GPa, from –0.07 cm^{-1}/GPa below 10 GPa to –0.47 cm^{-1}/GPa above 15 GPa. This type of behavior is similar to that of the so–called soft mode observed, for example, in ferroelectric materials, where a further increase of the pressure leads to a ferroelectric/paraelectric structural phase transition [125]. This suggests that a phase transition may be responsible for the observed shift changes in pressure coefficients of the luminescence bands and Raman lines.

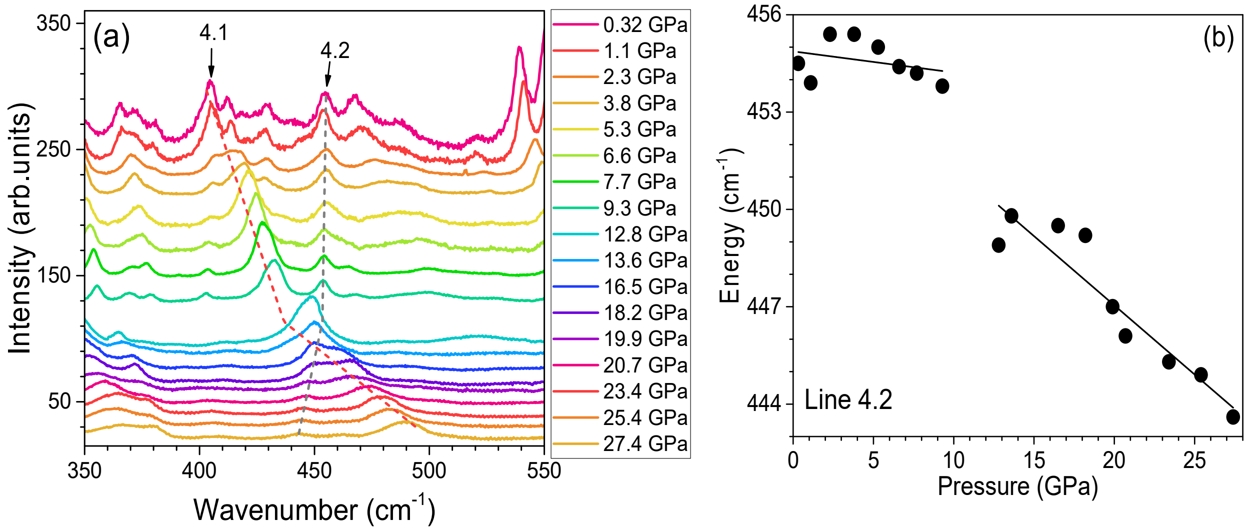

Fig. 33. Raman peak with diminishing energy for LuAP SCF (a) and its energy as a function of pressure (b)

However, another interpretation of this effect is also possible. Specifically, the energy of certain vibrations in the perovskite lattice may depend not only on the lattice parameters, which increase the energy with pressure, but also on the angle of deviations of the octahedra forming the lattice, which may cause changes in the force constants between the vibrating species [126]. Due to such distortions, the force parameters may decrease, causing the energies of certain lattice vibrations to decrease with increasing pressure. The vibrations around 400 cm^{-1} are associated with Al–O stretching and deformation modes in the parent $YAlO_3$ compound [127]. These effects do not exclude the possibility of an abrupt change in the already mentioned angle of distortion occurring at a certain pressure.

VII.2.6. Theoretical calculation of the band–gap energy as a function of pressure

All theoretical calculations presented in this chapter were conducted by Professor M. G. Brik.

The results of the theoretical calculations performed for LuAP using two approximations, GGA and LDA, are presented in Fig. 34. The relative changes in unit cell volume under pressure are shown in Fig. 34a. Using the calculated data, the bulk modulus and its pressure derivative were determined from the fit to the Murnaghan equation of state [128]. Both approximations give similar values of these parameters (shown in the graph) and are in good agreement with the data already published for YAP [129].

The calculated pressure dependence of the LuAP bandgap energy is shown in Fig. 34b for both approximations. As is typical for these calculations, the value of the bandgap energy is underestimated, although the pressure changes of this parameter are usually in better agreement with experimental data [130, 131]. However, as can be seen, the GGA and LDA approximations give quite different pressure dependences of the LuAP bandgap energy. This is most likely related to the relatively close energies of the direct and indirect bandgaps, similar to the energy structure of YAP [19]. Unfortunately, it is impossible to directly measure this dependence due to diamond absorption, which prevents performing such an experiment. The results of GGA predict that the LuAP bandgap strongly increases with applied pressure, but at higher pressures, a very strong bowing is observed when the indirect bandgap prevails over the direct one. This effect is observed at pressures higher than 15–0 GPa. From LDA calculations, a very weak influence of pressure on the bandgap energy is expected. The pressure dependences of the bandgap energy derived from both theoretical methods can be approximated by quadratic functions, shown in Fig. 34b with appropriate parameters.

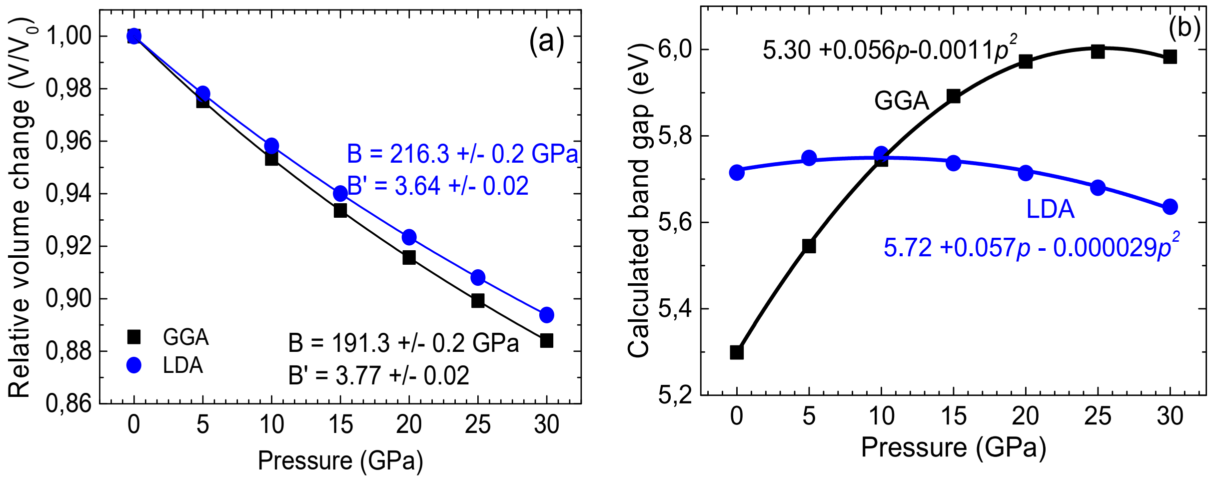

Fig. 34. Calculated pressure dependences of the relative unit cell volume (a) and bandgap energy (b) of LuAP using GGA and LGA approximations. Fitted values of bulk moduli and their pressure derivatives are given in (a) for both approximations. The bandgap pressure dependences can be fitted with quadratic functions presented in the graph.

VII.2.7. Discussion

VII.2.7.1. Calculations based on the Dorenbos model

The red shift of Ce^{3+} luminescence observed in high–pressure experiments is attributed to the compression and distortion of the crystal lattice. The physical mechanisms leading to the redshift are three–fold: (i) a downshift of the barycenter (centroid) of *5d* levels, ε_c, compared to the free ion, (ii) an increase in the crystal field splitting of the *5d* states, ε_{cfs}, and (iii) distortion of the oxygen polyhedron surrounding Ce^{3+} from cubic symmetry. The first two mechanisms can be evaluated as follows: The downshift of the centroid can be described by the following formula, adapted from previous works [132, 133, 134]:

$$\varepsilon_c = A\sum_{i=1}^{N}\left[\frac{a_{sp}^{i}}{(R_i-0.6\Delta R)^6}\right] \qquad (13)$$

Here R_i is the distance (in picometers) between Ce^{3+} and anion i in the undistorted lattice. Pressure application changes these distances. The summation is over all N ($N = 8$) anions that coordinate Ce^{3+}. $0.6\,\Delta R$ is a correction for lattice relaxation around Ce^{3+}, ΔR is the difference between the radii of Ce^{3+} and Lu^{3+}, α_{sp}^{i} (in units of 0–30 m^{-3}) is the spectroscopic polarizability of anion i, and A is a constant (1.79 × 1013). The polarizability α_{sp}^{i} can be evaluated using the formula:

$$\alpha_{sp}^{i} = 0.33 + 4.8/\chi_{av}^{2} \tag{14}$$

Here χ_{av} is the weighted average of the electronegativities of the cations in the oxide compounds.

The contribution of the splitting of the *5d* state by the crystal field can be evaluated from the empirical formula:

$$\varepsilon_{cfs} = \beta_{poly} R_{av}^{-2} \tag{15}$$

Here R_{av} is the average distance between the activator and the neighboring anions, and β_{poly} values are 1, 0.89, 0.79, 0.42 for octahedral, cubic, dodecahedral, and tricapped trigonal prismatic coordination, respectively. The value $\beta_{octahedral} = 1.35 \times 109\ pm^2/cm$ [135].

Crystal field splitting of the *5d* levels is also dependent on the distortion from the cubic geometry of the octahedron, which is more difficult to evaluate.

R_i (pm)	1	2	3	4	5	6	7	8	R_{av}
YAP	223,7	230,61	228,43	228,43	248,07	248,07	256,91	256,91	240,14
LuAP	219,47	224,35	223,54	223,54	243,75	243,75	254,07	254,07	235,82

Table 4. The distances between Y–O, and Lu–O ions

The results of calculations based on the Dorenbos theory [133] and ambient pressure data, using distances between the cation and surrounding oxygens taken from [136] for YAP and from [126] for LuAP, respectively, are presented in Table 5. The distances R_i are taken from [136, 137] and are listed in Table 4. To calculate formulas (13) to (15), the remaining necessary data are the electronegativities: Y – 1.22; Al – 1.61; Lu – 1.27. It is assumed that Y, Lu, and Ce ions are located in dodecahedral (however strongly distorted) crystallographic positions, and thus the values of $\beta_{dod} = 0.79 \times \beta_{oct}$. The experimental positions of the barycenters of *5d* states of Ce^{3+} ions, estimated from the integral of absorption measurements of all *5d* transitions for each compound (see Fig. 26), are also given in Table 5. The barycenter energies obtained as the mean energy of the absorption peaks are also presented. The experimental values are compared to theoretical ones, obtained by subtracting the calculated centroid shift, ε_c, from the *5d* barycenter for the free Ce^{3+} ion, which is 6.35 eV (51 230 cm^{-1}) [134]. The crystal–field splitting, ε_{cfs}, is defined as the energy difference between the lowest and highest *5d* level. A fraction of ε_{cfs} contributes to the total downshift. Our estimations show that this fraction is equal to about 0.65 at ambient pressure and was kept constant in the calculation of pressure dependences. Fig. 35 presents a schematic picture of the energy structure of Ce^{3+} ions in YAP and LuAP under ambient and high pressure.

Parameter	YAP:Ce		LuAP:Ce	
	theory (eV)	experiment (eV)	theory (eV)	experiment (eV)
Bandgap energy		7.63		7.86
ε_c	2,58		3.06	
ε_{cfs}	2,30	1.68	2.38	2.17
Theoretical barycenter energy $E^{5d}_{free} - \varepsilon_c$	3.77		3.29	
Experimental barycenter energy (vs. *4f* state energy)		(4.76)*		(4.86)*
Theoretical (ε_c+0.65×ε_{cfs}) and experimental (ε_c–0.65×ε_{cfs}) down–shift**	ε_c+0.65×ε_{cfs} 4.08	ε_c – 0.65×ε_{cfs} (3.67)*	ε_c+0.65×ε_{cfs} 4.61	ε_c – 0.65×ε_{cfs} (3.56)*
The energy of the lowest *5d* level E^{5d}_{free} – down shift	2.28	4.05	1.74	4.03
The energy of the lowest *5d* level referenced to the band–gap	3.55	4.05	3.24	4.03

* *Calculated as an average of level peaks energies.*

** *The difference in sign of ε_{cfs} comes from different reference levels*

Table 5. Calculated from equations (13)–(15), and experimental values of the downshift of the centroid barycenter, ε_c, the splitting of the 5d state by the crystal field, ε_{cfs}, and related data at ambient pressure (see description below).

The calculated theoretical energies of the lowest–lying *5d* Ce^{3+} states in YAP and LuAP referenced to the free–ion energies do not agree with the values obtained from absorption measurements, as shown in Table 5. The theoretical values are about half as large as those observed experimentally. However, a better agreement is achieved for the total splitting energy of the *5d* states, ε_{cfs}.

The *5d* barycenter energy of Ce^{3+} in LuAP was estimated to be 5.22 eV if calculated from the integrated absorption to the *5d* states. This value is much larger than the average of the observed peak energies of the five *5d* states of Ce^{3+}, which is equal to 4.86 eV. The value obtained from the integration of the absorption coefficient is affected by the relatively large background present in the LuAP crystal close to the conduction band. The *5d* barycenter in LuAP estimated from the integrating procedure is located between the two highest–lying *5d* levels. In contrast, in YAP, the *5d* barycenter energies of Ce^{3+} are calculated both as an average of the peak energies and from the integration of the absorption coefficients, and they agree with each other (see Table 5). The better agreement in YAP is a consequence of the much lower background absorption than in LuAP. Therefore, the experimental Ce^{3+} *5d* barycenter energy in LuAP is better taken as equal to 4.86 eV, from the average position of *5d* levels peak energies.

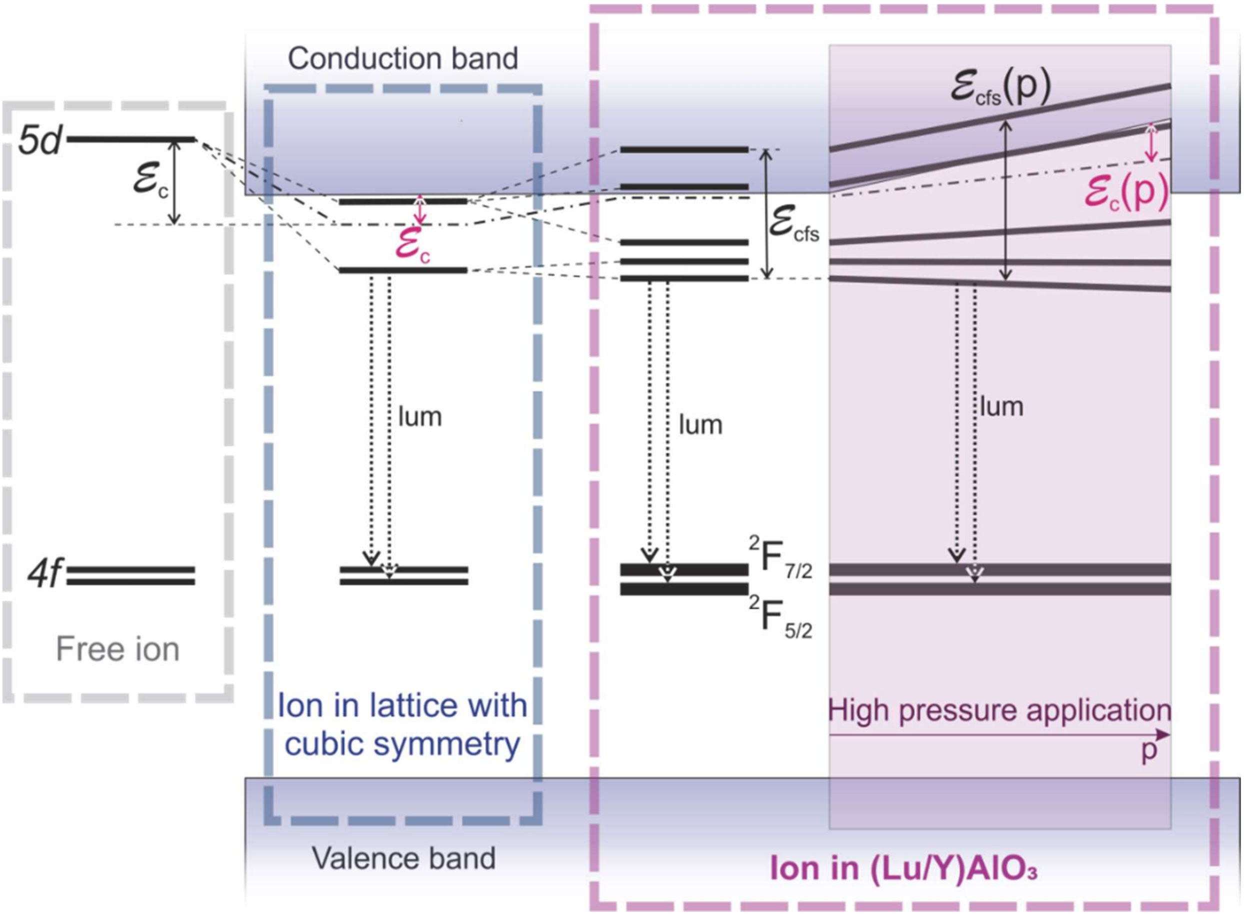

Fig. 35. Schematic energy structure of Ce^{3+} ions in YAP and LuAP under high pressure.

The theoretical energies of the *5d* level positions much better correlate with the experiment if they are calculated from the bandgap energies instead of the free Ce^{3+} ion *5d* state energy. The results of such calculations are shown in the last row of Table 5. Nevertheless, the difference of about 0.8 eV is still present in the case of LuAP:Ce^{3+}. The energy of the bandgap is very close to the energy of the Ce^{3+} to Ce^{4+} charge transfer process [138].

VII.2.7.2. Dependence of the *5d–4f* energies on pressure

It is now possible to calculate the pressure dependence of the energies of the *5d–4f* luminescence bands in LuAP:Ce, assuming that all distances between Ce^{3+} ions and the surrounding ligands change according to the modified Murnaghan equation of state [129] (this assumes that the distances under pressure change as $V^{1/3}$):

$$\frac{R_0}{R_p} = \left(\frac{pB_0'}{B_0} + 1\right)^{\frac{1}{3B_0'}} \tag{16}$$

Here R_0 and R are Ce^{3+} – oxygen distances at ambient and applied pressures, respectively, and B_0 and B_0' are values of the bulk modulus and its pressure derivative (see, for example, [139]). By fixing the theoretical positions of the *5d–4f* band maxima to the experimental positions at ambient pressure, the theoretical pressure dependences of the luminescence bands were calculated. These are shown in Fig. 36 as broken lines. The apparent discrepancy between experimental and theoretical data can be corrected by taking the position of the conduction band bottom as a reference level instead of the free–ion *5d* level energy. The best fit to the experimental data is obtained if a linear shift of the conduction band minimum with pressure, equal to 310 cm^{-1}/GPa, is assumed (see solid blue lines in Fig. 36).

Taking the pressure dependence of the bandgap calculated with the use of LDA (red lines in Fig. 36) leads to results very similar to those obtained using a fixed reference level, which is not in agreement with the experimental data. The dependence calculated with the use of theoretical GGA predictions (green solid lines) gives good agreement for pressures up to about 15 GPa, but at higher pressures, the theoretical lines deviate from the experimental data.

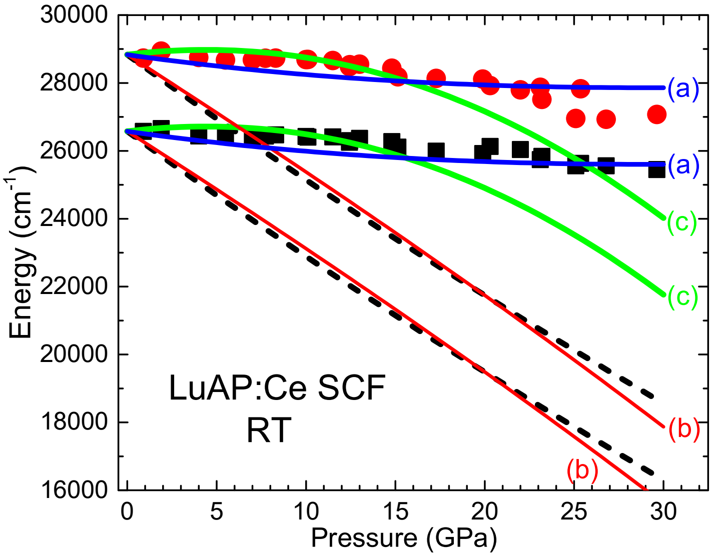

Fig. 36. Pressure dependences of 5d→4f transitions calculated from Dorenbos theory. Broken lines show dependences calculated according to Eqs. 1–4, solid lines present dependences calculated taking into account changes of the energy of conduction band minimum. Blue lines: linear pressure dependence of the band gap energy(a); red lines: band–gap calculated with LDA (b); green lines: band gap calculated using GGA (c).

There is no experimental data on the pressure dependence of the bandgap energy of LuAP due to its high energy, which coincides with the bandgap of diamonds. However, both the linear dependence of the bandgap energy and that calculated with GGA are in reasonable agreement with what is typically observed in similar compounds, such as YGG [120]. Therefore, using the bandgap energy as the reference level is postulated instead of the free Ce ion *5d* energy usage. This small correction allows the correlation of experimental data with the Dorenbos model and is in line with his idea of the Vacuum Referred Binding Energy (VRBE) or Host Referred Binding Energy (HRBE) concept, which was relatively recently presented [140, 141].

The obtained results with linear dependence of the bandgap energy or that calculated with GGA exhibit good agreement between theory and experimental data, at least up to 15 GPa. They also highlight the importance of considering the pressure dependence of the band structure. It is not possible to neglect the pressure dependence of the energy of the conduction band minimum versus the position of the *4f* levels, which are treated as pressure–independent in this consideration. This is in agreement with the commonly accepted idea that *4f* states, being screened by outer electrons, are very weakly dependent on the environment. In contrast, *d* levels, especially *5d*, strongly interact with surrounding anions, and therefore their energy structure has a strong dependence on pressure.

Using the conduction band energy as the reference level for the calculation of the downshift energy ε_c can be justified by the close location of the intervalence charge transfer state (IVCT), which is formed by ionization of the Ce^{3+} ion followed by trapping of the ionized electron. This state can be understood as a (Ce^{4+} + e) exciton, and its energy level should lie close to the bottom of the conduction band depending on the electron binding energy [138].

Although there is a general agreement between theoretical considerations and experimental data, closer comparisons reveal important deviations that are detected by our measurements. Firstly, the bending of theoretical curves in Fig. 36 (for linear band–gap dependence) is opposite to the experimentally observed curve (compare with Fig. 31a and Fig. 31b). This discrepancy could be due to experimental details that were not taken into account in the theoretical considerations. For instance, the pressure dependence of the cation–anion distances may not be the same for all anions as assumed in Eq. (15). The local compressibility of the polyhedron around Ce^{3+} may also be different from the average described by Murnaghan's equation, and the distortion from cubic symmetry may result in stronger splitting than described by Eq. (14). Finally, a certain type of phase transition may occur at pressures between 15 and 20 GPa, which is suggested by changes in the pressure coefficients of the Raman spectral lines that also occur at similar pressures.

Moreover, the deviation of the theoretical pressure dependence of the $5d \rightarrow 4f$ transitions for the band–gap calculated with GGA above 15 GPa from the experimental data may be associated with this phase transition. We do not expect this phase transition to lead to a different crystallographic structure or different space group symmetry. However, it is possible that the angles at which the octahedra containing Al ions are placed in the lattice may undergo an abrupt change under pressures in the range of 15 to 20 GPa. This change will not affect the symmetry of the crystal lattice but may impact the rigidity of the crystal structure, allowing for significant changes in the pressure coefficients of the phonon modes and luminescence peaks.

A certain type of phase transition is the most likely explanation for the observed change in pressure coefficients of the Ce^{3+} $5d \rightarrow 4f$ transitions at approximately 15 GPa in the free–standing layer and slightly higher pressure in the crystal grown using the micro–pulling down technique. A similar effect was previously observed in [142], which was associated with a certain reconfiguration of octahedrons containing Al ions but without a change in the general structure, such as the compound's space group. A similar effect was also discussed above in chapter VII.1, page 46, in the *R*AP:Eu^{3+} layers (you can also see [17], where results from chapter VII.1 are published). The different pressures at which this transition occurs in the free–standing LuAP layer grown by liquid phase epitaxy and in the crystals grown by micro–pulling down may be due to different types of defects present in both materials, particularly in the LuAP crystals grown at high temperatures (2000°C) compared to their SCF counterparts (~1000°C). Specifically, the concentration of Lu_{Al} antisite defect and oxygen vacancies, as well as their aggregates, is substantially higher in SC than in SCF [143]. Moreover, the concentration of uncontrollable rare earth impurities seems to be higher in SC than in SCF. A relatively large number of unidentified rare earth impurities were detected by luminescence measurements of SC.

The possibility of a phase transition is further supported by high–pressure Raman measurements shown in Fig. 32. In this experiment, the change in pressure coefficients of various lines is also observed in a similar pressure range (above 10 GPa). The observation of a soft mode in the Raman spectra, which is a characteristic feature of possible phase transitions, provides additional evidence that such a transition may be occurring in the studied material.

VII.3. Study of $CsPbBr_3$

VII.3.1. Absorption of $CsPbBr_3$ as a function of temperature

VII.3.1.1. Experimental result and initial processing

Absorption spectra of $CsPbBr_3$ were measured at various temperatures. Before the measurement, the sample was polished using fine aluminum oxide powder with a declared average grain size of 12.5 μm, followed by washing with acetone to remove any leftover polishing residue. The obtained results are presented in Fig. 37.

As described in [57], the Boltzmann function can be used to fit absorption data (see fitting in Fig. 37a, d). Equation (5) provides the fitting function, and the detailed explanation of why to use it is in chapter V.3.2, page 20. Based on the findings in [57], both direct and indirect band gaps can be calculated from the Boltzmann function fit using the relevant equations.

$$\alpha(E) = \alpha_{max} + \frac{\alpha_{min} - \alpha_{max}}{1 + e^{\frac{E-E_0}{\Delta E}}} \tag{5}$$

$$\begin{aligned} E_{dir} &= E_0 - n_{dir}^{coeff} \times \Delta E \\ E_{ind} &= E_0 - n_{ind}^{coeff} \times \Delta E \end{aligned} \tag{17}$$

Here, E_{dir} (E_{ind}) is the direct (indirect) band gap; E_0 and ΔE are fitting parameters from equation (5); and $n_{dir}^{coeff} \cong 0.3$ and $n_{dir}^{coeff} \cong 4.3$ are coefficients, taken from [57]. These values were obtained empirically by comparing the direct and indirect band gaps obtained from linear fittings with those obtained from Boltzmann fittings. In this study, the direct and indirect band gaps of $CsPbBr_3$ were determined using the Boltzmann fitting approach described by equation (17) (see Fig. 36a and d). Additionally, linear fittings of the square and square root of the absorption spectra were performed (see Fig. 37b, c, e, and f). The results obtained from these two methods were compared, and it was found that the obtained values were almost identical, as shown in the inset of Fig. 38. Although the Boltzmann function lacks a physical basis for absorption spectra fitting, the consistency between the results obtained in this study and the findings in [57] confirm that it produces mathematically equivalent to the Taucs' plots outcomes.

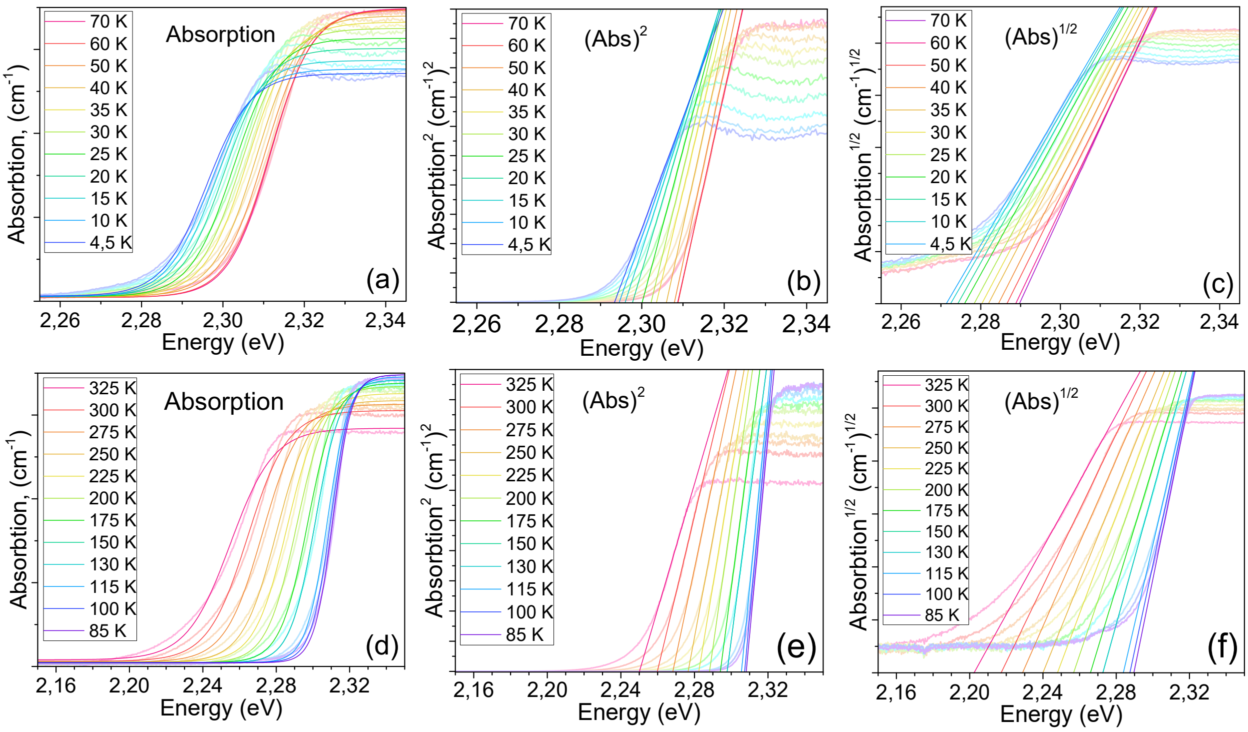

Fig. 37. Absorption spectra of CsPbBr$_3$ as a function of temperature. In a, b, and c temperature region from 4.5 to 70 K is shown, while in d, e, and f – from 85 K up to room temperature region is presented. In a and d absorption coefficient is fitted with the Boltzmann function, while in b and e, and c and f square and the square root of the absorption coefficient is fitted with a straight line.

The absolute value of the band gap of CsPbBr$_3$ has been reported with slight variations in different works, which can be attributed to the use of different methods for estimating the band gap energy and differences in sample quality, including crystal quality and defect concentrations. For instance, corresponding works have reported values of 2.25 eV [44, 80], 2.252 eV [43], 2.3 eV [73,144], 2.32 eV [51], 2.35 eV [72], and 2.36 eV [62] (all presented values are for ambient conditions). In this work, the band gap is underestimated, most probably due to additional subband absorption from defects and dynamic structure fluctuations (see details in chapter V.3.3, page 24). Nevertheless, the results presented in this work are consistent with typical values for CsPbBr$_3$, and reasonable values are obtained for the fitting of the band gap temperature dependence (Fig. 38).

The band gap of CsPbBr$_3$ is known to be direct at ambient conditions (see [50, 51, 43, 44, 54]), hence data obtained from linear fitting of the square of the absorption is analyzed further (Fig. 38). The band gap of CsPbBr$_3$ increases with temperature up to around 80 K, after which it decreases, contrary to the expected behavior of a band gap decrease with temperature due to electron–phonon interaction. The linear expansion of the band gap with temperature, discussed in chapter V.3.2.2, page 22, also needs to be considered for CsPbBr$_3$. Both effects (the linear expansion and the electron–phonon interaction) are taken into account in the equation from [65]:

$$E_g(T) = E_0 + BT - \frac{2a}{e^{\frac{h\nu_{ph}}{k_B T}} - 1} \tag{8}$$

Here E_0 is the band gap energy at zero temperature, the second term corresponds to the thermal expansion of the band gap with rate B, and the third term includes electron–phonon interaction. The weight of the electron–phonon interaction *a*, the phonon energy $h\nu_{ph}$, and the Boltzmann constant k_B are considered in the third term. The fitting of band gap energy on temperature is shown in Fig. 38, with and without taking into account the zero–temperature vibrations, resulting in E_0 values of 2.36 eV and 2.29 eV, respectively. The obtained parameters are close to those reported in [65] for $CsPbBr_3$ quantum dots. Additionally, the obtained value of the phonon wavenumber, $\nu_{ph} = 151\ cm^{-1}$, is very close to the reported longitudinal optical (LO) phonon of $CsPbBr_3$ [77, 78].

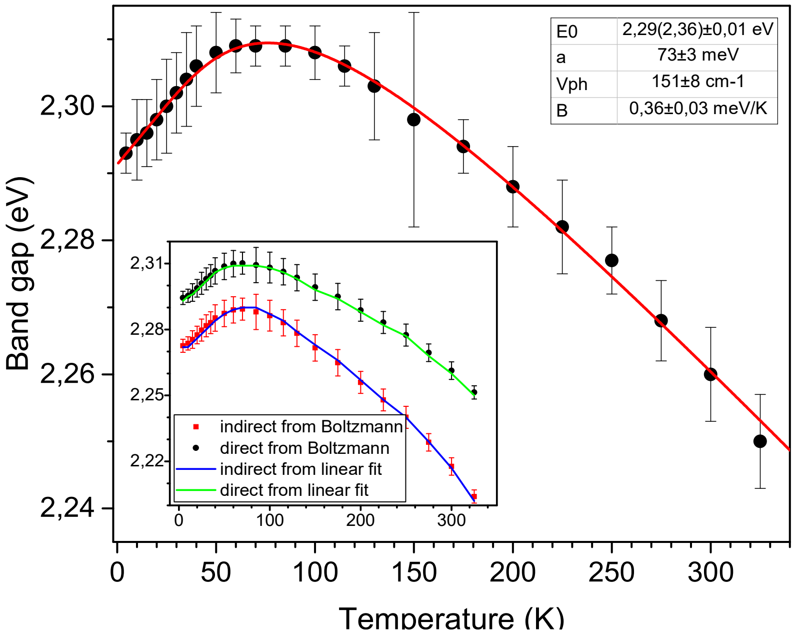

Fig. 38. Dependence of $CsPbBr_3$ band gap on temperature, taken from the linear fit of the square of absorption spectra. Fit in (a) is done by equation (8). Direct and indirect band gaps taken from linear fits are compared in the inset in (a) with the calculated from Boltzmann fitting

VII.3.1.2. Urbach states

The Urbach energy, also known as the so–called Urbach tail, was determined by fitting the absorption spectra using the exponential function given by the equation:

$$\alpha(E) = \alpha_0 e^{\frac{E}{E_U}} \tag{18}$$

Here α_0 and E_U are material constants, with E_U representing the Urbach energy, which characterizes the slope of the absorption edge.

The obtained Urbach energies are plotted as a function of temperature in Fig. 39. The dependence of the Urbach energy on temperature was fitted using the modified expression previously reported by Cody et.al. [145] and applied to $CsPbBr_3$ in [72]:

$$E_U = \frac{\hbar\nu_{ph}}{\sigma_0}\left(\frac{1+X}{2} + \frac{1}{e^{\frac{\hbar\nu_{ph}}{k_B T}} - 1}\right) \tag{19}$$

Here, $\hbar\nu_{ph}$ is the average phonon energy, X is a measure of the structure fluctuation, σ_0 is the steepness parameter, and k_B is the Boltzmann constant. The results of the fitting are presented in the tables in Fig. 39, with two temperature regions used for fitting. The first fitting includes the entire available temperature range and is shown in red color in Fig. 39, with an obtained phonon wavenumber of 193 cm^{-1}. However, the discrepancy between this value and the value obtained from fitting the band gap dependence on temperature (see Fig. 38) suggests that either the band gap fit or the Urbach fit is incorrect. Therefore, a second fitting is done, starting from 50 K and shown in green color in Fig. 39. The obtained phonon wavenumber is 155 cm^{-1}, which is in good agreement with the value obtained in Fig. 38.

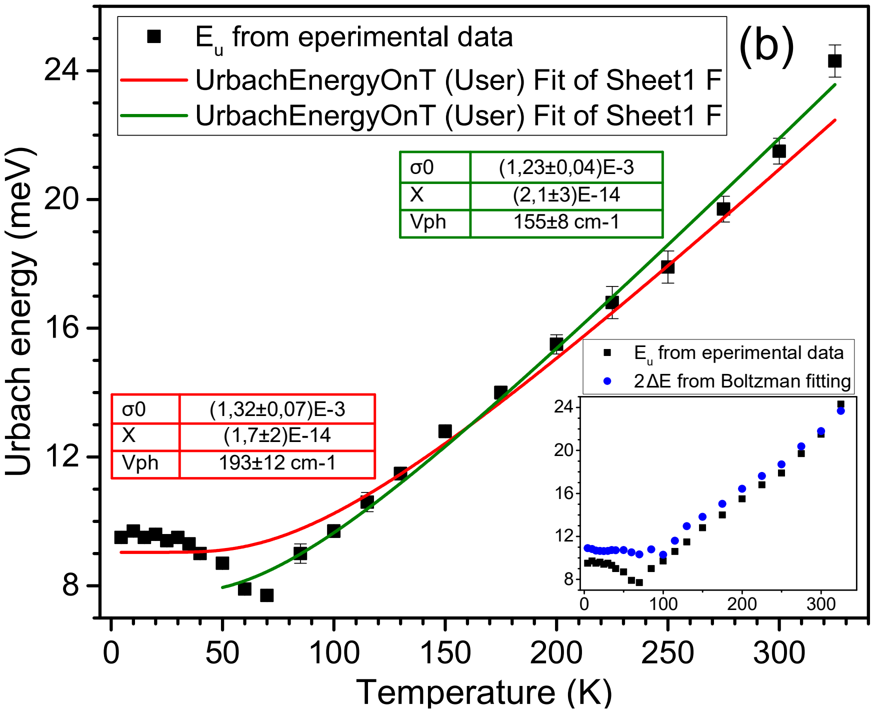

Fig. 39. Urbach energy as a function of temperature with fits, done by the equation (19). In the inset, Urbach energy is compared with the doubled ΔE parameter from the Boltzmann fit of the absorption spectra in the inset

It is important to emphasize that the estimation of the Urbach energy is not straightforward, as it requires very precise absorption measurements. The experimental data should have a change in the absorption coefficient between the minimum and maximum values of at least two orders of magnitude. In this work, our absorption spectra only changed in one order of magnitude, so a high error in Urbach energy estimation is unavoidable. This could be the reason for the unnatural drop of the Urbach energy with the temperature increase from 4.5 up to 50 K, and it may explain the incorrect values obtained when the fitting is done in the entire temperature range (red curve in Fig. 39).

Despite the limitations in the precision of the absorption measurement, these results are presented here because they are in good agreement with other works. For example, the absolute value of the Urbach energy at room temperature (24 meV) is in good agreement with [73]. The shape of the Urbach energy dependence on temperature is also similar to the data obtained in other works (see, for example, [71, 72]).

In the inset of Fig. 39, the Urbach energy is plotted together with the doubled parameter from the Boltzmann fit of the absorption spectra (*2*ΔE*, where *ΔE* is the parameter from equation (5)). As shown in the inset, the absolute value of $2*\Delta E$ and its temperature dependence are very close to the Urbach energy. This confirms the assumptions about the meaning of the ΔE parameter made in chapter V.3.2, page 20.

VII.3.2. Raman spectra of $CsPbBr_3$

VII.3.2.1. Temperature dependence

Raman spectra were measured at ambient pressure as a function of temperature, and the results are shown in Fig. 40. No phase transitions were observed below room temperature, which is consistent with previous literature. However, a fast shift of the line and fast broadening of the lines were observed. The Raman lines of $CsPbBr_3$ below 150 cm^{-1} originate from the transverse optical (TO) phonons of [$PbBr_6$] octahedra [45, 74, 75]. Chapters V.3.3.3 (page 26) and V.3.3.4 (page 26) present a review of the literature regarding Raman spectra of perovskites. Table 6 shows that the positions of the Raman lines obtained in this work are in good agreement with other studies. The mean values of the phonon lines are 52 and 70, 75 and 81, and 129 and 132 cm^{-1} for the TO_1, TO_2, and TO_3 doublets, respectively. The relatively broad and weak band around 309 cm^{-1} is related to the second–order phonon mode [45, 74, 146] of the LO phonon, which is located around 155 cm^{-1} [77, 78].

In Fig. 40b, the line positions are plotted as a function of temperature. A previously unreported line positioned around 72.5 cm^{-1} at 8 K was observed, and it was traced up to around 200 K, where it merged with the TO_2–1 line. This line is referred to as the low–temperature phonon (LTP) since it can only be seen at low temperatures. The position of all lines shifts to lower energy as the temperature increases, except for the LO×2 line which remains constant.

Fig. 40c shows the full width at half maximum (FWHM) of the Raman lines as a function of temperature. All FWHM values increase with the temperature increase, except for the TO_1–2 line, which stops broadening and shifting towards lower energies (see Fig. 40) at temperatures above 150 K due to the movement of this line to the lower spectral limit of the set–up. The rate of FWHM increase with temperature is different for different lines. The explanation of this phenomenon will be discussed further.

The central peak, the origin of which is discussed in chapter V.3.3.3, page 26, is visible in the form of a background of the spectra. Fast broadening of the Raman lines, including the central peak, can be observed in the temperature dependence of the Raman spectra of $CsPbBr_3$ below room temperature (see Fig. 40c). Some explanations for this behavior, based on the literature review, can be found in chapters V.3.3.3 (page 26) and V.3.3.5 (page 27). This fast broadening of the lines is related to the structure fluctuation, which increases with the temperature. This behavior can even be considered as an order–disorder phase transition, which occurs around 60–80 K for $CsPbBr_3$. A similar case has been reported for $CsPbCl_3$ in [79].

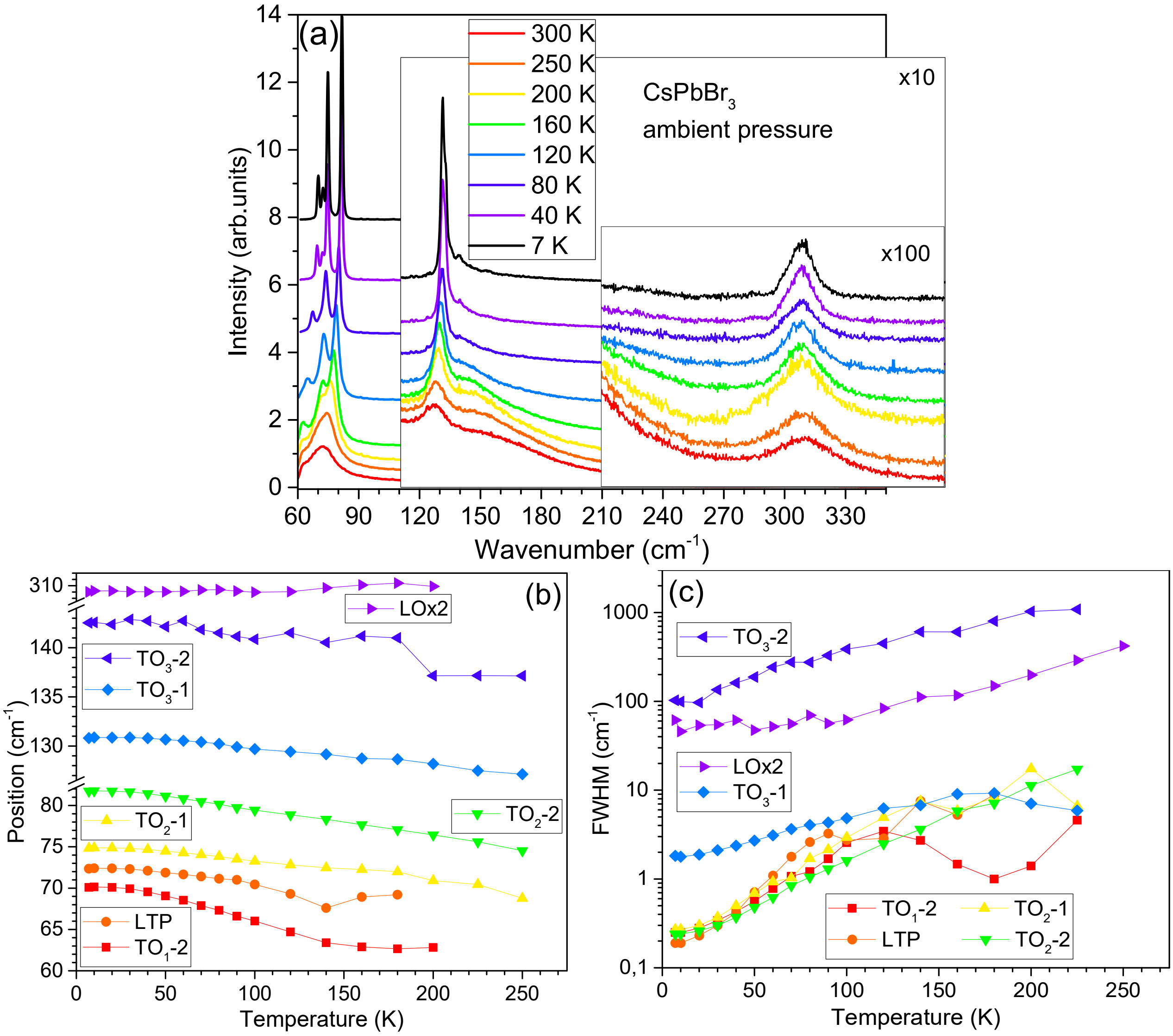

Fig. 40. CsPbBr3 Raman dependence on temperature (a), peak positions as a function of temperature (b), and full–width half maximum (FWHM) of few lines

As shown in Fig. 40b and c, some Raman lines shift and become broader with temperature faster than others. If we assume that both the position and FWHM of Raman lines are affected by the structure fluctuation, it follows that the degree of influence of the structure fluctuation on different lines from the Raman spectra is different. For instance, both the FWHM and the position of the TO_3 line change with the temperature much less than those of the TO_2–2 line. Hence, we can conclude that the TO_2–2 phonon is more strongly affected by the structure fluctuation than the TO_3 phonon.

VII.3.2.2. High–pressure dependence

Fig. 41 displays the high–pressure Raman measurements of the best–quality $CsPbBr_3$ crystal. At low temperatures (Fig. 41a, b), the Raman lines are more clearly resolved and reveal a phase transition around 1.2 GPa. At room temperature (Fig. 41d), the phase transition is visible at the same pressure. The authors in [51] concluded that with increasing pressure, [$PbBr_6$] octahedra rotate and Pb–Br distances decrease. However, above 1.2 GPa, Pb–Br distances are much harder to compress, giving rise to the isostructural phase transition of $CsPbBr_3$. In Fig. 41c, it is noticeable that TO_i ($i = 1, 2, 3$) lines shift slower above 1.2 GPa than at lower pressures, indicating a change in the compressibility of Pb–Br distances caused by the phase transition. Table 6 presents the pressure coefficients of $CsPbBr_3$ Raman lines at low temperatures for pressures below and above 1.2 GPa.

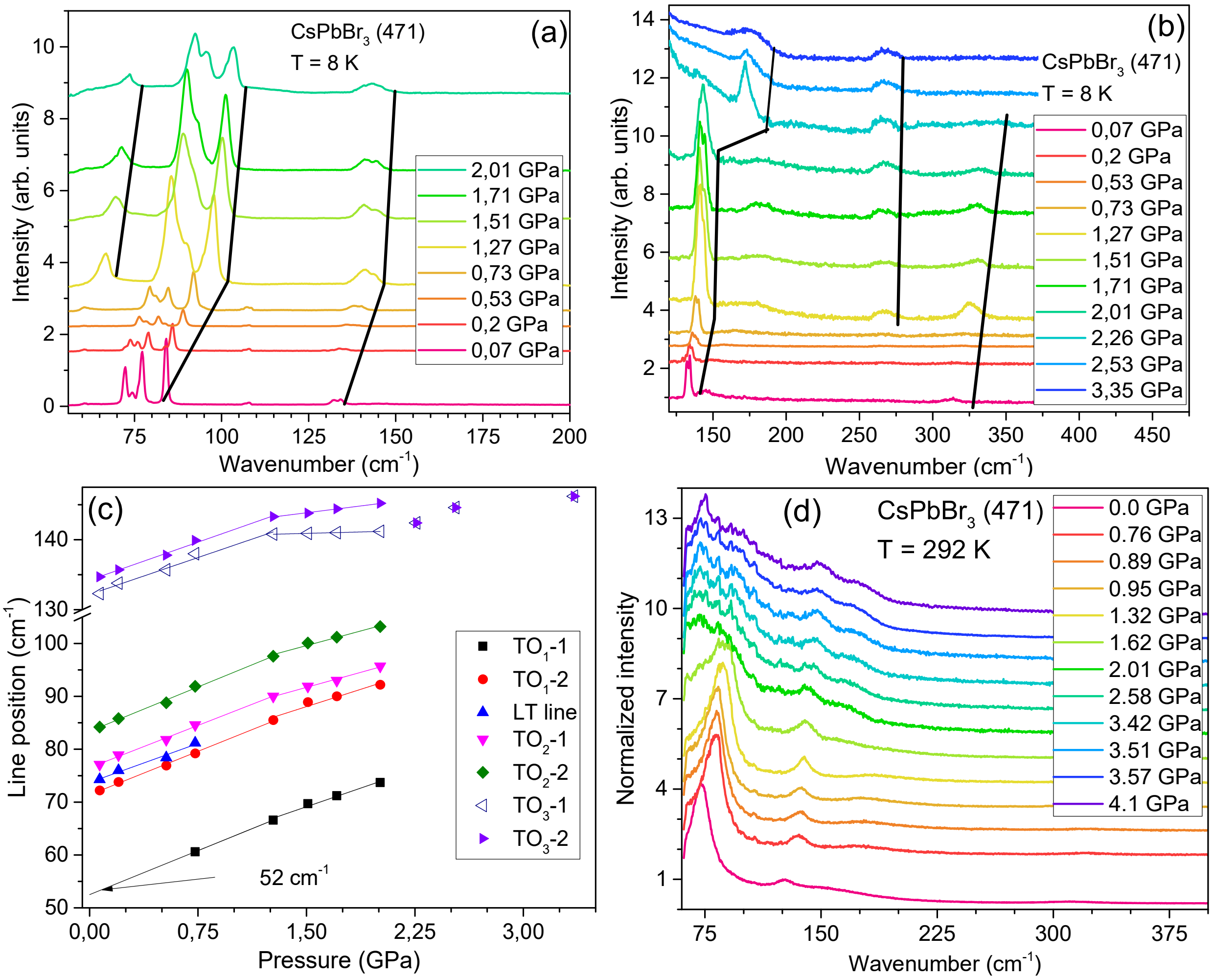

Fig. 41. Raman spectra of $CsPbBr_3$ with low defect number as a function of pressure at low ((a) and (b)) and room temperature (d). position of the Raman lines on pressure measured at low temperature (c)

The central peak present in all spectra in Fig. 41 is the increase of the background with the wavenumber decrease. The results presented in Fig. 41d confirm the findings reported by Long Zhang et al. in [51], where the central peak is more prominent at high pressures and room temperature. The intensity of the central peak increases with temperature (see Fig. 40a) and is attributed to higher structural fluctuations at room temperature than at low temperature (see the previous chapter). The intensity of the central peak also increases with pressure, which can be attributed to either the amorphization process or the transition to some high–pressure phase of $CsPbBr_3$. The previous studies report contradicting results regarding the high–pressure state of $CsPbBr_3$, with two main assumptions: amorphization and undefined high–pressure phase (see details in chapter V.3.1.2, page 20).

The set–up used in this study has a lower limit due to the usage of the filter that cuts light up to 60 cm^{-1} from the laser line. Therefore, lines below this value cannot be measured. The position of TO_1–1, equal to 52 cm^{-1}, was estimated from the fit of the high–pressure dependence (see Fig. 41c). The Raman line located around 28–29 cm^{-1} is taken from [67, 74], where low energy Raman spectra are studied. The origin of this line is not clear, and it is named a low energy phonon (LEP) in this work.

	LEP	TO$_1$		LTP	TO$_2$		TO$_3$		LOx2
		1	2		1	2	1	2	
83 K (cm^{-1}) from [75]	—	52	67	—	74	81	129	133	—
80 K (cm^{-1}) from [67, 74]	28-29	47	67	—	75	79	129	—	—
8 K (cm^{-1})	—	53	70	72.5	75	82	130	132	309
below 1.2 GPa ($\frac{cm^{-1}}{GPa}$)	—	11.1	10.0	9.8	10.7	11.2	7.0	7.2	10.6
above 1.2 GPa ($\frac{cm^{-1}}{GPa}$)	—	9.3	8.7	—	7.6	7.4	0.6	2.6	4.4
luminescence line (nm)	534.9	535.5	—	—	536.2	536.5	—	537.9	543

Table 6. Position of $CsPbBr_3$ Raman lines at low temperature and ambient pressure. Pressure coefficients of $CsPbBr_3$ Raman lines at low temperature. LEP is the shortening from low energy phonon, and LTP – low–temperature phonon

Table 6 also provides the wavelength of the luminescence line, which is further discussed in the following chapters. Phonon replicas from separate phonons are present in the luminescence spectra of $CsPbBr_3$. When the measured spectrum is completed by adding lines below 60 cm^{-1}, the combined spectrum agrees with the theoretically calculated phonon density of states presented in [147], except for a small underestimation of the phonon energies in the 12–25 meV (90–200 cm^{-1}) energy region.

VII.3.2.3. Summary and conclusions to chapter VII.3.2

$CsPbBr_3$ Raman spectra are atypical due to the presence of the central peak, which is discussed in detail in chapter V.3.3.3, page 26. This central peak appears as a background in the shape of broadband around 0 cm^{-1} and its intensity increases with temperature. It originates from structural fluctuations [67].

The temperature dependence of the $CsPbBr_3$ Raman spectra is atypical due to the influence of structural fluctuations on the regular phonon lines. This results in a fast shift and FWHF increase of the Raman lines. This effect is related to the interaction of regular phonons with structural fluctuations, which increase with temperature and lead to an order–disorder phase transition [79]. We assume that the Raman peaks are observed from different fluctuating lattices, resulting in broader peaks. This assumption is based on a similar one proposed in [67], where the authors consider $CsPbBr_3$ to fluctuate among many non–cubic phases, appearing on average as the cubic phase.

On the other hand, the pressure dependence of the Raman spectra is typical for $CsPbBr_3$, and this work's novelty lies in the low–temperature measurements of the $CsPbBr_3$ Raman spectra, which demonstrate that the same pressure–induced phase transitions occur at low temperatures and room temperature. At pressures above

2 GPa, $CsPbBr_3$ shows either amorphization or a phase transition to an undefined phase (see the previous chapter and chapter V.3.1.2, page 20).

VII.3.3. Luminescence of $CsPbBr_3$

VII.3.3.1. Low–temperature luminescence

The luminescence spectra of $CsPbBr_3$, measured at liquid helium temperature under 405 nm laser excitation, are shown in Fig. 42. Sharp lines at 534 nm and 542 nm correspond to the free and Rashba excitons, respectively. However, due to the overlap of the Rashba exciton with other lines, the exact position of the Rashba line is difficult to establish. Therefore, the position of the Rashba line at 542 nm is accepted as the mean value of many experimental results from this and other works. The line at 536 nm is the phonon replica of the free exciton. Broad lines around and above 540 nm are assigned to the defect luminescence. The Rashba exciton and defect lines overlap around 542 nm, making it difficult to separate them. The lines' origin is assigned following [42].

The Raman spectra are discussed in detail in Chapter VII.3.2, page 76. Due to the Raman set–up spectral limits, lines below 60 cm^{-1} were not measured. Therefore, to have all lines in the Raman spectrum, lines at 52 and 29 cm^{-1} are taken from other works [67, 92, 74] and marked in the spectrum in the form of delta functions (see Fig. 42). The longitudinal vibration (LO) with energy 155 cm^{-1} [77, 78] should also be taken into account. The obtained Raman spectrum is shown in Fig. 42a together with the luminescence spectra of $CsPbBr_3$ #471 (this number corresponds to the sample of the highest quality) measured in different points of the same sample. The Raman spectrum is shown again in Fig. 42c together with the $CsPbBr_3$ spectrum measured on the set–up with a higher resolution and under excitation of 355 nm instead of 405 nm. Judging from the position of the Raman lines, the phonon replicas of the free exciton can exist at 534.9, 535.5, 536.2, 536.5, 537.9, and 543 nm, which correspond to LEP, TO_1, TO_2, TO_2, TO_3, and the second order of LO, respectively.

Different parts of the same sample exhibit slight variations in luminescence, particularly in the region above 540 nm, which is not related to the phonon replicas (see Fig. 42a). This suggests that the sample is non–homogeneous and may have an uneven distribution of defects, as well as inclusions of other phases. In Fig. 42b, spectra of various samples are shown, revealing different relative intensities of the free exciton at 534 nm and the lines above 540 nm. This indicates that not only is one sample non–homogeneous, but samples synthesized through different methods may also have different defect concentrations and/or phase content. To determine whether the observed luminescence differences are caused by the presence of different phases, XRD measurements of the powdered samples were conducted, and all the results showed a pure $CsPbBr_3$ orthorhombic phase, indicating that the different defect concentrations are likely to be the real cause of the luminescence differences.

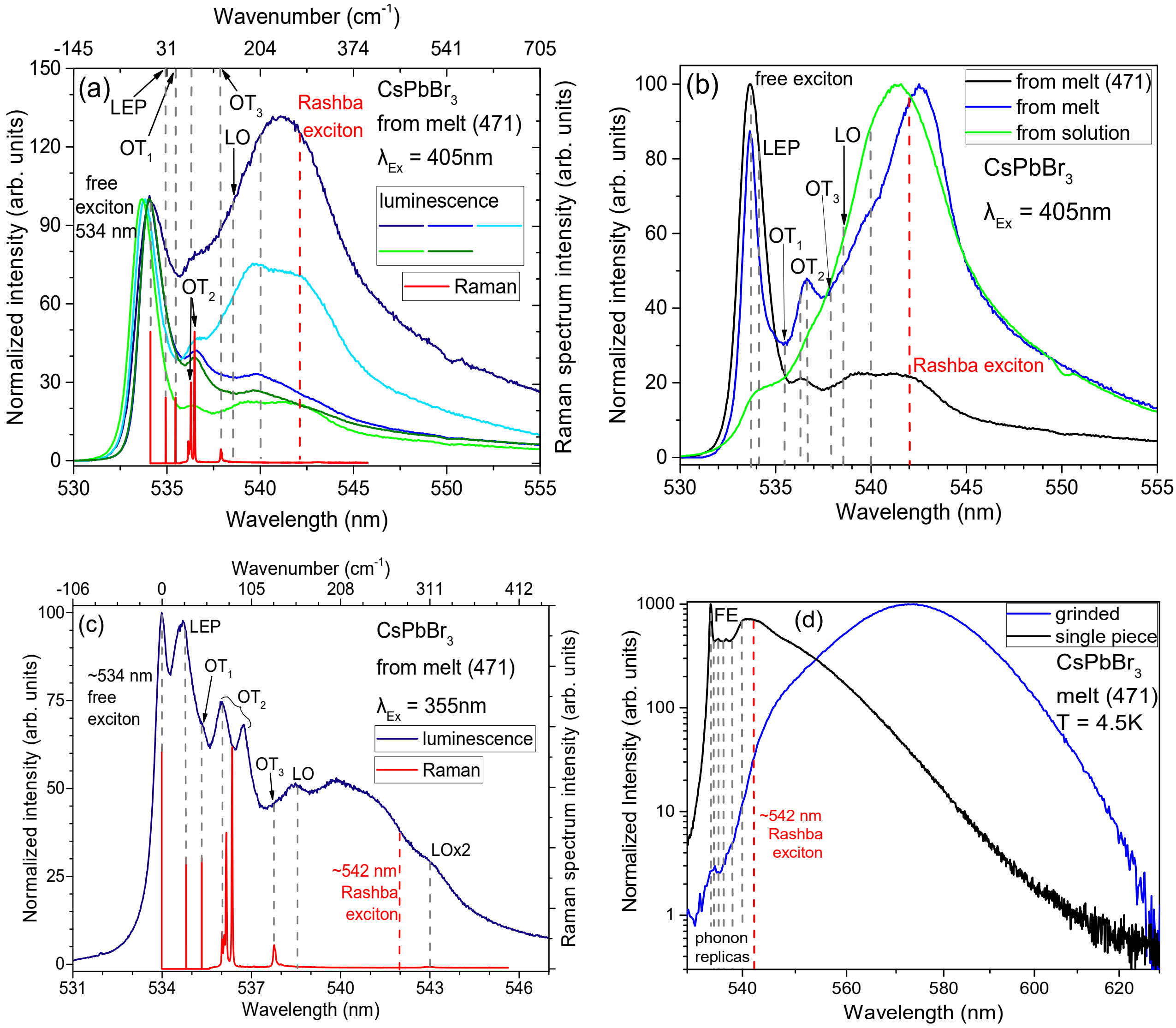

Fig. 42. Luminescence of SC CsPbBr₃ samples at liquid helium temperature. (a) – comparison of the luminescence of different parts of the sample; (b) – comparison of the samples synthesized from solution, from the melt, and old sample from melt; (c) – comparison of the CsPbBr₃ luminescence spectrum with the Raman of the same sample. (d) – luminescence of a single piece of the sample, and the powdered sample.

The highest quality sample #471 was initially measured at low temperature as a large single crystal and then ground in a mortar before being measured again in powdered form. As shown in Fig. 42d, the luminescence spectrum underwent a significant change after mechanical treatment, with the ground sample exhibiting barely detectable excitonic luminescence. $CsPbBr_3$ is a soft material [148], and mechanical treatment can result in the formation of defects in the lattice. It is also possible that different parts of the sample may contain varying amounts of defects, with those subjected to more mechanical treatment having a higher concentration. Another possible explanation for the significant change in luminescence after mechanical treatment is a change in the crystal phase of the sample. However, XRD measurements of the #471 single crystal showed the same phase as the powdered samples. Thus, we concluded that mechanical treatment did not alter the phase of $CsPbBr_3$.

VII.3.3.2. Dependence of the luminescence on temperature

The temperature dependence of the luminescence of $CsPbBr_3$ reveals interesting features. Fig. 43a shows the dependence of the luminescence as a function of temperature, while Fig. 43b shows the temperature dependence of the position of the free exciton, Rashba exciton, and defect band, as well as the integral intensity and direct band gap energy dependence on temperature.

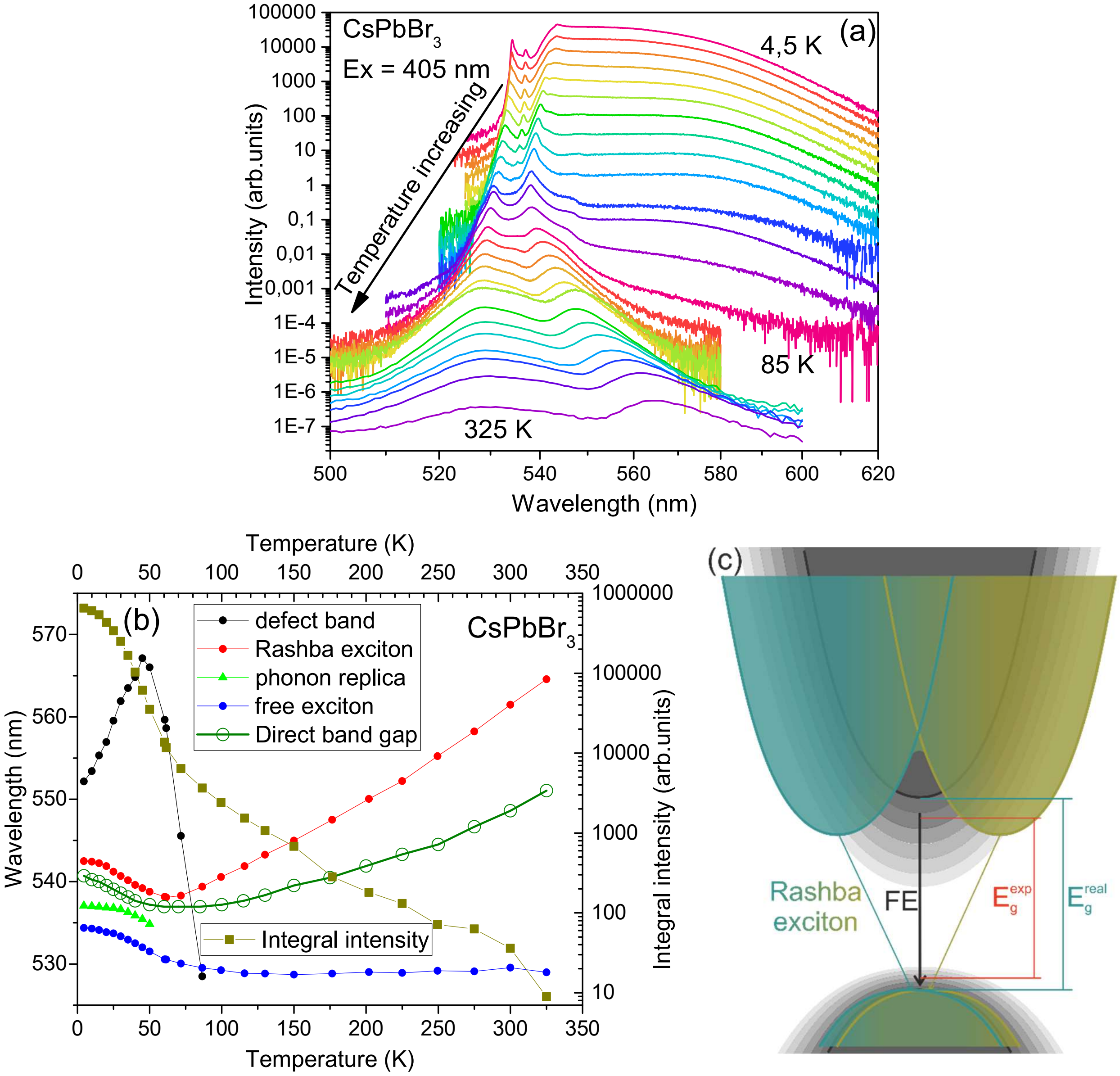

Fig. 43. $CsPbBr_3$ luminescence dependence on temperature for the sample from the melt. (a) – luminescence spectra, (b) – dependence of the luminescence integral intensity, peaks positions, and band gap energy.

One observation from Fig. 43b is that the band gap energy, calculated from the absorption spectra for the direct band gap, is located between the free and Rashba excitons. According to the definition of an exciton, the exciton energy cannot be smaller than the band gap energy. The results obtained here can be explained by the strong sub–band absorption caused by defects and structural fluctuations, which lead to an underestimation of the band gap energy. A simple visual demonstration of this explanation is shown in Fig. 43c. Due to the strong influence of sub–band absorption, the band gap calculated from the absorption spectra is underestimated, creating a false impression that the free exciton has higher energy than the band gap.

Fig. 43b illustrates a clear difference in the temperature dependence of free and Rashba excitons. This finding is consistent with previous studies [91, 93]. However, the assignment of the line at 542 nm has been debated in different studies, with some assigning it to the Rashba effect and others to defect–bound excitons. Nevertheless, recent studies have mostly agreed on the assignment of this line to the Rashba effect. Therefore, in this work, we assign the line at 542 nm to the Rashba exciton.

The intensity dependence on temperature reveals two regions. The first region, at the low temperature, shows a more rapid quenching of the integral intensity. This region ends around 80 K, and the defect luminescence is completely quenched within it. Afterward, excitonic luminescence continues to decrease more slowly. These temperature regions resemble similar ones, reported in [93].

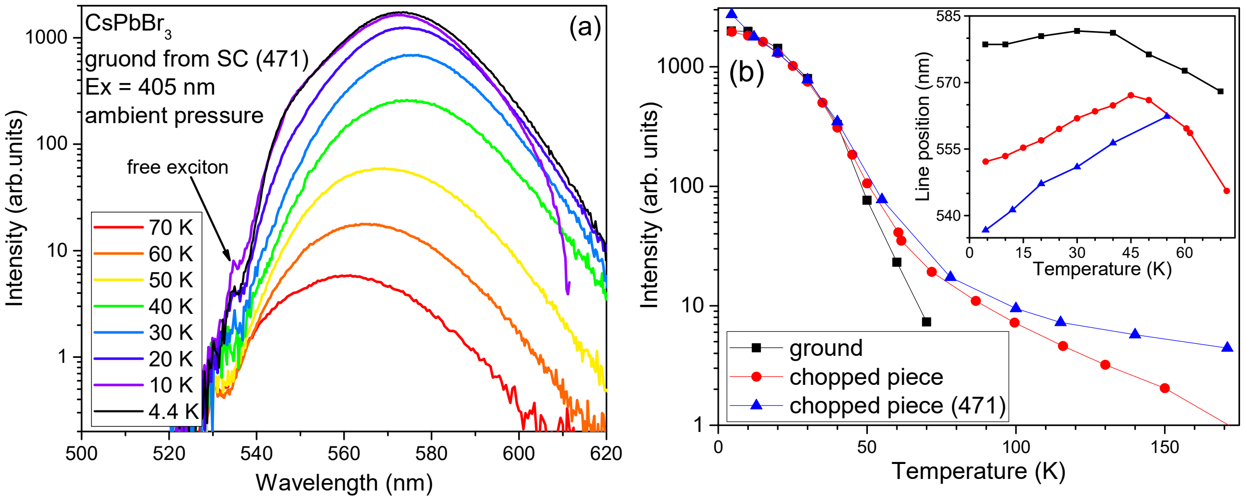

Fig. 44. Temperature dependence of the luminescence of ground sample. In (b) position of luminescence lines assigned to defects and integrated intensities of different samples are compared

The ground sample's luminescence dependence is shown in Fig. 44. The free exciton luminescence is barely detectable and only a broad band with a maximum of around 575 nm is present in the luminescence of the ground sample. In Fig. 44b, the integral intensities of entire spectra of different samples are compared. The samples are listed in decreasing order of defect concentrations: ground, chopped piece, and a single piece of sample #471. As shown in Fig. 44b, the defect luminescence is quenched at the same rate, regardless of the defect concentration within the range of our sample. At 80 K, the defect luminescence is negligibly small, and only excitonic luminescence is present at higher temperatures, which is consistent with the model of defects forming an exponential distribution of the levels below the bottom of the conduction band [99].

In the inset of Fig. 44b, the maximum position of the defect luminescence line is compared for samples with varying defect concentrations. It can be observed that the line position maximum decreases with decreasing defect concentration. At the temperature around 40–50 K, the defect luminescence changes the shifting direction, while the exciton luminescence changes the shifting direction around 80 K (as shown in Fig. 43b). This difference can be used to distinguish between excitonic and defect luminescence in $CsPbBr_3$. Similar behavior of defect luminescence is reported in [99] for $FAPbI_3$ (FA – $HC(NH_2)_2$ – formamidinium), where the authors assigned this luminescence to the defect states that form the band of levels with exponential distribution below the band gap (see details in chapter V.3.6.2, page 32). In reference [99], the authors propose that the origin of the band–tail states in $FAPbI_3$ may lie in the rotational freedom of the polar organic cation, which has been identified as a source of structural disorder in $APbX_3$. In the case of $CsPbBr_3$, the Cs ion is spherically symmetrical, and the structural disorder is related to the motion of Cs ions (see chapter IV.3.3, page 22). Therefore, the origin of the broad band luminescence of $CsPbBr_3$, shown in Fig. 43, may lie in the band–tail states, formed as a result of the structural disorder of $CsPbBr_3$.

VII.3.4. $CsPbBr_3$ luminescence under high–pressure

VII.3.4.1. Low–temperature high–pressure luminescence: spectra

Fig. 45 illustrates the luminescent spectra of $CsPbBr_3$ as a function of pressure, shown in two partially overlapping pressure ranges: (a) from 0.06 to 1.53 GPa and (b) from 0.98 to 4.22 GPa. To improve readability, the spectra are presented in two separate graphs, allowing for a clearer visualization of the transition between the first and second pressure regions.

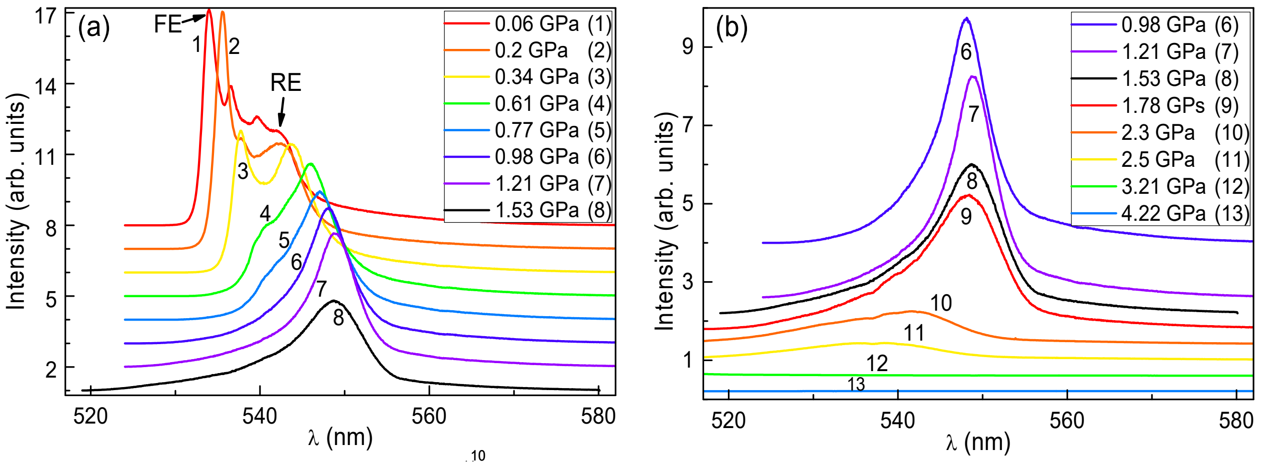

Fig. 45. Dependence of the $CsPbBr_3$ luminescence on pressure at T = 12 K. For better readability, the luminescence spectra are presented in two separate, partially overlapped pressure regions: (a) – 0.06 – 1.53 GPa and (b) – 0.98 – 4.42 GPa.

The luminescence peaks in Fig. 45 can be divided into two groups, corresponding to direct (free) and indirect (Rashba) excitons. The intensity of the free exciton (534.0 nm) and its phonon replica decreases as pressure increases, while the intensity of the Rashba exciton (542 nm) increases. At a pressure of 1 GPa, the free exciton and its phonon replica are almost entirely quenched, forming a structureless shoulder to the Rashba line. Conversely, the intensity of the Rashba exciton begins to decrease significantly above 1.3 GPa and disappears completely at 4.2 GPa.

VII.3.4.2. Position of the low–temperature high–pressure luminescence

Fig. 46 shows the energy position of the luminescence maxima of free and Rashba excitons as a function of pressure. A shift towards lower energies (in the long–wavelength direction) is observed in the pressure range of 0–1.3 GPa, followed by a reverse shift towards higher energies after 1.3 GPa. The shifts in the two mentioned above regions can be fitted by the equation from [149]:

$$E_g = E_{opt} + \chi \mathrm{p} \tag{20}$$

where E_{opt} is the ambient optical gap and χ is the pressure coefficient, indicating the change of the band gap (in meV) with a change of 1 GPa in hydrostatic pressure. The fitting by equation (20) is shown in Fig. 46, yielding values of $\chi = –41$ meV/GPa and $\chi = –28$ meV/GPa for the free and Rashba excitons, respectively, in the pressure range of 0–1.3 GPa, and $\chi = 59$ meV/GPa and $\chi = 89$ meV/GPa for the free and Rashba excitons, respectively, for pressures above 1.3 GPa. These values are consistent with previous studies of $CsPbBr_3$ at room temperature [50, 51, 100, 150, 151].

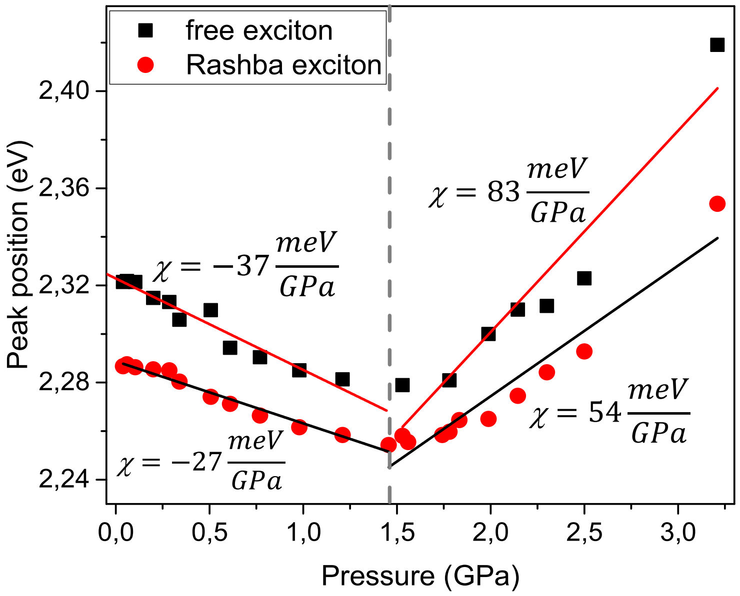

Fig. 46. Dependence of the position of $CsPbBr_3$ luminescence maxima on pressure at T = 12 K.

In a study [64], the bottom of the conduction band is found to be determined by the non–bonding localized state of the *6p* orbital, and therefore, the effect of pressure is not significant for its energy position. The width of the band gap is mainly determined by the energy states of the valence band, which has an antibonding character resulting from the interaction of the *6s* Pb and *4p* Br atomic orbitals with the predominant contribution of the *4p* Br orbitals [152]. The decrease in the overlap of the wave functions in the valence band leads to a strengthening of the bond and a shift of the top of the valence band toward lower energies, resulting in an increase in the band gap [150]. This occurs until the distance between bromine and lead reaches critical values, beyond which this approach is no longer appropriate.

As discussed in chapter V.3.1.2, page 20, two main changes occur in the structural parameters of $CsPbBr_3$ with pressure increase, which are Pb–Br distance reduction and Pb–Br–Pb angle reduction. Moreover, below ~1.3 GPa Pb–Br distances are more easily compressed than above this critical pressure, which results in the isostructural phase transition around 1.3 GPa and different behavior of the band gap below and above the phase–transition pressure. In work [150], authors show theoretical calculations for high pressures, concluding that the changes in the Pb–Br–Pb angles are decisive for the change of the band gap above 1.3 GPa. Calculations show that with pressure increase from 1.3 to 4.2 GPa, the angle changes from 153° to 133° [64], which is sufficient to increase the Pb–Br distance. This increase in the $CsPbBr_3$ band gap is caused by the octahedron rotations and is consistent with the behavior of the position of the luminescence maxima as a function of pressure, which is clearly seen in Fig. 46.

VII.3.4.3. The intensity of the low–temperature high–pressure luminescence

The integrated intensity of the $CsPbBr_3$ luminescence was determined by calculating the area under the luminescence curves. The dependence of the integrated intensity on pressure is shown in Fig. 47a, where the black squares and black eye–guiding line represent the total luminescence intensity. The intensity of the Rashba emission was estimated by measuring the peak maxima from Fig. 45 for all spectra and is shown in Fig. 47a as red circles and a red eye–guiding line. The intensity of the free exciton was obtained by subtracting the Rashba intensity from the total luminescence intensity and is also shown in Fig. 47a as blue triangles and a blue eye–guiding line. It should be noted that the estimation of the free exciton's intensity includes the intensity of the phonon replicas of the free exciton, which leads to a slightly higher value for the free exciton's intensity.

The data presented in Fig. 47a demonstrate that the luminescence of free exciton and its phonon replicas decreases in intensity with increasing pressure up to 1 GPa, while the luminescence of Rashba exciton becomes more intense in this pressure range. However, at higher pressures, the Rashba exciton is also quenched. These observations suggest that free excitons and Rashba excitons compete as de–excitation channels for excited electron–hole pairs generated during the excitation process (see Fig. 47b).

From Fig. 46, it can be observed that the energetic distance between free and Rashba excitons is not constant with pressure. It decreases and then increases respectively below and above 1.3 GPa. This suggests that the Rashba splitting decreases and then increases below and above 1.3 GPa. In [153], the authors report that the Rashba splitting decreases with increasing pressure for $MAPbI_3$, which supports our assumption.

At ambient pressure, the energy difference between the free excitons and Rashba excitons is about 35 meV (about 350 cm^{-1}), which is in agreement with [93], and decreases with applied pressure to about 25 meV (202 cm^{-1}) at the pressure of about 1 GPa (see Fig. 46). The decrease of the free exciton’s intensity and increase of the Rashba exciton’s intensity with pressure increase can be explained by the increase of the probability of nonradiative deexcitation from the free exciton to the Rashba exciton (schematically shown in Fig. 47b). This process can be explained by the so–called "energy–gap law" [154]. According to that law, the multiphonon emission rate A_{nr} between two states separated by the energy ΔE is proportional to the exponent of the energy ΔE:

$$A_{nr} = A_{nr}(0)e^{-\alpha\Delta E} \tag{21}$$

Here $A_{nr}(0)$ and α are characteristic parameters for the material. The energy gap ΔE may be expressed as:

$$\Delta E = n \cdot \hbar\Omega \tag{22}$$

Here $\hbar\Omega$ is the effective phonon energy and n is the number of phonons needed to cover the energy distance ΔE. Considering the above values of energy distances between the free exciton's and Rashba exciton's states at ambient pressure and about 1 GPa, and the LO phonon energy of $CsPbBr_3$ (19 meV = 155 cm^{-1} [42, 77]), we get the ratio of nonradiative transition rate between these levels at ambient pressure and 1 GPa equal approximately to at least $e^{-1\beta}/e^{-2\beta} = e^{1} \approx 2{,}72$ times, where $\beta = \alpha\,\hbar\Omega$. This means that the probability of nonradiative deexcitation between the free exciton and Rashba exciton increases approximately 2.7 times between ambient and 1 GPa pressures. This mechanism is analogous to the one the authors of [93] used to explain a similar effect they observed in the temperature–dependent luminescence of $CsPbBr_3$.

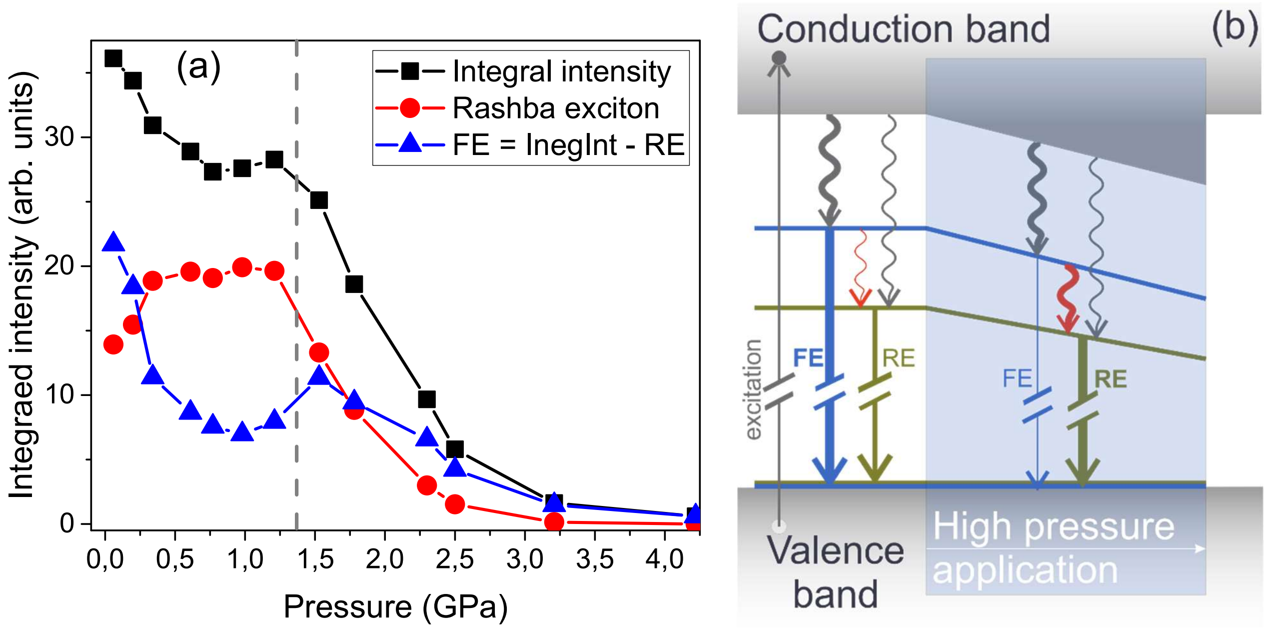

Fig. 47. (a) Pressure dependence of the integral intensity of $CsPbBr_3$ luminescence, and pressure dependence of the in–peak intensity of the Rashba excitons emission. (b) Schematic representation of the position of free and Rashba excitons on pressure.

This is why excitation energy is efficiently transferred to the Rashba excitons, leading to the quenching of free exciton emission with increasing pressure. The effective phonon energy of $CsPbBr_3$ may be lower than 155 cm^{-1} due to the presence of low–energy TO phonons with an energy of approximately 75 cm^{-1} (as reported in chapter VII.3.2, page 76 and in works [74, 75]). These phonons could also participate in the transitions between free and Rashba excitons, which would increase the nonradiative transition probability.

As discussed earlier, the intensity of Rashba excitons increases below 1.3 GPa due to the increase in the probability of nonradiative deexcitation from free excitons to Rashba excitons. Therefore, the slight increase in free exciton intensity in the pressure range 1.0–1.5 GPa can be explained by the decrease in the probability of nonradiative deexcitation caused by the increase in the Rashba splitting above 1.3 GPa.

The Rashba excitons have the lowest intensity relative to free excitons at 1 GPa, while the smallest Rashba splitting occurs at 1.3 GPa, which are slightly different pressures. We believe that this discrepancy is due to the low accuracy of the fittings done in Fig. 46. As shown in the figure, the position dependencies of luminescence peaks on pressure are not linear but rather follow parabolic–like curves. Fittings with straight lines were done because they have a physical basis, whereas fitting with parabolas does not. A parabolic–like dependence of the $CsPbBr_3$ luminescence position on pressure is reported in many other works [49, 63, 146, 148].

VII.3.4.4. Blue luminescence at pressures above 2 GPa

The luminescence of $CsPbBr_3$ with the lowest concentration of defects (sample #471) was measured at low temperatures as a function of pressure. The results of measurements of one piece of the sample are presented in Fig. 45, which are repeated in Fig. 48a. Results from another measurement of a different piece of the same sample are shown in Fig. 48b. As can be seen from Fig. 48, the general behavior of the luminescence under pressure is very similar for both cases. The difference comes from the relative intensity of the lines at the lowest pressure.

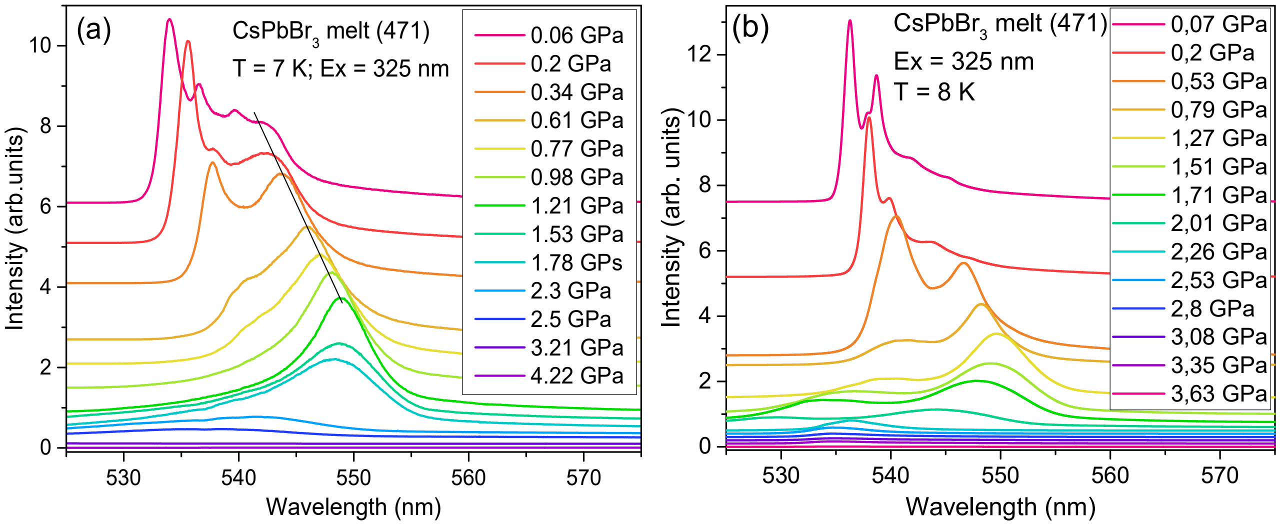

Fig. 48. Low–temperature luminescence of $CsPbBr_3$ as a function of high pressure. (a) and (b) are two measurements of different pieces of the same sample (from the melt, number 471). Oil was used as a pressure–transmitting medium

Fig. 49 shows the luminescence spectra from Fig. 48b in a broader spectral range with a logarithmic scale on the Y–axis. This allows us to demonstrate the weak blue luminescence that starts appearing around 500 nm as a single band at pressure 1.27 GPa (see Fig. 49a). As the pressure increases up to 2 GPa, this luminescence increases in intensity, and additional lines at approximately 475, 450, 425, and 400 nm appear (see Fig. 49b and c). At the pressure range from 2 GPa to 3.35 GPa, the intensity of the blue luminescence remains approximately the same and only redistributes between different lines. At the same pressure range, the intensity of the green luminescence continues to decrease. Fig. 49d shows the spectrum at 3.63 GPa, where the regular green luminescence of $CsPbBr_3$ is already very weak, and the blue luminescence intensity is also decreasing at high pressures. Around 4 GPa, all luminescence disappears.

In [51], the authors measured the absorption spectra of $CsPbBr_3$ as a function of pressure. The results show that the band gap of $CsPbBr_3$ decreases slightly as pressure increases up to 1 GPa. Afterward, the band gap increases up to 2 GPa. Around 2 GPa, the band gap of $CsPbBr_3$ jumps into the blue region of the spectra [51, 100]. Therefore, the blue luminescence shown in Fig. 49 may originate from newly formed excitons and/or defects, which appear in the abruptly expanded band gap.

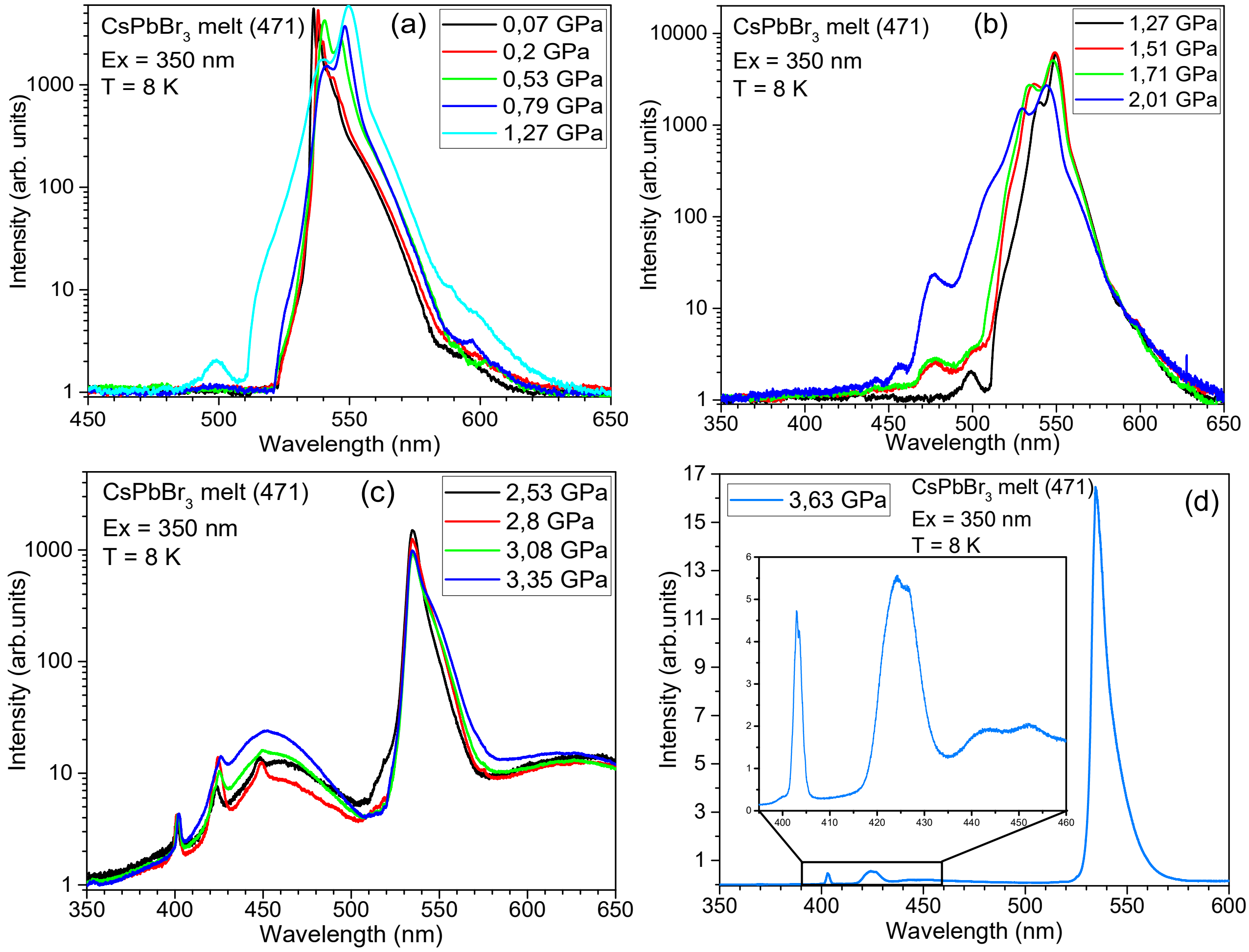

Fig. 49. Low–temperature blue luminescence of $CsPbBr_3$ under high pressure. Spectra are shown in logarithmic scale, to show details of the weak luminescence, and how it appears. Argon was used as a pressure–transmitting medium

In Fig. 50, the high–pressure blue luminescence of $CsPbBr_3$ at room temperature is shown. The intensity of the blue luminescence is much higher at room temperature compared to low temperature (as seen in Fig. 50) and can be attributed to the stronger temperature quenching of the green luminescence. The spectra of the blue luminescence measured at room temperature are similar to the spectra of $CsPbBr_3$ nanoparticles reported in previous works (such as [155, 156, 157]).

Amorphization processes under high pressure have been reported in some works (see details in chapter V.3.1.2, page 20). The high–pressure blue luminescence of $CsPbBr_3$ is similar to the luminescence of nano–sized $CsPbBr_3$, and the formation of nano–sized grains under high pressure could be proposed, considering amorphization. However, this assumption has several major drawbacks: (i) amorphization is almost impossible to reverse, (ii) there is no experimental confirmation of such a process yet, and (iii) some works report no amorphization at high pressure, but a phase transition (see details in chapter V.3.1.2, page 20). Therefore, the best explanation for the origin of the blue luminescence is the fast broadening of the band gap at high pressures. The effect of band–gap broadening as a function of pressure requires theoretical support, which is beyond the scope of this research, and may be an interesting topic for theorists.

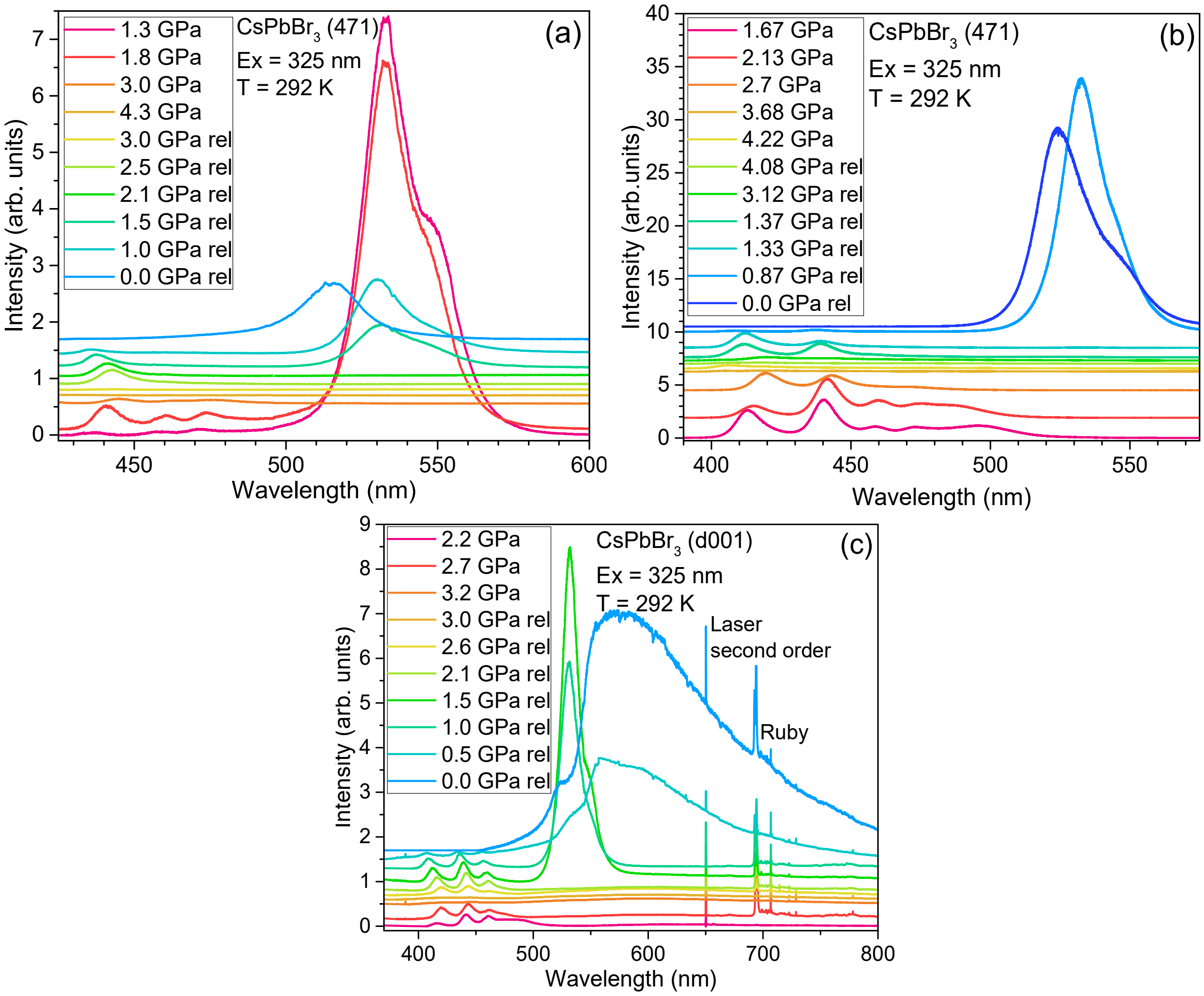

Fig. 50. High–pressure measurements of $CsPbBr_3$ blue luminescence at room temperature. All measurements were taken in both directions: while the pressure was increased, and while it was released. For the points, when the pressure was released, marked as "rel" in the signature. Argon was used as a pressure–transmitting medium

As shown in Fig. 50, the blue luminescence does not depend on the defect concentration in the sample. The blue luminescence appeared in both highly defected (numbered d001) and low defect #471 samples, suggesting that the blue luminescence is a fundamental property of the crystal rather than a result of defects present in the lattice.

VII.3.5. Dependence of the luminescence on the power density of the excitation light

VII.3.5.1. At low temperature

The spectra shown in Fig. 42a were excited with the same laser and power density of the laser light, allowing for a correct comparison. However, the spectra in Fig. 43a and Fig. 43c were measured with different power densities of the excitation light, and thus cannot be compared as there is a strong dependence of luminescence on the power density of the excitation light. To study this dependence, a few samples were measured at 8 K as a function of the power density of the excitation light. The results are presented in Fig. 51, where the spectra are normalized to the intensity of the free exciton line (around 534 nm).

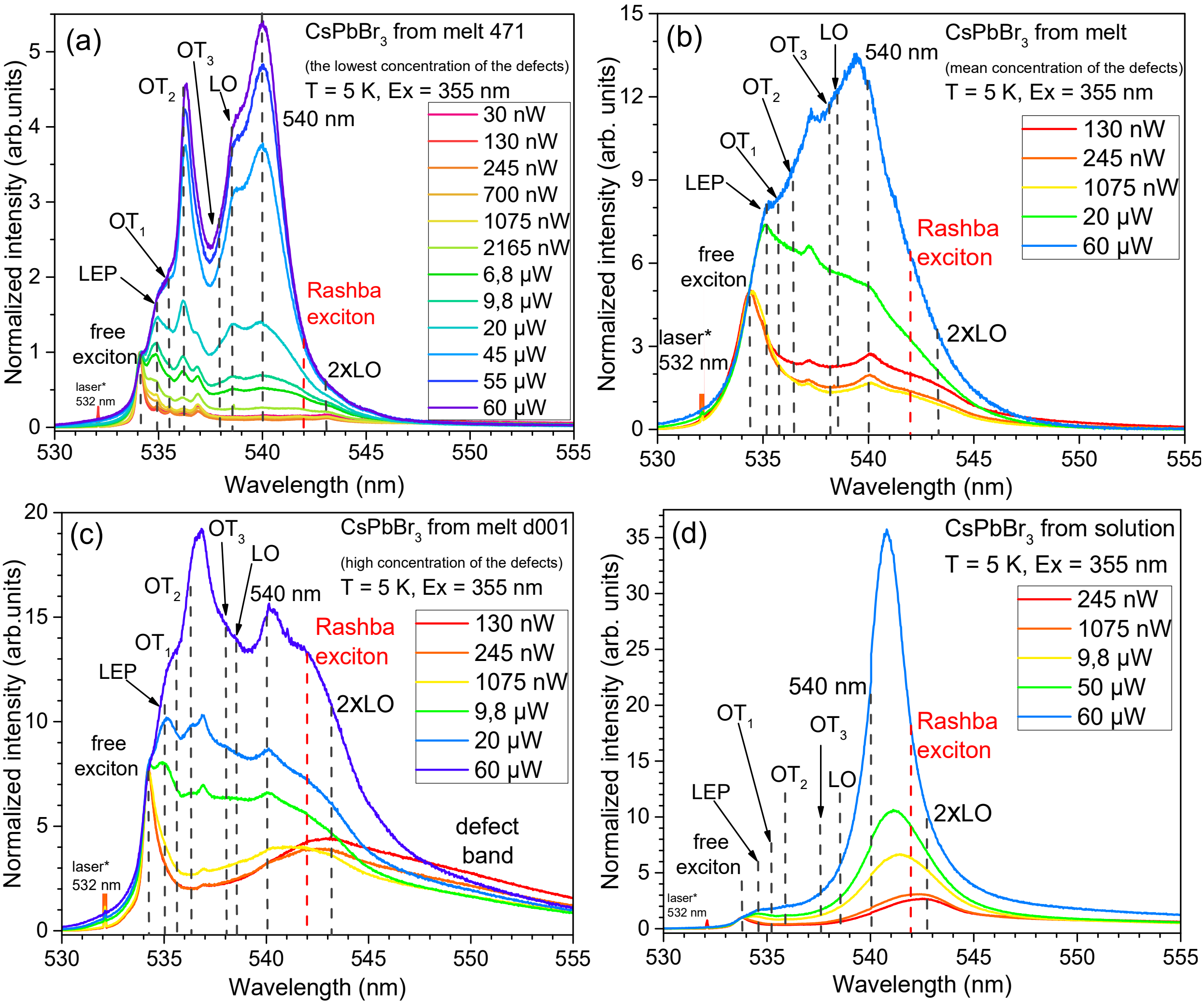

Fig. 51. Dependence of CsPbBr3 luminescence on the power density of the excitation light. Measured under excitation of 355 nm pulsed laser. A set of density filters was used to reduce full laser power to some value

As shown in Fig. 51, the relative intensities of the phonon replicas increase with increasing power density. However, there are additional lines at around 536.8, 538.6, and 540 nm, the origin of which is unknown. The relative intensity of these lines increases with the power density of the excitation increase.

In the work [144], the reversible phase transition of $CsPbBr_3$ caused by light exposure was investigated using XRD and Raman techniques. This phase transition is from the orthorhombic (Pnma) to the tetragonal ($P4_2mc$) structure, which returns to normal once the light is switched off. Assuming that the same phase transition occurs at low temperatures, the dominance of free exciton (534 nm) luminescence for the low power density of the excitation light indicates the orthorhombic structure. Meanwhile, the 540 nm luminescence prevails for the high density of the excitation power, indicating the free exciton of the tetragonal phase. The coexistence of both phases explains the presence of both excitonic lines simultaneously.

A possible alternative explanation for the emission around 540 nm is that it may be assigned to the bi–exciton. In a previous study [32], the authors claimed to have found bi–excitons in $CsPbBr_3$. While there are many studies on the topic of bi–excitonic luminescence in $CsPbBr_3$, most of them are based on decay kinetic measurements, which provide the authors with a sufficient basis for assigning the lines to bi–excitons. Therefore, without further study, it is difficult to definitively assign the 540 nm line to a bi–excitonic origin based solely on the results presented in this work.

It is important to consider the heating of the sample as a potential source of the observed changes due to light exposure. However, a previous study [144] excluded the possibility of sample heating by monitoring the temperature change during the light exposure and showing a negligible temperature change. As discussed earlier (see Fig. 43), an increase in temperature up to 80 K results in luminescence lines shifting towards higher energies. However, in the case of power–density–dependent spectra, as the power density of the light source increases, the lines do not shift or shift in the opposite direction. Therefore, the heating of the sample is considered to be negligible.

In the spectra of the $CsPbBr_3$ sample from the melt with the label d001 (see Fig. 51c), a broad band around 550 nm is observed and is attributed to defects. It is noticeable that the relative intensity of this band decreases as the excitation power density increases, which is the expected behavior for defect luminescence. As the power density of the excitation increases, a saturation of the defect luminescence is expected to occur at some point. The sequential increase in excitation power should only cause an increase in the excitonic luminescence, which is consistent with additional measurements of the sample from the melt with the lowest defect content after mechanical treatment (see Fig. 52a). The sample was ground and then measured as a function of power density at liquid helium temperature. Similar observations for $CsPbBr_3$ were made by other authors in [33], and the broadband emission around 550 nm (Fig. 51) and 575 nm (Fig. 52) showed power and temperature dependence identical to the dependences in [33]. This supports the assumption that the defect band originates from the defect band with an exponential distribution below the band gap.

To compare the different samples, their spectra were excited with the same power density, and their luminescence spectra were plotted on one plot. Fig. 52b shows the luminescence spectra of different $CsPbBr_3$ samples excited with a laser power of 60 μW, while Fig. 52c shows the spectra excited with a power of 0.245 μW. The highest intensity of the defect luminescence is observed for the ground sample in both cases, but even for this sample, the excitonic luminescence dominates when excited with a laser power of 60 μW. The luminescence around 540 nm is dominant for all samples when excited with 60 μW of laser power.

The maximum of the defect luminescence also depends on the power density of the excitation light. As shown in Fig. 52a, as the excitation power increases, the defect luminescence shifts towards higher energies. This is in agreement with the saturation model mentioned earlier.

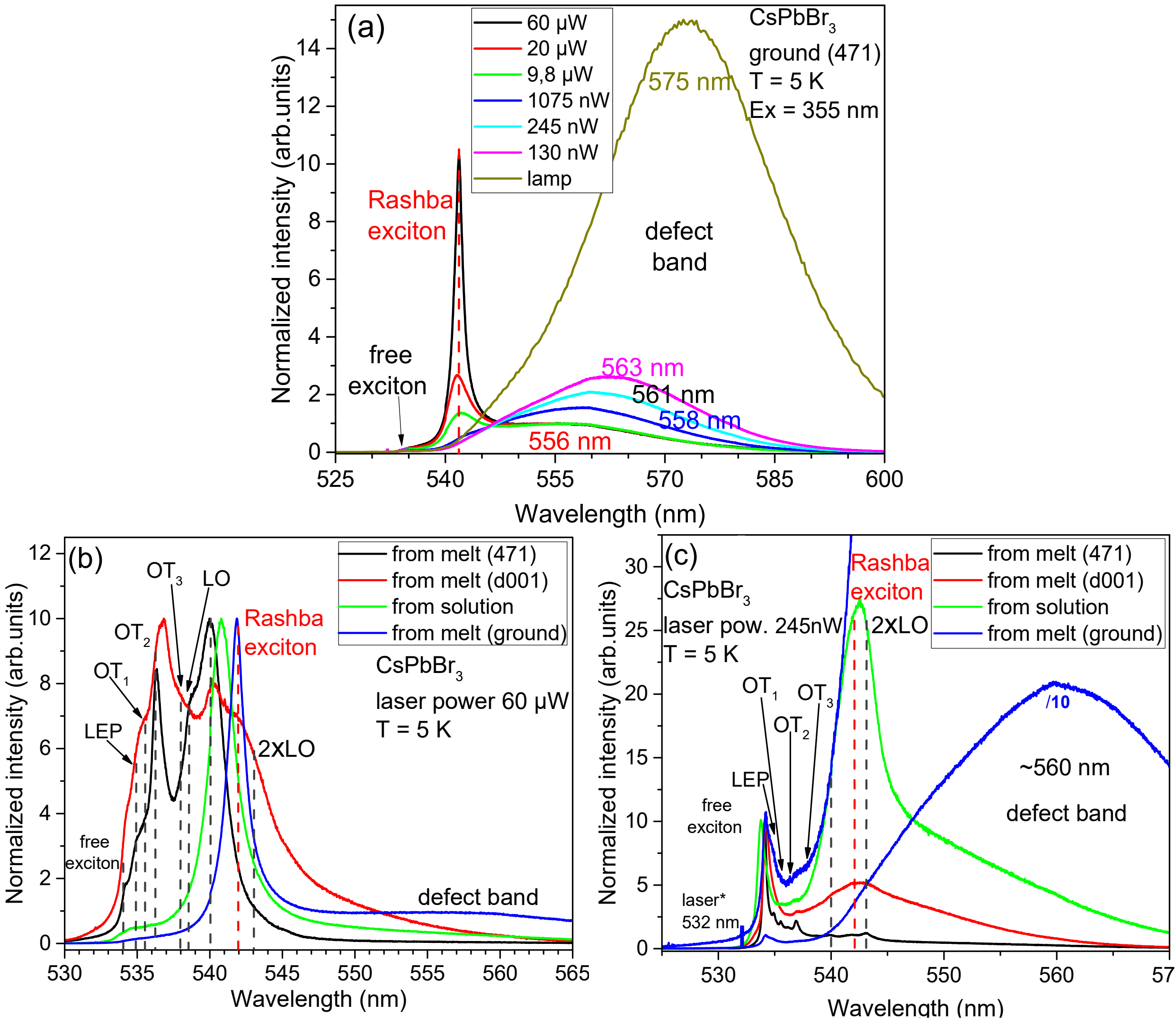

Fig. 52. Luminescence as a function of the power density of the excitation light of ground sample (a); comparison of different samples luminescence at constant excitation density power: (b) – 60 μW and (c) – 0,245 μW of the laser power

Another possible explanation for the observed spectra changes in Fig. 51 is that the lines at 534, 534.9, 535.5, 536.2, 536.9, 538.6, and 540 nm may originate from different excitonic pairs of the monophase $CsPbBr_3$. The change in the relative intensity of these lines could be caused by the redistribution of electrons on the excitonic level under the influence of the high density of the excitation power.

VII.3.5.2. Luminescence as a function of temperature and power density

To gain a better understanding of the spectra shown in Fig. 51 and Fig. 52, the temperature dependence of CsPbBr$_3$ luminescence was measured at a constant density of excitation power. Results for single crystal and ground samples are presented in Fig. 53 and Fig. 54, respectively.

Fig. 53 shows that luminescence around 540 nm is present for all densities of excitation power. The exact origin of this line was not determined in the previous chapter. Assuming it is a bi–exciton line, it should not be present at the lowest excitation power (Fig. 53d) and should decrease more rapidly with temperature increase than it does in Fig. 53a, b, and c. Therefore, it is not a bi–exciton. Assuming it is the Rashba line, its intensity relative to free exciton intensity should decrease with increasing excitation power. Therefore, it is not a Rhashba exciton, and the origin of it still remains unclear.

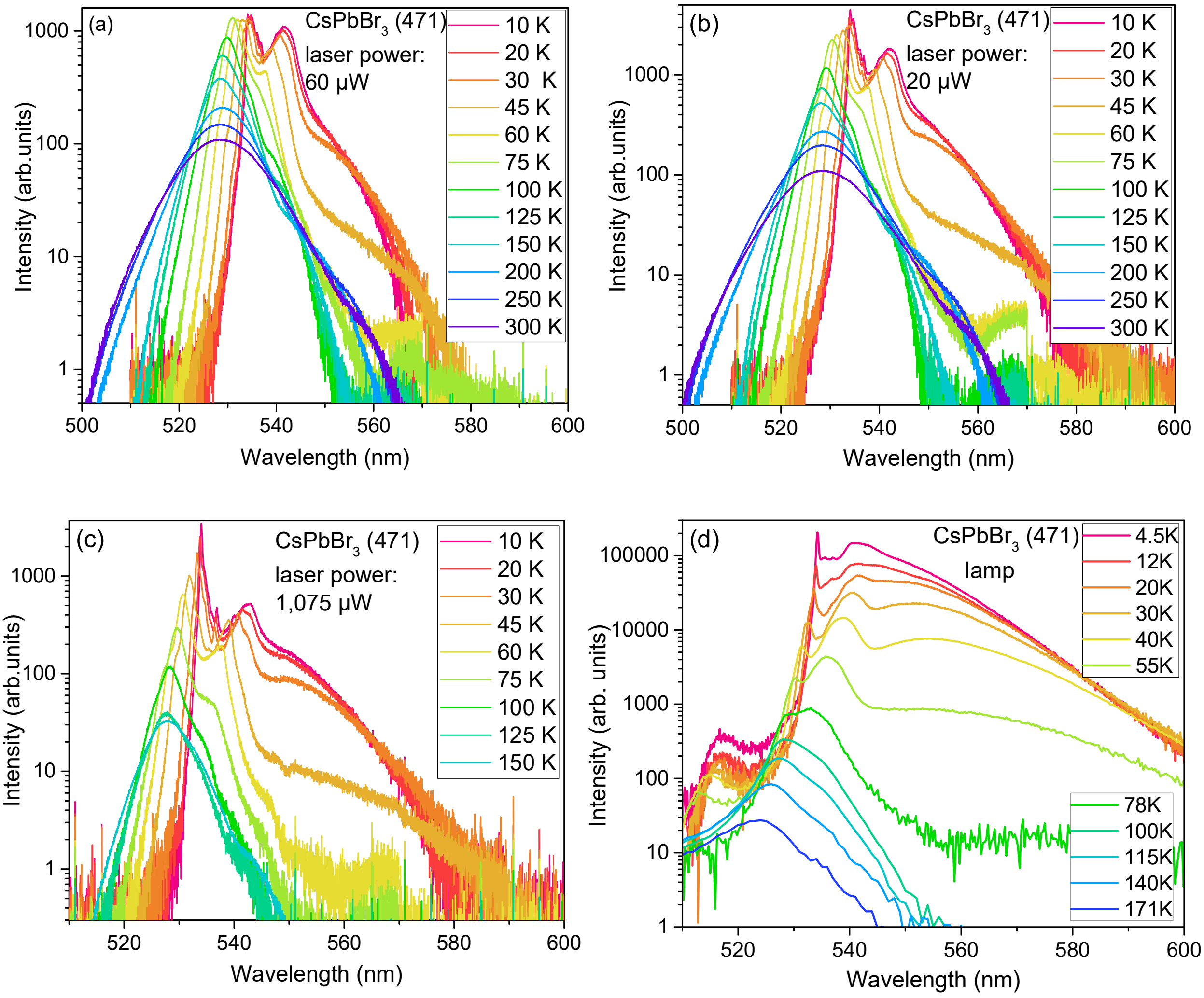

Fig. 53. Temperature–dependent spectra of CsPbBr$_3$ single crystal at different excitation power: (a) – 60 μW; (b) – 20 μW; (c) – 1.075 μW; (d) – lamp

Fig. 54 presents temperature–dependent spectra of the ground sample at different excitation power densities. As shown, the defect band of the ground sample prevails at low temperatures. As temperature and/or excitation power increase, the intensity of the defect band decreases, and the 540 nm line intensity increases.

It appears that the 540 nm line and defect band are related, and the population can redistribute between them. Therefore, it can be assumed that they originate from two closely positioned centers or even the same center. In this case, the 540 nm line should be some kind of very fast transition from the top of the defect levels, assuming, that the defects are forming some distributions of states. However, as shown in Fig. 51d, the 540 nm line can exist without the defect band. Further study is required to better understand the origin of these lines.

As shown in Fig. 51, Fig. 53, and Fig. 54, the free exciton line around 534 nm is dominant for single crystal samples with low defect concentration. If the concentration of defects increases in the sample, the defect band and 540 nm line appear. However, the 540 nm line can also be dominant in the sample due to another reason. For example, it is dominant in the sample synthesized from the solution (see Fig. 51d).

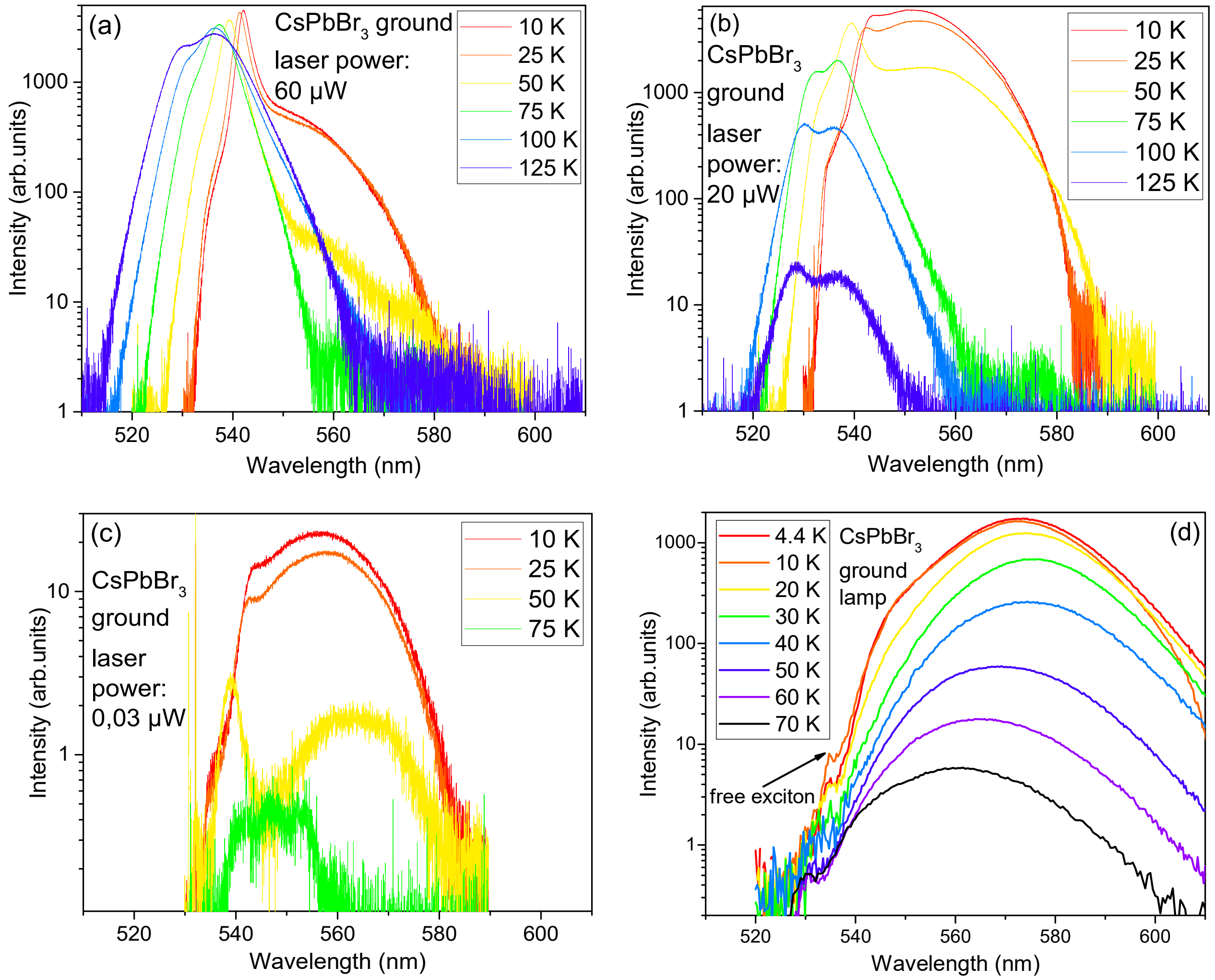

Fig. 54. Temperature–dependent spectra of ground $CsPbBr_3$ at different excitation power: (a) – 60 µW; (b) – 20 µW; (c) – 0.03 µW; (d) – lamp

Another possible origin of the 540 nm line is the presence of a secondary phase, such as tetragonal. This is likely to be the most plausible explanation. In this case, samples synthesized from the melt usually have an orthorhombic structure and exhibit free exciton emission with their phonon replicas and Rashba exciton. The sample synthesized from the solution might have a high amount of the secondary phase, which gives rise to a 540 nm line (probably free exciton too but without phonon replicas). At high excitation power, the 540 nm line is dominant due to reversible phase transition, reported before under light exposure [144]. As shown in Fig. 54, with increasing temperature, free exciton luminescence starts to prevail over the 540 nm line. This could be explained by the higher stability of the secondary phase at low temperatures, with an increase in temperature causing the increase of the volume of the regular orthorhombic phase.

VII.4. Comparison of calculated from experimental results parameters

The intensity of the central peak from Raman spectra was calculated to represent the number of structural fluctuations. The dependence of the central peak intensity on temperature is plotted alongside the Urbach energy (see details in chapter VII.3.1, page 18) in Fig. 55. As seen in the figure, there is a correlation between the intensity of the central peak and the Urbach energy, suggesting that the additional absorption below the band gap (Urbach absorption) is related to structural fluctuations. In other words, the structural fluctuations locally create lowered band gaps that form an exponential distribution of levels below the undistorted band gap.

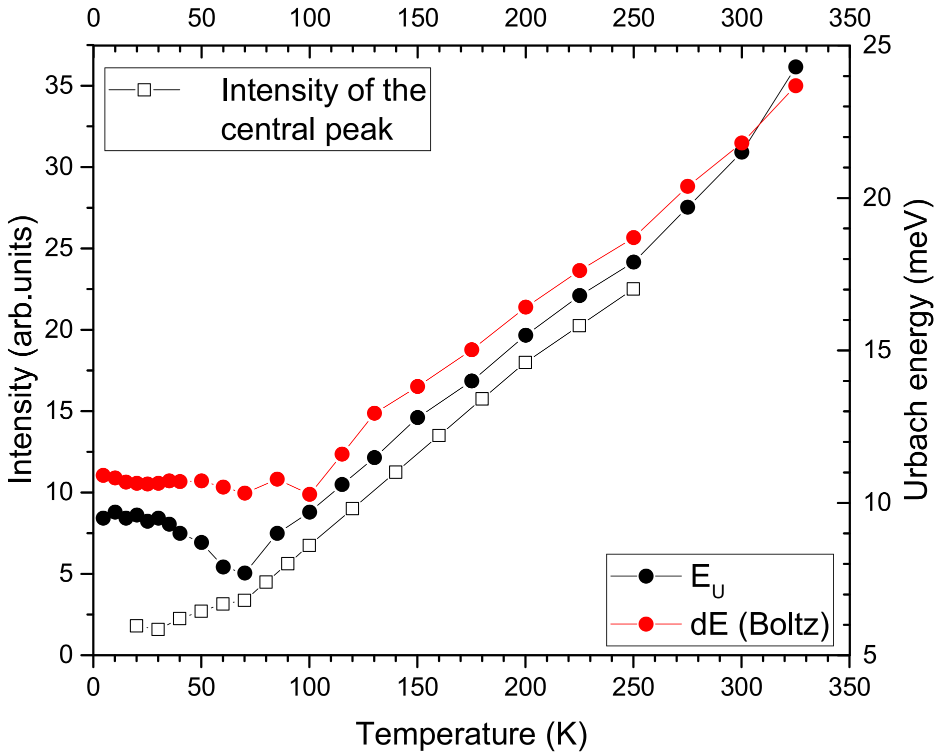

Fig. 55. Comparison of the intensity of the central peak with the Urbach energy (estimated in chapter VII.3.1.2, page 74)

It is important to emphasize that the distribution of the Urbach states and the distribution of the defect levels (see Fig. 10) are completely different sets of states. The Urbach states are formed by the rapidly fluctuating band gap, while the defect states are stable and formed by some defects, such as Br–vacancies. The decay time of the defect luminescence is known to be in the range of microseconds [42], which is impossible from fast fluctuating states. Despite the different origins of these states, their energy dependence on temperature is correlated. This correlation is evident in Fig. 56b, where the intensity of the central peak starts to increase faster around 80 K, while at lower temperatures, the defect luminescence is quenched. This behavior can be explained by the depopulation of the defect states through structure fluctuations. At low temperatures, the structure fluctuation is mainly formed by the quantum zero–point motion and does not significantly contribute to the depopulation of the defect levels. As the temperature rises, the structure fluctuation increases, and this starts depopulating the defect band.

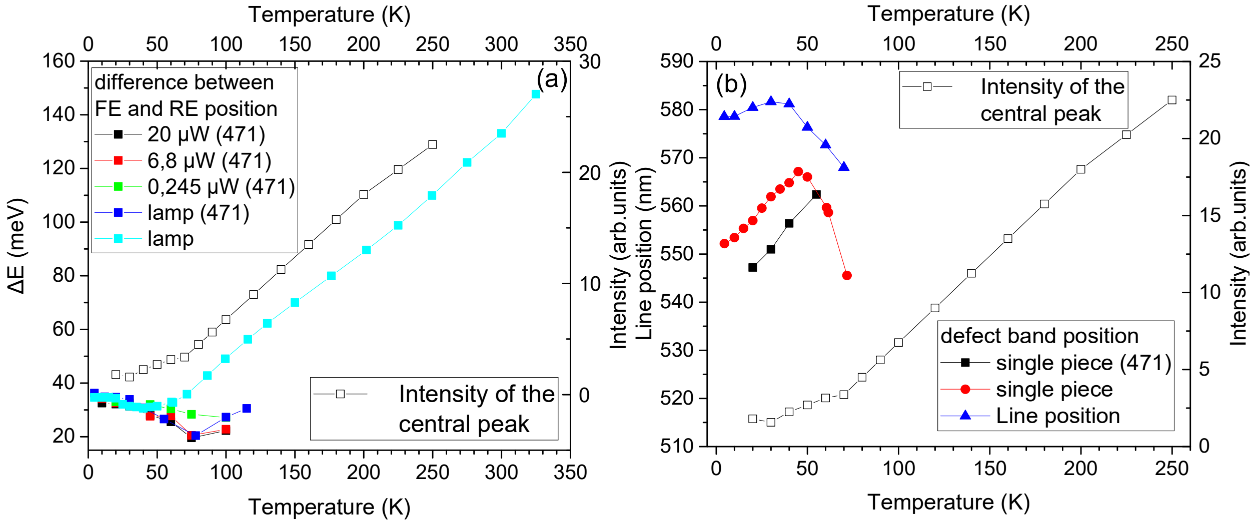

Fig. 56. Shows the correlation between the intensity of the central peak and: (a) the energetic distance between free and Rashba exciton; (b) the position of the defect band

As seen in Fig. 56a, the energetic distance between the free and Rashba exciton is proportional to the intensity of the central peak. This suggests that the electric field responsible for the Rashba effect is proportional to the structural fluctuation, and therefore, the lowering of the Rashba minimum is also proportional to the structural fluctuation.

VIII. Conclusions

VIII.1. Rare–earth aluminum oxide perovskites

VIII.1.1. Doped with Eu^{3+}

In this work, SCFs of *R*AP (*R* = Gd, Tb, Y, Lu) doped with Eu^{3+} and grown by the LPE method were studied. The luminescence properties were investigated using high–pressure spectroscopy, with a particular focus on the sharp Eu^{3+} lines in the luminescent spectra. It was observed that the structure of these lines is identical for *R*AP (*R* = Gd, Tb, Lu) perovskites. However, YAP had a much richer line structure, possibly due to the existence of a larger variety of Eu^{3+} sites with different local symmetry.

In line with the typical behavior of Eu^{3+}, the luminescent lines of the samples shifted towards lower energies as the pressure increased. However, in the case of YAP, some lines showed a different trend, shifting towards higher energy with increasing pressure. The K–value, which is the ratio of the intensities of $^5D_0 \rightarrow {}^7F_2$ and $^5D_0 \rightarrow {}^7F_1$ transitions of the Eu^{3+} ion, for YAP was less different from the general trend than LuAP's K–value. The K–value decreased with increasing pressure in all samples. The K–value for YAP was approximately 0.7 at the lowest pressure, which is consistent with [9], while the K–value of the other samples was close to 1.8 at the lowest pressure.

In the case of LuAP, the behavior of the K–value on pressure was found to be different due to the interaction of Eu^{3+} centers with defects. These defects revealed themselves in the form of broadband under 325 nm and 275 nm excitation, with their origin assigned to Pb^{2+} dimers in LuAP:Eu SCF, as well as to the centers created by the charged dimers of the oxygen vacancies. With increasing pressure, the defect luminescence shifted towards higher energies, with its intensity initially increasing, reaching its maximum slightly below 20 GPa, and decreasing afterward. The pressure dependence of the K–value of LuAP strongly correlated with the defect luminescence intensity on pressure, supporting the assumption of the interaction between Eu^{3+} and defect centers.

LuAP SCF was found to have the highest amount of defects compared to the other samples, which may be related to the smallest ionic radii of Lu ion compared to the other rare earth elements, leading to the biggest lattice parameters mismatch of YAP and LuAP. Additionally, the LuAP SCF was grown on a YAP substrate, creating favorable conditions for defect formation in the SCF.

Thus, it was concluded that the K–value parameter depends on (i) the lattice parameters of the examined perovskites, (ii) the symmetry of the local structure, (iii) the concentration of defects, and (iv) the strength of the interaction between defects and Eu^{3+} centers. Consequently, the K–value is not only dependent on the chemical compound but also on the presence of defects, which in turn depend on the growth conditions and the concentration of non–intentional dopants.

VIII.1.2. Doped with Ce^{3+}

The absorption measurements in the near–UV region of YAP and LuAP crystals led to the determination of the bandgap values of $YAlO_3$ and $LuAlO_3$ single crystals at room temperature. The direct bandgap values were found to be 7.63 eV and 7.86 eV, respectively. At high temperatures above 650 K, thermal quenching of YAP:Ce luminescence was observed, which provided valuable information about the position of the lowest excited *5d* level of Ce^{3+} relative to the bottom of the conduction band. The position of the *4f* level was estimated to be consistent with the predictions of Dorenbos theory and DFT calculations.

In LuAP crystals, Ce^{3+} luminescence quenching was not observed up to about 873 K, likely due to the larger bandgap of LuAP compared to YAP and the lower energy of the ground Ce^{3+} *4f* states in LuAP.

While the downshift of the *5d* energy levels of Ce^{3+} relative to the free Ce^{3+} ion calculated according to the Dorenbos theory did not agree with experimental data, it was reconciled when calculated relative to the bandgap energy of YAP and LuAP. This approach also allowed for the correlation of the observed changes of the *5d* state energies under pressure in LuAP with the pressure–induced changes in the average cation–anion distances.

An alternative hypothesis, proposed in [158], suggests a pressure–induced shift of the energies of both *4f* and *5d* manifolds. This would result in minimal or no pressure dependence of the $4f \leftrightarrow 5d$ transition energies. However, this hypothesis contradicts the Dorenbos model and the common understanding that *5d* states are more sensitive to the surrounding ligands than *4f* states.

The observed change of the pressure coefficients of the $5d \rightarrow 4f$ Ce^{3+} luminescence bands is believed to be associated with pressure–induced structural transitions occurring in the liquid–phase epitaxy grown layers at a pressure of about 15 GPa, and at higher pressures in crystals grown by the micro–pulling down grown method. This difference was related to the larger number of unintentional impurities and structural defects present in the micro–pulled–down crystals than in the single crystalline film.

Moreover, the abrupt changes in the pressure coefficients of Raman modes above 10 GPa in LuAP confirmed the hypothesis of a phase transition. The high–pressure Raman experiment also identified a soft mode with an energy of 455.4 cm^{-1} at ambient pressure, the energy of which decreased with the pressure increase.

VIII.2. Cesium lead bromide perovskite

In this study, the luminescence properties of cesium lead bromide perovskite were investigated using single crystal samples synthesized by two different methods. The focus was on high–pressure luminescence at low temperatures. The resulting luminescence spectra showed a rich structure, which was analyzed to identify three main groups of lines: (i) direct (free) and indirect (Rashba) excitons and their phonon replicas, (ii) a broad defect band, and (iii) a line at around 540 nm at low temperatures that appeared in all samples at high excitation power densities and was dominant for the sample synthesized from solution.

The origin of the 540 nm line is unclear, as it contradicts different observations. It is observed that the intensity of the 540 nm line increases with the power density of the excitation light, which contradicts the origin of the line from defects (Br–vacancies), formed during mechanical treatment. Furthermore, the bi–excitonic origin of the 540 nm line contradicts the temperature dependence of the line.

The correlation between the 540 nm line and the broad defect band suggests a possible relationship between their origins. One hypothesis is that the 540 nm line arises from Br–vacancies, and the broad band luminescence originates from the defect band with an exponential distribution below the band gap. The presence of Br–vacancies may enhance the structural disorder, leading to the coexistence of the 540 nm line and defect band. However, these assumptions necessitate a fine theoretical model and experimental verification to gain a better understanding of the luminescence properties of $CsPbBr_3$.

It was shown that the structure fluctuation of the sample influences the luminescent properties. First of all, there is a central peak in the Raman spectra of $CsPbBr_3$, from which the quantitative estimation of the structure fluctuation was made. Afterward, it was shown that many luminescent properties correlate with the structure fluctuation behavior on temperature. It was observed that:

- the dependence of the Urbach energy on temperature correlates strongly with the structure fluctuation;
- the defect luminescence is quenched in the same temperature region, where the intensity of the structure fluctuation increases;
- the Rashba split is proportional to the structure fluctuation.

In this study, low–temperature high–pressure luminescence was measured for the first time, allowing for the resolution of free and Rashba excitons under high pressure. The results showed that as pressure increased from ambient to about 1 GPa, the intensity of the Rashba exciton increased, while the intensity of the free exciton decreased. However, with further pressure increase, a reverse trend was observed until both free and Rashba excitons started to quench. The changes in the relative intensity of the free and Rashba excitons were explained by changes in the probability of nonradiative deexcitation from the free excitons to the Rashba excitons states. As the pressure increased up to 1.3 GPa, the Rashba splitting decreased, resulting in an increase in Rashba exciton intensity due to the increased probability of nonradiative deexcitation. As the pressure increased above 1.3 GPa, the Rashba splitting decreased, leading to an increase in free exciton intensity. The discrepancy in the pressure values where the Rashba splitting was the smallest (1.3 GPa) and where the Rashba exciton intensity was the lowest (1 GPa) was caused by the low precision of the non–linear dependency fitting with straight lines.

Another novelty in the results was the blue emission of the bulk $CsPbBr_3$ under high pressure. This blue emission was explained by the rapid expansion of the $CsPbBr_3$ band gap at high pressures, reported before.

VIII.3. Commonly seen phase transition

In LuAP, a change in the behavior of certain parameters was observed at pressures around 10–15 GPa, including shifts in the position of the luminescence lines of Eu^{3+} and Ce^{3+} and Raman line shifts. This suggests the occurrence of a phase transition in this pressure range. Similar behavior has been observed in $CsPbBr_3$, where an isostructural phase transition occurs at a much lower pressure of around 1 GPa, related to a change in the compressibility of the Pb–Br distance. The pressure coefficients of the Raman lines in both LuAP and $CsPbBr_3$ exhibit a small change at their respective phase transition pressures, with smaller coefficients at higher pressures. This similarity in the Raman spectra supports the assumption that an isostructural phase transition occurs in LuAP. Further investigation, including high–pressure XRD measurements and theoretical calculations, is necessary to confirm this assumption.

IX. Appendixes

IX.1. Curriculum vitae of the author

Education:

- September 2010 – June 2014, Bachelor's degree in Physics with specialization in Experimental Physics, Faculty of Physics of Ivan Franko National University, Lviv, Ukraine.
- September 2014 – June 2016, Master's degree in Physics with specialization in Experimental Physics, Faculty of Physics of Ivan Franko National University, Lviv, Ukraine.
- June 2016 – Master thesis defense. Thesis topic: "Luminescence of rare earth ions in fluoride nanocrystals"
- October 2016 – October 2022, a Ph.D. student at the Institute of Physics of the Polish Academy of Science (IP PAS)

Current research activities and research interests:

- Characterization of luminescent properties of cesium lead halide perovskites as a function of temperature and high quasi–hydrostatic pressure.
- Characterization of luminescent properties of yttrium and rare–earth aluminum oxide perovskite single crystal films, and their doping with Ce^{3+} and Eu^{3+} ions.
- Characterization of luminescent properties of the Mn^{2+} ion in $Gd(Zn, Mg)B_5O_{10}$ under high pressure.

My research interests are focused on materials with the perovskite structure. My primary research focuses on rare–earth aluminum oxide perovskites. These materials have the potential for X–ray micro–imaging applications, as the presence of rare–earth increases the absorption of high–energy photons and particles, and thin films can be produced using liquid–phase epitaxy. My secondary research involves the cesium lead halide perovskites, which have excellent optoelectrical properties and are highly promising for various applications. A unique property of these perovskites is their absence of luminescence quenching with increased defects concentration in the lattice, resulting in high–quality luminescence and electrical properties.

I primarily use spectroscopic methods such as excitation and emission spectra, absorption and decay time measurements, and Raman spectroscopy to characterize the properties of these materials. I conduct measurements under various conditions, including ambient conditions, as well as at different temperatures and high quasi–hydrostatic pressures. My experience in programming with LabView, C#, and MathLab allows me to automate measurement setups and analyze data more efficiently.

Languages: English, Polish, Italian, Ukrainian (native)

IX.2. Copyright

This work builds upon earlier published results, and while the text has been substantially rewritten, some figures and tables have been reused in their original form. The articles from which these figures were taken, along with the relevant copyright documentation from the respective journals, are provided below.

Title of the article: “Influence of high pressure on Ce^{3+} luminescence in $LuAlO_3$ and $YAlO_3$ single crystals and single crystalline layers”

Authors: Lev–Ivan Bulyk, Ajeesh Kumar Somakumar, Hanka Przybylińska, P. Ciepielewski, Yu. Zorenko, Ya. Zhydachevskyy, I. Kudryavtseva, V. Gorbenko, A. Lushchik, M.G. Brik, Y. Syrotych, S. Witkiewicz–Łukaszek, A. Fedorov, Andrzej Suchocki

Publication: Journal of Luminescence

Publisher: Elsevier

Date: December 2022

© 2019 Elsevier B.V. All rights reserved. Open access.

Full citation can be found in chapter III, page 6, under number 1

Used content:

Figure in cited work	Figure in this work	Table in cited work	Table in this work
Fig. 1	Fig. 25	Table 1	Table 5
Fig. 2	Fig. 26	Table S1	Table 3
Fig. 3	Fig. 27		
Fig. 4	Fig. 28		
Fig. 5	Fig. 29		
Fig. 6	Fig. 30		
Fig. 7	Fig. 31		
Fig. 8	Fig. 32		
Fig. 9	Fig. 33		
Fig. 10	Fig. 34		
Fig. 11	Fig. 35		
Fig. 12	Fig. 36		

Title of the article: “Influence of high pressure on Eu^{3+} luminescence in epitaxial RAlO$_3$ (R = Gd, Tb, Lu, $Gd_{0,6}Lu_{0,4}$, or Y) single crystalline films”

Authors: Lev–Ivan Bulyk, Yu. Zorenko, V. Gorbenko, Andrzej Suchocki

Publication: Journal of Luminescence

Publisher: Elsevier

Date: Aprile 2020

© 2019 Elsevier B.V. All rights reserved

Full citation can be found in chapter III, page 6, under number 2

Used content:

Figure in cited work	Figure in this work	Table in cited work	Table in this work
Fig. 2	Fig. 17	Table 1	Table 2
Fig. 3	Fig. 18		
Fig. 4	Fig. 19		
Fig. 5	Fig. 20		

Fig. 6	Fig. 21
Fig. 7	Fig. 23
Fig. 8	Fig. 22
Fig. 9	Fig. 24

Both of the aforementioned cases adhere to the copyright rules stated on the web page [159], and are duplicated in this work in chapter IX.3, page 104.

IX.3. Elsevier Copyright

ELSEVIER (https:/www.elsevier.com) (https: /www.elsevier.com/search–results)

Copyright

Overview Author rights Institution rights Government rights Find out more

Overview

In order for Elsevier to publish and disseminate research articles, we need certain publishing rightsfrom authors, which are determined by a publishing agreement between the author and Elsevier.

For articles published open access, the authors license exclusive rights in their article to Elsevier where a CC BY–NC–ND end user license is selected, and license non–exclusive rights where a CC BY end user license is selected.

For articles published under the subscription model, the authors typically transfer copyright to Elsevier. In some circumstances, authors may instead grant us (or the learned society for whom we publish) an exclusive license to publish and disseminate their work.

Regardless of whether they choose to publish open access or subscription with Elsevier, authors have many of the same rights under our publishing agreement, which support their need to share,disseminate and maximize the impact of their research.

For open access articles, authors will also have additional rights, depending on the Creative Commons end user license that they select. This Creative Commons license sets out the rights that readers (as well as the authors) have to reuse and share the article: please see here (https://www.elsevier.com/about/policies/open–access–licenses) for more information on how articles can be reused and shared under these licenses.

This page aims to summarise authors’ rights when publishing with Elsevier; these are explained in more detail in the publishing agreement between the author and Elsevier.

Irrespective of how an article is published, Elsevier is committed to protect and defend authors’ works and their reputation. We take allegations of infringement, plagiarism, ethical disputes, and fraud very seriously.

Author rights

The below table explains the rights that authors have when they publish with Elsevier, for authors who choose to publish either open access or subscription. These apply to the corresponding author and all co–authors.

Author rights in Elsevier’s proprietary journals	Published open access	Published subscription
Retain patent and trademark rights	√	√
Retain the rights to use their research data freely without any restriction	√	√
Receive proper attribution and credit for their published work	√	√
Re–use their own material in new works without permissionor payment (with full acknowledgement of the original article): Extend an article to book length 2. Include an article in a subsequent compilation of their ownwork 3. Reuse portions, excerpts, and their own figures or tablesin other works.	√	√
Use and share their works for scholarly purposes (with full acknowledgement of the original article): 1. In their own classroom teaching. Electronic and physical distribution of copies is permitted IN an author is speaking at a conference, they can present the article and distribute copies to the attendees 3. Distribute the article, including by email, to their students and to research colleagues who they know for their personal use 4. Share and publicize the article via Share Links, which offers 50 days’ free access for anyone, without signup or registration 5. Include in a thesis or dissertation (provided this is not published commercially) 6. Share copies of their article privately as part of an invitation–only work group on commercial sites with which the publisher has a hosting agreement	√	√
Publicly share the preprint on any website or repository at any time.	√	√

Publicly share the accepted manuscript on non–commercial sites	√	√ using a CCBY–NC–ND license and usually only after an embargo period (see Sharing Policy (https://www.elsevier.com/about/policies/sharing) for more information)
Publicly share the final published article	√ in line with the author's choice of enduser license	×
Retain copyright	√	×

Institution rights

Regardless of how the author chooses to publish with Elsevier, their institution has the right to use articles for classroom teaching and internal training. Articles can be used for these purposes throughout the author's institution, not just by the author:

Institution rights in Elsevier's proprietary journals (providing full acknowledgement of the original article is given)	All articles
Copies can be distributed electronically as well as in physical form for classroom teaching and internal training purposes	√
Material can be included in coursework and courseware programs for use within theinstitution (but not in Massive Open Online Courses)	√
Articles can be included in applications for grant funding	√
Theses and dissertations which contain embedded final published articles as part of the formal submission can be posted publicly by the awarding institution with DOI links back to the formal publication on ScienceDirect	√

Government rights

For US government employees, works created within the scope of their employment are considered to be public domain and Elsevier's publishing agreements do not require a transfer orlicense of rights for such works.

In the UK and certain commonwealth countries, a work created by a government employee is copyrightable, but the government may own the copyright (Crown copyright). Click here (https://www.elsevier.com/open–access/agreements/uk–national–archives) for information about UK government employees publishing open access.

Find out more

- Download a sample publishing agreement for articles financed by journal subscriptionsin English and French.
- Download a sample publishing agreement for articles published open access with a commercial user license (CC BY) and a+ non–commercial user license. (CC BY–NC–ND)
- For authors who wish to self–archive see our sharing guidelines (https:/www.elsevier.com/about/policies/sharing).
- See our author pages (https://www.elsevier.com/authors/submit–your–paper/sharing–and–promoting–your–articIe)for further details about how to promote your article.
- See our hosting (https://www.elsevier.com/about/policies/hosting) page for additionalinformation on hosting research published by Elsevier.
- For use of Elsevier material not defined here please see our permissions page (https://www.elsevier.com/about/policies/copyright/permissions) or visit the Permissions Support Center (https:/service.eIsevier.com/app/contact/supporthub/permissions–helpdesk)
- IN an author has become aware of a possible plagiarism, fraud or infringement we recommend contacting their Elsevier publishing contact who can then liaise with our in–house legal department.
- If you are publishing in a society or third party owned journal, they may have different publishing agreements. Please see the journal's Guide for Authors for journal specific copyright information.

X. References

[1] https://www.princeton.edu/~cavalab/tutorials/public/structures/perovskites.html

[2] T. A. Liebsch and V. L. Sobolev, Coexistence of phases and interphase boundaries in $BaTiO_3$, May 2013 Journal of Applied Physics 113(19), doi: 10.1063/1.4806996

[3] https://en.wikipedia.org/wiki/Goldschmidt_tolerance_factor

[4] V. M. Goldschmidt, Die Gesetze der Krystallochemie, Naturwissenschaften volume 14, pages 477–485 (1926), doi: 10.1007/bf01507527

[5] Christopher J. Bartel, Christopher Sutton, Bryan R. Goldsmith, Runhai Ouyang, Charles B. Musgrave, Luca M. Ghiringhelli, Matthias Scheffler, New tolerance factor to predict the stability of perovskite oxides and halides, SCIENCE ADVANCES, Vol 5, Issue 2, (2019), doi: 10.1126/sciadv.aav0693

[6] Toyoto Sato, Shigeyuki Takagi, Stefano Deledda, Bjørn C. Hauback, and Shinichi Orimo, Extending the applicability of the Goldschmidt tolerance factor to arbitrary ionic compounds, Scientific Reports, volume 6, Article number: 23592, (2016), doi: 10.1038/srep23592

[7] Alexander E. Fedorovskiy, Nikita A. Drigo, Mohammad Khaja Nazeeruddin, The Role of Goldschmidt's Tolerance Factor in the Formation of A_2BX_6 Double Halide Perovskites and its Optimal Range, Small Methods, Volume 4, Issue 5, (2020), doi: 10.1002/smtd.201900426

[8] Mitsunori Yada, Masahumi Ohya, Kaoru Ohe, Masato Machida, and Tsuyoshi Kijima, Porous Yttrium Aluminum Oxide Templated by Alkyl Sulfate Assemblies, Langmuir 2000, 16, 1535–1541, doi: 10.1021/la990493p

[9] V. Gorbenko, T. Zorenko, K. Paprocki, F. Riva, P. A. Douissard, T. Martin, Ya. Zhydachevskii, A. Suchocki, A. Fedorovd and Yu. Zorenko. Epitaxial growth of single crystalline film scintillating screens based on Eu^{3+} doped $RAlO_3$ (R = Y, Lu, Gd, Tb) perovskites. CrystEngComm 20, 937–945 (2018) doi: 10.1039/C7CE02074K

[10] Kuro, T., Nakauchi, D., Okada, G., Kawaguchi, N, and Yanagida, T. X–ray induced luminescence properties of $(Y,Eu)AlO_3$ single crystals. Opt. Mater. (Amst). 64, 282–287 (2017) doi: 10.18494/SAM.2020.2742

[11] Editors: Govindhan Dhanaraj, Kullaiah Byrappa, Vishwanath Prasad, Michael Dudley, Springer Handbook of Crystal Growth, chapter: "Liquid–Phase Epitaxy of Advanced Materials", link: https://link.springer.com/chapter/10.1007/978–3–540–74761–1_31

[12] T. Zorenko, V. Gorbenko, A. Petrosyan, W. Gieszczyk, P. Bilski, and Yu. Zorenko. Intrinsic and defect–related luminescence of $YAlO_3$ and $LuAlO_3$ single crystals and films. Opt. Mater. (Amst). 86, 376–381 (2018) doi: 10.3390/ma13092032

[13] J. Chen, G. Zhao, Y. Sun, and T. Liu, Theoretical study on the electronic structures and optical properties of Y AlO_3 crystal with interstitial oxygen atom. Solid State Commun. 150, 897–900 (2010) doi: 10.1016/j.ssc.2010.01.035

[14] P. A. Tanner, Some misconceptions concerning the electronic spectra of tri–positive europium and cerium. Chem. Soc. Rev. 42, 5090–101 (2013) doi: 10.1039/c3cs60033e

[15] J.A. Mares, N. Cechova, M. Nikl, J. Kvapil, R. Kratky, and J. Pospısil. Cerium–doped $RE^{3+}AlO_3$ perovskite scintillators: Spectroscopy and radiation induced defects. J. Alloys Compd. 275–277, 200–204 (1998), doi: 10.1016/S0925–8388(98)00303–X

[16] X. Wu, S. Qin, and Z. Wu, Generalized gradient approximation calculations of the pressure–induced phase transition of $YAlO_3$ perovskite. J. Phys. Condens. Matter 18, 3907–3916 (2006), doi: 10.1088/0953–8984/18/16/001

[17] Lev–Ivan Bulyk, Yu Zorenko, V. Gorbenko, Andrzej Suchocki, Influence of high pressure on Eu^{3+} luminescence in epitaxial $RAlO_3$ (R = Gd, Tb, Lu, $Gd_{0,6}Lu_{0,4}$, or Y) single crystalline films, Journal of Luminescence 220 (2020) 116991, doi: 10.1016/j.jlumin.2019.116991

[18] A. Lempicki, J. Glodo, Ce–doped scintillators: LSO and LuAP, Nuclear Instruments and Methods in Physics Research A 416 (1998) 333–344, doi: 10.1016/S0168–9002(98)00689–5

[19] Samah Al–Qaisi, R. Ahmed, Bakhtiar Ul Haq, D. P. Rai, S. A. Tahir, A comprehensive first–principles computational study on the physical properties of lutetium aluminum perovskite $LuAlO_3$, Materials Chemistry and Physics, 250 (2020) 123148, doi: 10.1016/j.matchemphys.2020.123148

[20] M. G. Brik, C.–G. Ma, M. Piasecki, A. Suchocki, Locating impurity and defect levels in the host band gap by first–principles calculations: Pure and Ce^{3+}–doped $YAlO_3$, Optical Materials 113 (2021) 110843, doi: 10.1016/j.optmat.2021.110843

[21] V. Babin, V. Gorbenko, A. Makhov, J.A. Mares, M. Nikl, S. Zazubovich, Yu. Zorenko, Luminescence characteristics of Pb^{2+} centres in undoped and Ce^{3+}–doped $Lu_3Al_5O_{12}$ single–crystalline films and Pb^{2+}–Ce^{3+} energy transfer processes, J. Lumin. 127 (2007) 384–390, doi: 10.1016/j.jlumin.2007.01.011

[22] Yu Zorenko, T. Voznyak, V. Gorbenko, T. Zorenko, A. Voloshinovskiĭ, V. Vistovsky, M. Nikl, K. Nejezchleb, V. Kolobanov, D. Spasskiĭ,

Luminescence spectroscopy of excitons and antisite defects in $Lu_3Al_5O_{12}$ single crystals and single–crystal films, Opt. Spectrosc. 104 (2008) 75–87, doi: 10.1134/S0030400X08010116

[23] Yu.V. Zorenko, A.S. Voloshinovskii, G.B. Stryganyuk, I.V. Konstankevych, Ultraviolet Luminescence of Single Crystals and Single–Crystal Films of $YAlO_3$. Optics and Spectroscopy. 2004. 96, № 1. P.70–76, doi: 10.1134/1.1643988

[24] Yu. V Zorenko, V. I Gorbenko, Growth and luminescence properties of single–crystalline films of $RAlO_3$ (R = Lu, Lu–Y, Y, Tb) perovskite. Phys. Solid State 2009, 51, 1800–1808, doi: 10.1134/S1063783409090078

[25] Y. Zorenko, V. Gorbenko, T. Zorenko, T. Voznyak, F. Riva, P. A. Douissard, T. Martin, A. Fedorov, A. Suchocki, Y. Zhydachevskii, Growth and luminescent properties of single crystalline films of Ce^{3+} doped $Pr_{1-x}Lu_xAlO_3$ and $Gd_{1-x}Lu_xAlO_3$ perovskites. J. Cryst. Growth 2017, 457, 220–226, doi: 10.1016/j.jcrysgro.2016.02.020

[26] F. Riva, P–.A. Douissard, T. Martin, F. Carla, Y.V. Zorenko, C. Dujardin, Epitaxial growth of gadolinium and lutetium–based aluminum perovskites thin film for X–rays micro–imaging applications, CrystEngComm, 2016, V.18, P. 608–615, doi: 10.1039/C5CE01938A

[27] P. Dorenbos, Fundamental Limitations in the Performance of Ce^{3+}–, Pr^{3+}–, and Eu^{2+}–Activated Scintillator, IEEE Transactions on Nuclear Science, volume 57, issue 3, pages 1162–1167 (2010), doi: 10.1109/TNS.2009.2031140

[28] MØLLER, C. Crystal Structure and Photoconductivity of Cæsium Plumbohalides. Nature 182, 1436 (1958), doi: 10.1038/1821436a0

[29] Nabonswende Aida Nadege Ouedraogo, Yichuan Chen, Yue Yue Xiao, Qi Meng, Chang Bao Han, Hui Yan, Yongzhe Zhang, Stability of all–inorganic perovskite solar cells, Nano Energy 67 (2020) 104249, doi: 10.1016/j.nanoen.2019.104249

[30] Yue Lin, Xi Zheng, Zhibin Shangguan, Guolong Chen, Weizhi Huang, Weijie Guo, Xiaotong Fan, Xiao Yang, Zijun Zhao, Tingzhu Wu, and Zhong Chen, All–inorganic encapsulation for remarkably stable cesium lead halide perovskite nanocrystals: toward full–color display applications, J. Mater. Chem. C, 2021, 9, 12303, doi: 10.1039/d1tc02685b

[31] V. B. Mykhaylyk, H. Kraus, V. Kapustianyk, H. J. Kim, P. Mercere, M. Rudko, P. Da Silva, O. Antonyak, and M. Dendebera, Bright and fast scintillations of an inorganic halide perovskite $CsPbBr_3$ crystal at cryogenic temperatures, Scientific Reports, 10, 8601, (2020), doi: 10.1038/s41598–020–65672–z

[32] Yang Liu, Ju Wang, Lin Zhang, Wei Liu, Cuncun Wu, Congyue Liu, Zhaoxin Wu, Xiao, Zhijian Chen, and Shufeng Wang, Exciton and bi–exciton mechanisms in amplified spontaneous emission from $CsPbBr_3$ perovskite thin films, Optics Express, Vol. 27, Issue 20, pp. 29124–29132 (2019), doi: 10.1364/OE.27.029124

[33] Xiangzhou Lao, Zhi Yang, Zhicheng Su, Zilan Wang, Honggang Ye, Minqiang Wang, Xi Yaob and Shijie Xu, Luminescence and thermal behaviors of free and trapped excitons in cesium lead halide perovskite nanosheets, Nanoscale, 2018, 10, 9949, doi: 10.1039/c8nr01109e

[34] Suhas Mahesh, Nakita K. Noel, Matthew T. Klug, Jong Chul Lim, Jonathan H. Warby, James M. Ball, M. Herz, Michael B. Johnston, Henry J. Snaith, Solution–Processed All–Perovskite Multijunction Solar Cells, Volume 3, Issue 2, 2019, Pages 387–401, doi: 10.1016/j.joule.2019.01.007

[35] Best Research–Cell Efficiency Chart from NREL web–page: https://www.nrel.gov/pv/cell–efficiency.html

[36] Natalia Yantara, Saikat Bhaumik, Fei Yan, Dharani Sabba, Herlina A. Dewi, Nripan Mathews, Pablo P. Boix, Hilmi Volkan Demir, and Subodh Mhaisalkar, Inorganic Halide Perovskites for Efficient Light–Emitting Diodes, J. Phys. Chem. Lett., 6, 4360−4364, (2015), doi: 10.1021/acs.jpclett.5b02011

[37] Yan Meng, Mahshid Ahmadi, Xiaoyan Wu, Tianfei Xu, Long Xu, Zuhong Xiong, Ping Chen, High performance and stable all–inorganic perovskite light emitting diodes by reducing luminescence quenching at PEDOT:PSS/Perovskites interface, Organic Electronics 64, 47–53, (2019), doi: 10.1016/j.orgel.2018.10.014

[38] Jianxun Lu, Wenjing Feng, Guanding Mei, Jiayun Sun, Chuanzhong Yan, Di Zhang, Kebin Lin, Dan Wu, Kai Wang, and Zhanhua Wei, Ultrathin PEDOT:PSS Enables Colorful and Efficient Perovskite Light–Emitting Diodes, Adv. Sci. 2020, 7, 2000689, doi: 10.1002/advs.202000689

[39] Zahra Andaji–Garmaroudi, Mojtaba Abdi–Jalebi, Dengyang Guo, Stuart Macpherson, Aditya Sadhanala, Elizabeth M. Tennyson, Edoardo Ruggeri, Miguel Anaya, Krzysztof Galkowski, Ravichandran Shivanna, Kilian Lohmann, Kyle Frohna, Sebastian Mackowski, Tom J. Savenije, Richard H. Friend, and Samuel D. Stranks, A Highly Emissive Surface Layer in Mixed–Halide Multication Perovskites, Adv. Mater., 31, 1902374, (2019), doi: 10.1002/adma.201902374

[40] Alexandra Szemjonov, Krzysztof Galkowski, Miguel Anaya, Zahra Andaji–Garmaroudi, Tomi K. Baikie, Sebastian Mackowski, Iain D. Baikie,

Samuel D. Stranks, and M. Saiful Islam, Impact of Oxygen on the Electronic Structure of Triple–Cation Halide Perovskites, ACS Materials Lett., 1, 506−510, (2019), doi: 10.1021/acsmaterialslett.9b00294

[41] I.P. Pashuk, N.S. Pidzyrajlo, M.G. Matsko, Exciton Absorption, Luminescence and Resonance Raman Scattering in $CsPbCl_3$ and $CsPbBr_3$ Crystals at Low Temperatures, Fiz. Tverd. Tela. 23(7) (1981) 2162–2165

[42] M. Dendebera, Y. Chornodolskyy, R. Gamernyk, O. Antonyak, I. Pashuk, S. Myagkota, I. Gnilitskyi, V. Pankratov, V. Vistovskyy, V. Mykhaylyk, M. Grinberg, A. Voloshinovskii, Time resolved luminescence spectroscopy of $CsPbBr_3$ single crystal, May 2020 Journal of Luminescence 225(7):117346, doi: 10.1016/j.jlumin.2020.117346

[43] Mingzhi Zhang, Zhiping Zheng, Qiuyun Fu, Zheng Chen, Jianle He, Sen Zhang, Liang Yan, Yunxiang Hu and Wei Luo, Growth and characterization of all–inorganic lead halide perovskite semiconductor $CsPbBr_3$ single crystals, CrystEngComm, 19, 6797, (2017), doi: 10.1039/c7ce01709j

[44] Constantinos C. Stoumpos, Christos D. Malliakas, John A. Peters, Zhifu Liu, Maria Sebastian, Jino Im, Thomas C. Chasapis, Arief C. Wibowo, Duck Young Chung, Arthur J. Freeman, Bruce W. Wessels, and Mercouri G. Kanatzidis, Crystal Growth of the Perovskite Semiconductor $CsPbBr_3$: A New Material for High–Energy Radiation Detection, Cryst. Growth Des., 13, 2722−2727, (2013), doi: 10.1021/cg400645t

[45] Dana M. Calistru, L. Mihut, S. Lefrant, I. Baltog, Identification of the symmetry of phonon modes in $CsPbCl_3$ in phase IV by Raman and resonance–Raman scattering, Journal of Applied Physics 82, 5391 (1997); doi: 10.1063/1.366307

[46] Y. Fujii and S. Hoshino, Neutron scattering study on phase transitions of $CsPbCl_3$, Physical Review B 9, 4549, (1973) doi: 10.1103/PhysRevB.9.4549

[47] Patrick Cottingham and Richard L. Brutchey, Depressed Phase Transitions and Thermally Persistent Local Distortions in $CsPbBr_3$ Quantum Dots, Chem. Mater. 2018, 30, 6711−6716, doi: 10.1021/acs.chemmater.8b02295

[48] Shunsuke Hirotsu, Jimpei Harada, Masashi Iizumi, and Kazuo Gesi, Structural Phase Transitions in $CsPbBr_3$, J. Phys. Soc. Jpn. 37, pp. 1393-1398 (1974), doi: 10.1143/JPSJ.37.1393

[49] M. Rodova, J. Brozek, K. Knizek and K. Nitsch, Phase transitions in ternary caesium lead bromide, Journal of Thermal Analysis and Calorimetry, Vol. 71 (2003) 667–673, doi: 10.1023/A:1022836800820

[50] Sorb Yesudhas, Maria V. Morrell, Matthew J. Anderson, Carsten A. Ullrich, Curtis Kenney–Benson, Yangchuan Xing, and Suchismita Guha, Pressure–

Induced Phase Changes in Cesium Lead Bromide Perovskite Nanocrystals with and without Ruddlesden − Popper Faults, Chem. Mater. 2020, 32, 785−794, doi: 10.1021/acs.chemmater.9b04157

[51] Long Zhang, Qingxin Zeng, and Kai Wang, Pressure–Induced Structural and Optical Properties of Inorganic Halide Perovskite $CsPbBr_3$, J. Phys. Chem. Lett. 2017, 8, 3752−3758, doi: 10.1021/acs.jpclett.7b01577

[52] J. Gong, H. Zhong, C. Gao, J. Peng, X. Liu, Q. Lin, G. Fang, S. Yuan, Z. Zhang, X. Xiao, Pressure–Induced Indirect–Direct Bandgap Transition of $CsPbBr_3$ Single Crystal and Its Effect on Photoluminescence Quantum Yield, Advanced Science. 9 (2022), doi: 10.1002/advs.202201554

[53] James Endres, David A. Egger, Michael Kulbak, Ross A. Kerner, Lianfeng Zhao, Scott H. Silver, Gary Hodes, Barry P. Rand, David Cahen, Leeor Kronik, and Antoine Kahn, Valence and Conduction Band Densities of States of Metal Halide Perovskites: A Combined Experimental−Theoretical Study, J. Phys. Chem. Lett. 2016, 7, 2722−2729, doi: 10.1021/acs.jpclett.6b00946

[54] Ariadni Boziki, M. Ibrahim Dar, Gwénolé Jacopin, Michael Grätzel, and Ursula Rothlisberger, Molecular Origin of the Asymmetric Photoluminescence Spectra of $CsPbBr_3$ at Low Temperature, J. Phys. Chem. Lett. 2021, 12, 2699−2704, doi: 10.1021/acs.jpclett.1c00263

[55] Jacques I. Pankove, Optical processes in semiconductors, University of Colorado, Dover Publications, Inc., New York, 1971

[56] J.Tauc, Optical properties and electronic structure of amorphous Ge and Si, Materials Research Bulletin, Volume 3, Issue 1, January 1968, Pages 37–46, doi: 10.1016/0025–5408(68)90023–8

[57] A. R. Zanatta, Revisiting the optical bandgap of semiconductors and the proposal of a unified methodology to its determination, Scientific Reports volume 9, Article number: 11225 (2019), doi: 10.1038/s41598–019–47670–y

[58] Y. P. Varshni, Temperature dependence of the energy gap in semiconductors, Physica 34, 149 (1967), doi: 10.1016/0031–8914(67)90062–6

[59] L. Vina, S. Logothetidis, and M. Cardona, Temperature dependence of the dielectric function of gerriianium, Phys. Rev. B 30, 1979, 1984, doi: 10.1103/PhysRevB.30.1979

[60] Chonglong Yu, Zhuo Chen, Jian J. Wang, William Pfenninger, Nemanja Vockic, John T. Kenney, and Kai Shum, Temperature dependence of the band gap of perovskite semiconductor compound $CsSnI_3$, Journal of Applied Physics 110, 063526 (2011), doi: 10.1063/1.3638699

[61] M. Ibrahim Dar, Gwénolé Jacopin, Simone Meloni, Alessandro Mattoni, Neha Arora, Ariadni Boziki, Shaik Mohammed Zakeeruddin, Ursula Rothlisberger, Michael Grätzel, Origin of unusual bandgap shift and dual emission in organic–inorganic lead halide perovskites, Dar et al. Sci. Adv. 2016;2: e1601156, doi: 10.1126/sciadv.1601156

[62] Giovanni Mannino, Ioannis Deretzis, Emanuele Smecca, Antonino La Magna, Alessandra Alberti, Davide Ceratti, and David Cahen. Temperature–Dependent Optical Band Gap in $CsPbBr_3$, $MAPbBr_3$, and $FAPbBr_3$ Single Crystals, J. Phys. Chem. Lett. 2020, 11, 2490−2496, doi: 10.1021/acs.jpclett.0c00295

[63] Lingping Kong, Gang Liu, Jue Gong, Qingyang Hu, Richard D. Schaller, Przemyslaw Dera, Dongzhou Zhang, Zhenxian Liu, Wenge Yang, Kai Zhu, Yuzhao Tang, Chuanyi Wang, Su–Huai Wei, Tao Xu, and Ho–kwang Mao, Simultaneous band–gap narrowing and carrier–lifetime prolongation of organic–inorganic trihalide perovskites, PNAS, 113 (32) 8910–8915, 2016, doi: 10.1073/pnas.1609030113

[64] Yang Huang, Lingrui Wang, Zhuang Ma, and Fei Wang, Pressure–induced band structure evolution of halide perovskites: a first–principles atomic and electronic structure study, Journal Physical Chemistry C 2019, 123, 739−745, doi: 10.1021/acs.jpcc.8b11500

[65] Ke Wei, Zhongjie Xu, Runze Chen, Xin Zheng, Xiangai Cheng, and Tian Jiang, Temperature–dependent excitonic photoluminescence excited by two–photon absorption in perovskite $CsPbBr_3$ quantum dots, Optics Letters, Vol. 41, No. 16, August 15 2016, doi: 10.1364/OL.41.003821

[66] Study of Local Structure in Selected Organic–Inorganic Perovskites in the Pm3jm Phase, Richard J. Worhatch, HyunJeong Kim, Ian P. Swainson, André L. Yonkeu, and Simon J. L. Billinge, Chem. Mater. 2008, 20, 1272–1277, doi: 10.1021/cm702668d

[67] Omer Yaffe, Yinsheng Guo, Liang Z. Tan, David A. Egger, Trevor Hull, Constantinos C. Stoumpos, Fan Zheng, Tony F. Heinz, Leeor Kronik, Mercouri G. Kanatzidis, Jonathan S. Owen, Andrew M. Rappe, Marcos A. Pimenta, and Louis E. Brus, Local Polar Fluctuations in Lead Halide Perovskite Crystals, Phys. Rev. Lett., 118, 136001 (2017), doi: 10.1103/PhysRevLett.118.136001

[68] R. E. Wasylishen, O. Knop, J. B. Macdonald, Cation rotation in methylammonium lead halides, Solid State Commun. 56, 581‑582 (1985), doi: 10.1016/0038–1098(85)90959–7

[69] Lead halide perovskites: Crystal–liquid duality, phonon glass electron crystals, and large polaron formation, Kiyoshi Miyata, Timothy L. Atallah, X.–Y. Zhu, Sci. Adv. 2017;3: e1701469, doi: 10.1126/sciadv.1701469

[70] Franz Urbach, The Long–Wavelength Edge of Photographic Sensitivity and of the Electronic Absorytion of Solids, Phys. Rev. 92, 1324, 1953, doi: 10.1103/PhysRev.92.1324

[71] Martin Ledinsky, Tereza Schonfeldova, Jakub Holovsky, Erkan Aydin, Zdenka Hajkova, Lucie Landova, Neda Neykova, Antonín Fejfar, and Stefaan De Wolf, Temperature Dependence of the Urbach Energy in Lead Iodide Perovskites, J. Phys. Chem. Lett. 2019, 10, 1368−1373, doi: 10.1021/acs.jpclett.9b00138

[72] Naomi Falsini, Giammarco Roini, Andrea Ristori, Nicola Calisi, Francesco Biccari, and Anna Vinattieri, Analysis of the Urbach tail in cesium lead halide Perovskites, J. Appl. Phys. 131, 010902 (2022); doi: 10.1063/5.0076712

[73] O. Yu. Posudievsky, N. V. Konoshchuk, V. L. Karbivskyy, O. P. Boiko, V. G. Koshechko, and V. D. Pokhodenko, Structural and spectral characteristics of mechanochemically prepared $CsPbBr_3$, Theoretical and Experimental Chemistry, Vol. 53, No. 4, September, 2017, doi: 10.1007/s11237–017–9520–z

[74] Zhuang Zhao, Manyi Zhong, Weichang Zhou, Yuehua Peng, Yanling Yin, Dongsheng Tang, and Bingsuo Zou, Simultaneous Triplet Exciton−Phonon and Exciton−Photon Photoluminescence in the Individual Weak Confinement $CsPbBr_3$ Micro/Nanowires, J. Phys. Chem. C 2019, 123, 25349−25358, doi: 10.1021/acs.jpcc.9b06643

[75] Mengling Liao, Beibei Shan, and Ming Li, In Situ Raman Spectroscopic Studies of Thermal Stability of All–Inorganic Cesium Lead Halide ($CsPbX_3$, X = Cl, Br, I) Perovskite Nanocrystals, Mengling Liao, Beibei Shan, and Ming Li, J. Phys. Chem. Lett. 2019, 10, 1217−1225, doi: 10.1021/acs.jpclett.9b00344

[76] All–inorganic perovskite $CsPbBr_3$ microstructures growth via chemical vapor deposition for high–performance photodetectors, Xindi Mo, Xing Li, Guozhang Dai, Pei He, Jia Sun, Han Huang and Junliang Yang, Nanoscale, 2019, 11, 21386, doi: 10.1039/c9nr06682a

[77] Claudiu M. Iaru, Annalisa Brodu, Niels J. J. van Hoof, Stan E. T. ter Huurne, Jonathan Buhot, Federico Montanarella, Sophia Buhbut, Peter C. M. Christianen, Daniël Vanmaekelbergh, Celso de Mello Donega, Jaime Gòmez Rivas, Paul M. Koenraad, and Andrei Yu. Silov, Fröhlich interaction dominated by a single phonon mode in $CsPbBr_3$, Nat Commun 12, 5844 (2021), doi: 10.1038/s41467–021–26192–0

[78] Hao Long, Xiang Peng, Kebin Lin, Liqiang Xie, Jianxun Lu, Baoping Zhang, Leiying Ying, Zhanhua Wei, Acoustic phonon–exciton interaction by extremely strong exciton confinement and large phonon energy in $CsPbBr_3$

perovskite, Applied Physics Express 12, 052003 (2019), doi: 10.7567/1882–0786/ab0dd5

[79] C. Carabatos–Nedelec, M. Oussaid and K. Nitsch, Raman scattering investigation of cesium plumbochloride, $CsPbCl_3$, phase transitions, J. Raman Spectrosc. 2003; 34: 388–393, doi: 10.1002/jrs.1005

[80] Zhang, M.; Zheng, Z.; Fu, Q.; Guo, P.; Zhang, S.; Chen, C.; Chen, H.; Wang, M.; Luo, W.; Tian, Y. Determination of Defect Levels in Melt–Grown All–Inorganic Perovskite $CsPbBr_3$ Crystals by Thermally Stimulated Current Spectra. J. Phys. Chem. C 2018, 122, 10309, doi: 10.1021/acs.jpcc.8b01532

[81] Zhang, B.; Wang, F.; Zhang, H.; Xiao, B.; Sun, Q.; Guo, J.; Ahmed, B. H.; Shao, A.; Zhou, J. Defect Proliferation in $CsPbBr_3$ Crystal Induced by Ion Migration. Appl. Phys. Lett. 2020, 116, No. 063505, doi: 10.1063/1.5134108

[82] Xinlei Zhang, Fangbao Wang, Bin–Bin Zhang, Gangqiang Zha, and Wanqi Jie, Ferroelastic Domains in a $CsPbBr_3$ Single Crystal and Their Phase Transition Characteristics: An in Situ TEM Study, Cryst. Growth Des. 2020, 20, 4585−4592, doi: 10.1021/acs.cgd.0c00370

[83] Yongtao Liu, Alex Belianinov, Liam Collins, Roger Proksch, Anton V. Ievlev, Bin Hu, Sergei V. Kalinin, Olga S. Ovchinnikova, Ferroic twin domains in metal halide perovskites, MRS Advances, Volume 4, Issue 51–52, doi: 10.1557/adv.2019.358

[84] Keith P. McKenna, Electronic Properties of {111} Twin Boundaries in a Mixed–Ion Lead Halide Perovskite Solar Absorber, ACS Energy Letters 2018 3 (11), 2663–2668, doi: 10.1021/acsenergylett.8b01700

[85] Э. И. Рашба, Симметрия энергетических зон в кристаллах типа вюрцита. I. Симметрия зон без учета спин–орбитального взаимодействия, Физика тверд. тела, 1(3), 407–421 (1959)

[86] Э. И. Рашба, В. И. Шека, Симметрия энергетических зон в кристаллах типа вюрцита. II. Симметрия зон с учётом спиновых взаимодействий, Физика тверд. тела, 1(2), 162–176 (1959)

[87] Supplemental Material to the paper by G. Bihlmayer, O. Rader, and R. Winkler, Focus on the Rashba effect, New J. Phys. 17, 050202 (2015), link: http://iopscience.iop.org/1367–2630/17/5/050202/media/njp050202_suppdata.pdf

[88] G. Bihlmayer, O. Rader and R. Winkler, Focus on the Rashba effect, New J. Phys. 17 (2015) 050202. doi: 10.1088/1367–2630/17/5/050202

[89] Jahn–Teller effect. (2022, July 11). In Wikipedia. https://en.wikipedia.org/wiki/Jahn%E2%80%93Teller_effect

[90] Rashba effect. (2022, September 12). In Wikipedia. https://en.wikipedia.org/wiki/Rashba_effect

[91] Hongsun Ryu, Dae Young Park, Kyle M. McCall, Hye Ryung Byun, Yongjun Lee, Tae Jung Kim, Mun Seok Jeong, Jeongyong Kim, Mercouri G. Kanatzidis, and Joon I. Jang, Static Rashba Effect by Surface Reconstruction and Photon Recycling in the Dynamic Indirect Gap of $APbBr_3$ (A = Cs, CH_3NH_3) Single Crystals, J. Am. Chem. Soc. 2020, 142, 50, 21059–21067, doi: 10.1021/jacs.0c09132

[92] Bo Wu, Haifeng Yuan, Qiang Xu, Julian A. Steele, David Giovanni, Pascal Puech, Jianhui Fu, Yan Fong Ng, Nur Fadilah Jamaludin, Ankur Solanki, Subodh Mhaisalkar, Nripan Mathews, Maarten B.J. Roeffaers, Michael Grätzel, Johan Hofkens & Tze Chien Sum, Indirect tail states formation by thermal–induced polar fluctuations in halide perovskites, NATURE COMMUNICATIONS, (2019) 10:484, doi: 10.1038/s41467–019–08326–7

[93] Julian A. Steele, Pascal Puech, Bartomeu Monserrat, Bo Wu, Ruo Xi Yang, Thomas Kirchartz, Haifeng Yuan, Guillaume Fleury, Eduard Fron, Masoumeh Keshavarz, Elke Debroye, Guofu Zhou, Tze Chien Sum, Aron Walsh, Johan Hofkens, and Maarten B. J. Roeffaers, Role of Electron–Phonon Coupling in the Thermal Evolution of Bulk Rashba–Like Spin–Split Lead Halide Perovskites Exhibiting Dual–Band Photoluminescence, ACS Energy Lett. 2019, 4, 9, 2205–2212 Publication Date:August 19, 2019, doi: 10.1021/acsenergylett.9b01427

[94] Maya Isarov, Liang Z Tan, Jenya Tilchin, Freddy T Rabouw, Maryna I Bodnarchuk, Relinde J A van Dijk–Moes, Rotem Carmi, Yahel Barak, Alyssa Kostadinov, Itay Meir, Daniel Vanmaekelbergh, Maksym V Kovalenko, Andrew M Rappe, and Efrat Lifshitz, Polarized emission in II–VI and perovskite colloidal quantum dots, Maya Isarov et al 2017 J. Phys. B: At. Mol. Opt. Phys. 50 214001, doi: 10.1088/1361–6455/aa8dd4

[95] Chong Wang, Yanan Wang, Xinghua Su, Viktor G. Hadjiev, Shenyu Dai, Zhaojun Qin, Hector A. Calderon Benavides, Yizhou Ni, Qiang Li, Jie Jian, Md. Kamrul Alam, Haiyan Wang, Francisco C. Robles Hernandez, Yan Yao, Shuo Chen, Qingkai Yu, Guoying Feng, Zhiming Wang, and Jiming Bao, Extrinsic Green Photoluminescence from the Edges of 2D Cesium Lead Halides, Adv. Mater. 2019, 31, 1902492, DOI: 10.1002/adma.201902492

[96] Keisei Shibata, Jiyu Yan, Yuji Hazama, Shaoqiang Chen, and Hidefumi Akiyama, Exciton Localization and Enhancement of the Exciton−LO Phonon Interaction in a $CsPbBr_3$ Single Crystal, J. Phys. Chem. C 2020, 124, 18257−18263, doi: 10.1021/acs.jpcc.0c06254

[97] Maya Isarov, Liang Z. Tan, Maryna I. Bodnarchuk, Maksym V. Kovalenko, Andrew M. Rappe, and Efrat Lifshitz, Rashba Effect in a Single Colloidal $CsPbBr_3$ Perovskite Nanocrystal Detected by Magneto–Optical

Measurements, Nano Lett. 2017, 17, 8, 5020–5026 Publication Date:June 28, 2017, doi: 10.1021/acs.nanolett.7b02248

[98] Julian A. Steele, Pascal Puech, Bartomeu Monserrat, Bo Wu, Ruo Xi Yang, Thomas Kirchartz, Haifeng Yuan, Guillaume Fleury, David Giovanni, Eduard Fron, Masoumeh Keshavarz, Elke Debroye, Guofu Zhou, Tze Chien Sum, Aron Walsh, Johan Hofkens, and Maarten B. J. Roeffaers, Role of Electron−Phonon Coupling in the Thermal Evolution of Bulk Rashba–Like Spin–Split Lead Halide Perovskites Exhibiting Dual–Band Photoluminescence, ACS Energy Lett. 2019, 4, 9, 2205–2212, doi: 10.1021/acsenergylett.9b01427

[99] Adam D. Wright, Rebecca L. Milot, Giles E. Eperon, Henry J. Snaith, Michael B. Johnston, and Laura M. Herz, Band–Tail Recombination in Hybrid Lead Iodide Perovskite, Adv. Funct. Mater. 2017, 27, 1700860, doi: 10.1002/adfm.201700860

[100] Xiujun Gao, Quan Wang, Ye Zhang, Cuili Cui, Ning Sui, Xiaochun Chi, Hanzhuang Zhang, Qiang Zhou, Yongjun Bao, and Yinghui Wang, Pressure Effects on Optoelectronic Properties of $CsPbBr_3$ Nanocrystals, J. Phys. Chem. C 2020, 124, 20, 11239–11247, doi: 10.1021/acs.jpcc.0c02701

[101] Zhenchao Li, Ziming Chen, Yongchao Yang, Qifan Xue, Hin–Lap Yip & Yong Cao, Modulation of recombination zone position for quasi–two–dimensional blue perovskite light–emitting diodes with efficiency exceeding 5%, NATURE COMMUNICATIONS, (2019) 10:1027, 10.1038/s41467–019–09011–5

[102] Y. Zorenko, M. Nikl, J. A. Mares, V. Gorbenko, V. Savchyn, T. Voznyak, M. Kucera, A. Beitlerova, R. Kucerkova, A. Fedorov. The luminescent and scintillation properties of $YAlO_3$ and $YAlO_3$:Ce single crystalline films grown by liquid phase epitaxy from BaO–based flux. Phys. Status Solidi A, 2009, V. 206, No. 11, 2586–2592, doi: 10.1002/pssa.200925032

[103] C. E. Weir, E. R. Lippincott, A. Van Valkenburg, and E. N. Bunting, Infrared Studies In the 1– to I5–Micron Region to 30,000 Atmospheres, Journal of Research of the National Bureau of Standards–A. Physics and Chemistry, Vol. 63A, No. I, (1959), doi: 10.6028/jres.063A.003

[104] Agnès Dewaele, Paul Loubeyre, Florent Occelli, Olivier Marie & Mohamed Mezouar, Toroidal diamond anvil cell for detailed measurements under extreme static pressures, NATURE COMMUNICATIONS, 9, 2913, (2018), doi: 10.1038/s41467–018–05294–2

[105] J. C. Chervin , B. Canny and M. Mancinelli. Ruby–spheres as pressure gauge for optically transparent high pressure cells, High Pressure Research, 21, 305–314 (2006), doi: 10.1080/08957950108202589

[106] Chris J. H. Wort and Richard S. Balmer, Diamond as an electronic material, MaterialsToday, Volume 11, Issues 1–2, January–February 2008, Pages 22–28, doi: 10.1016/S1369–7021(07)70349–8

[107] https://asset.cloudinary.com/dppsafhfg/368f168280ba0894eb9fc82c772d956c

[108] Babin, V. Bichevin, V. Gorbenko, A. Makhov, E. Mihokova, M. Nikl, A. Vedda, S. Zazubovich, Y. Zorenko, Luminescence of dimer lead centers in aluminium perovskites and garnets, Phys. Status Solidi Basic Res. 246 (2009) 1318–1326, doi: 10.1002/pssb.200844492

[109] C.K. Jayasankar, K.R. Setty, P. Babu, W.B. Holzapfel, High–pressure luminescence study of Eu^{3+} in lithium borate glass, 214108 (2004) 1–7, doi: 10.1103/PhysRevB.69.214108

[110] C. Zhang, Z. Zhang, R.C. Dai, W. Zhongping, High–Pressure Raman and Luminescence Study on the Phase Transition of High–Pressure Raman and Luminescence Study on the Phase Transition of $GdVO_4:Eu^{3+}$, (2010), doi: 10.1021/jp106063c

[111] B.R. Jovanić, M. Dramićanin, B. Viana, B. Panić, Radiation Effects & Defects in Solids High–pressure optical studies of Y_2O_3 : Eu nanoparticles, 0150 (2008), doi: 10.1080/10420150802082705

[112] S. Zazubovich, A. Krasnikov, Yu. Zorenko, V. Gorbenko, V. Babin, E. Mihokova, and M. Nikl, Luminescence of Pb– and Bi–Related Centers in Aluminum Garnet, Perovskite, and Orthosilicate Single–Crystalline Films. Nanocomposite, Ceramic, and Thin Film Scintillators", p.227–287. Pan Stanford Publishing Pte. Ltd., 2016

[113] S. Sanyal, M.S. Akselrod, Anisotropy of optical absorption and fluorescence in Al_2O_3:C, Mg crystals, J. Appl. Phys. 98 (2005) 1–12, doi: 10.1063/1.1999032

[114] S Klotz, J–C–Chervin, P Munsch, and G Le Marchand, Hydrostatic limits of 11 pressure transmitting media, J. Phys. D: Appl. Phys. 42 (2009), doi: doi: 10.1088/0022–3727/42/7/075413

[115] W. Dewo, V. Gorbenko, Y. Zorenko, T. Runka, Raman spectroscopy of Ce^{3+} doped $Lu_3Al_5O_{12}$ single crystalline films grown onto $Y_3Al_5O_{12}$ substrate, Opt. Mater. X. 2019, 3, 100029, doi: 10.1016/j.omx.2019.100029

[116] M. Amilusik, D. Wlodarczyk, A. Suchocki, M. Bockowski, Micro–Raman studies of strain in bulk GaN crystals grown by hydride vapor phase epitaxy on ammonothermal GaN seeds, Jpn. J. Appl. Phys. 2019, 58, SCCB32, doi: 10.7567/1347–4065/ab1390

[117] W. Dewo, V. Gorbenko, Y. Syrotych, Yu. Zorenko, T. Runka, Mn Doped $XAlO_3$ (X = Y, Tb) Single Crystalline Film Grown onto $YAlO_3$ Substrates:

Raman Spectroscopy Study Toward Visualization of Mechanical Stress, J. Phys. Chem. C 2021, 125, 29, 16279–16288, doi: 10.1021/acs.jpcc.1c03922

[118] V. Kolobanov, V. Mikhailin, N. Petrovnin, D. Spassky, Yu. Zorenko. Exciton creation in $LuAlO_3$ single crystalline film. Phys. Stat. Sol. (b). 2006. V.243. P.R60–R62, doi: 10.1002/pssb.200642211

[119] H. Przybylińska, Chong–Geng Ma, M. G. Brik, A. Kamińska, J. Szczepkowski, P. Sybilski, A. Wittlin, M. Berkowski, W. Jastrzębski, and A. Suchocki, Evidences of multicenter structure of cerium ions in gadolinium gallium garnet crystals studied by infrared absorption spectroscopy, Phys. Rev. B 87, 045114 (2013), doi: 10.1103/PhysRevB.87.045114

[120] Yongjie Wang, D. Włodarczyk, Li Li, A. Wittlin, H. Przybylinska, P. Sybilski, Ya Zhydachevskii, Chong–Geng Ma, M.G. Brik, M. Malinowski, Yu Zorenko, V. Gorbenko, A. Suchocki, Electronic structure of Ce^{3+} in yttrium and lutetium orthoaluminate crystals and single crystal layers, Journal of Alloys and Compounds 723 (2017) 157e163, doi: 10.1016/j.jallcom.2017.06.235

[121] P. Dorenbos, The electronic level structure of lanthanide impurities in $REPO_4$, $REBO_3$, $REAlO_3$, and RE_2O_3 (RE = La, Gd, Y, Lu, Sc) compounds, J. Phys. Condens. Matter 25 (2013) 225501, doi: 10.1088/0953–8984/25/22/225501

[122] Yongjie Wang, M. Głowacki, M. Berkowski, A. Kamińska, Andrzej Suchocki, Comment on "Spectroscopic properties and location of the Ce^{3+} energy levels in $Y_3Al_2Ga_3O_{12}$ and $Y_3Ga_5O_{12}$ at ambient and high hydrostatic pressure" by S. Mahlik, A. Lazarowska, J. Ueda, S. Tanabe and M. Grinberg, Phys. Chem. Chem. Phys., 2016, 18, 6683, PCCP 2019, 21, 2816, doi: 10.1039/c8cp06154h

[123] J. J. Joos, D. Poelman and P. F. Smet, Energy level modeling of lanthanide materials: review and uncertainty analysis, Phys. Chem. Chem. Phys., 2015, 17, 19058, doi: 10.1039/c5cp02156a

[124] Wioletta Dewo, Katarzyna Łuczyńska, Yuriy Zorenko, Vitaliy Gorbenko, Kacper Drużbicki, Tomasz Runka, In silico Raman spectroscopy of $YAlO_3$ single–crystalline film, Spectrochimica Acta Part A: Molecular and Biomolecular Spectroscopy 231 (2020) 118111, doi: 10.1016/j.saa.2020.118111

[125] G. Venkataraman, Soft modes and structural phase transitions, Bull. Mater. Sci., 1 (1979) 129, doi: 10.1007/BF02743964.

[126] J. P. Perdew, K. Burke, M. Ernzerhof, Generalized Gradient Approximation Made Simple, Phys.Rev.Lett.77(1996)3865, doi: 10.1103/PhysRevLett.77.3865

[127] W. Dewo, K. Łuczyńska, Y. Zorenko, V. Gorbenko, K Drużbicki, T Runka, In silico Raman spectroscopy of $YAlO_3$ single–crystalline film., Spectrochimica Acta Part A: Molecular and Biomolecular Spectroscopy 231 (2020) 118111, doi: 10.1016/j.saa.2020.118111

[128] F. D. Murnaghan, The Compressibility of Media under Extreme Pressures, Proc. Natl. Acad. Sci. U.S.A. 30, 244 (1944), doi: 10.1073/pnas.30.9.244

[129] Zuocai Huang, Jing Feng, Wei Pan, First–principles calculations of mechanical and thermodynamic properties of $YAlO_3$, Computational Material Science 50 (2011) 3056, doi: 10.1016/j.commatsci.2011.05.028

[130] P. Łach, G. Karczewski, P. Wojnar, T. Wojtowicz, M. G. Brik, A. Kamińska, A. Reszka, B. Kowalski, and A. Suchocki, Pressure coefficients of the photoluminescence of the II–VI semiconducting quantum dots grown by molecular beam epitaxy, J. Luminescence 132, 1501 – 1506 (2012), doi: 10.1016/j.jlumin.2012.01.035

[131] M. G. Brik, P. Łach, G. Karczewski, T. Wojtowicz, A. Kamińska, and A. Suchocki, Theoretical studies of the pressure–induced zinc–blende to cinnabar structure phase transition in CdTe, Materials Chemistry and Physics 140, 216–221 (2013), doi: 10.1016/j.matchemphys.2013.03.024

[132] Yani He, Jilin Zhang, Wenli Zhou, Jin Han, Zhongxian Qiu, Liping Yu, Chunying Rong, and Shixun Lian, Multicolor Emission in a Single–Phase Phosphor $Ca_3Al_2O_6$:Ce^{3+}, Li^+: Luminescence and Site Occupancy, J. Am. Ceram. Soc., 97 [5] 1517–1522 (2014), doi: 10.1111/jace.12801

[133] P. Dorenbos, 5d–Level Energies of Ce^{3+} and the Crystalline Environment. II. Chloride, Bromide, and Iodide Compounds, Phys. Rev. B, 62 [23] 15650–9 (2000), doi: 10.1103/PhysRevB.62.15650

[134] P. Dorenbos, Calculation of the Energy of the 5d Barycenter of $La_3F_3[Si_3O_9]$:Ce^{3+}, J. Lumin., 105 [2–4] 117–9 (2003), doi: 10.1016/S0022–2313(03)00116–9

[135] P. Dorenbos, 5d–Level Energies of Ce^{3+} and the Crystalline Environment. III. Oxides Containing Ionic Complexes, Phys. Rev. B, 64, 1–12 (2001), doi: 10.1103/PhysRevB.64.125117

[136] ICSD 4115, FIZ Karlsruhe – Leibniz Institute for Information Infrastructure.

[137] L. Vasylechko, A. Senyshyn, and U. Bismayer, Perovskite–Type Aluminates and Gallates, Handbook on the Physics and Chemistry of Rare Earths, Volume 39, p. 113, Elsevier 2009, doi: 10.1016/S0168–1273(08)00002–0

[138] P. Dorenbos, E. G. Rogers, Vacuum Refered Binding Energies of the Lanthanides in Transition Metal Oxide Compounds, ECS Journal of Solid State Science and Technologies, 3 (2014) R150, doi: 10.1149/2.0061408jss

[139] V. V. Brazhkin, E. L. Gromnitskaya, I. V. Danilov, Y. Katayama, A. G. Lyapin, and S. V. Popova, High pressure behavior of P_2O_5 crystalline modifications: compressibility, elastic properties and phase transitions, Mater. Res. Express 2 (2015) 025201, doi: 10.1088/2053–1591/2/2/025201

[140] Pieter Dorenbos, Aday Josef, Johan T. M. De Haas, Karl W. Krämer, Vacuum referred binding energies of the lanthanides in chloride, bromide, and iodide compounds, Journal of Luminescence 208 (2019) 463–467, doi: 10.1016/j.jlumin.2019.01.009

[141] P. Dorenbos, Improved parameters for the lanthanide 4f q and 4f q−15d curves in HRBE and VRBE schemes that take the nephelauxetic effect into account, Journal of Luminescence 222, 2020, 117164, doi: 10.1016/j.jlumin.2020.117164

[142] Fang Hong, Binbin Yue, Naohisa Hirao, Guohao Ren, Bin Chen, and Ho–Kwang Mao, Pressure–induced isostructural transition in a distorted perovskite via octahedron reconfiguration, Appl. Phys. Lett. 109, 241904 (2016), doi: 10.1063/1.4972303

[143] Yu. Zorenko, V. Gorbenko, T. Voznyak, V. Mikhailin, V. Kolobanov, D. Spassky, M. Nikl, Intrinsic and Ce^{3+}–related luminescence in single crystalline films and single crystals of LuAP and LuAP:Ce perovskites, IEEE Trans. Nucl. Sci. 55 (3) (2008) 1192–1196, doi: 10.1109/TNS.2008.915690

[144] Jie Xue, Dandan Yang, Bo Cai, Xiaobao Xu, Wang, He Ma, Xuechao Yu, Guoliang Yuan, Yousheng Zou, Song, and Haibo Zeng, Photon–Induced Reversible Phase Transition in $CsPbBr_3$ Perovskite, Adv. Funct. Mater. 2019, 1807922, doi: 10.1002/adfm.201807922

[145] D. Cody, T. Tiedje, B. Abeles, B. Brooks, and Y. Goldstein, Disorder and the optical–absorption edge of hydrogenated amorphous silicon, Phys. Rev. Lett. 47, 1480–1483 (1981), doi: 10.1103/PhysRevLett.47.1480

[146] Xindi Mo, Xing Li, Guozhang Dai, Pei He, Jia Sun, Han Huang and Junliang Yang, All–inorganic perovskite $CsPbBr_3$ microstructures growth via chemical vapor deposition for high–performance photodetectors, Nanoscale, 2019, 11, 21386, doi: 10.1039/c9nr06682a

[147] Xianzhong Zhou and Ziyang Zhang, Electron–phonon coupling in $CsPbBr_3$, AIP Advances 10, 125015 (2020); doi: 10.1063/5.0017149

[148] Yevgeny Rakita, Sidney R. Cohen, Nir Klein Kedem, Gary Hodes, David Cahen, Mechanical Properties of $APbX_3$ (A=Cs or CH_3NH_3; X=I or Br) Perovskite Single Crystals, MRS Communications, Volume 5, Issue 4, December 2015, pp. 623 – 629, doi: 10.1557/mrc.2015.69

[149] J. Curtis Beimborn II, Leah M. G. Hall, Pornthip Tongying, Gordana Dukovic, and J. Mathias Weber, Pressure Response of

Photoluminescence in Cesium Lead Iodide Perovskite Nanocrystals, J. Phys. Chem. C 2018, 122, 20, 11024–11030, doi: 10.1021/acs.jpcc.8b03280

[150] G. Xiao, Y. Cao, G. Qi, L. Wang, C. Liu, Z. Ma, X. Yang, Y. Sui, W. Zheng, B. Zou, Pressure Effects on Structure and Optical Properties in Cesium Lead Bromide Perovskite Nanocrystals, J Am Chem Soc. 139 (2017) 10087–10094, doi: 10.1021/jacs.7b05260

[151] M. Li, T. Liu, Y. Wang, W. Yang, X. Lü, Pressure responses of halide perovskites with various compositions, dimensionalities, and morphologies, Matter and Radiation at Extremes. 5 (2020), doi: 10.1063/1.5133653

[152] Jingyu Qian, Bin Xu, Wenjing Tian, A comprehensive theoretical study of halide perovskites ABX_3, Organic Electronics Volume 37, October 2016, Pages 61–73, doi: 10.1016/j.orgel.2016.05.046

[153] T. Wang, B. Daiber, J.M. Frost, S.A. Mann, E.C. Garnett, A. Walsh, B. Ehrler, Indirect to direct bandgap transition in methylammonium lead halide perovskite, Energy Environ Sci. 10 (2017) 509–515, doi: 10.1039/c6ee03474h

[154] L.A. Riseberg, M.J. Weber, in Progress in Optics, 14, ed. E. Wolf, North–Holland Amsterdam (1975), doi: 10.1007/978–3–662–12213–6_6

[155] Shwetharani R, Halali V. Vishaka, Kusuma J, and R. Geetha Balakrishna, Green to Blue Light Emitting $CsPbBr_3$ Perovskite by Ligand Exchange and its Encapsulation by TiO_2 for Tandem Effect in Photovoltaic Applications, ACS Appl. Nano Mater. 2020, 3, 6089−6098, doi: 10.1021/acsanm.0c01293

[156] Yi Zhao, Ziyao He, Feiyang Ren, Wei Xia, Xiaojuan Liang, Lanlan Zhai, Weidong Xiang, One–step preparation of blue–emitting $CsPbBr_3$ quantum dots loaded on natural mineral halloysite nanot, Applied Clay Science 208 (2021) 106110, doi: 10.1016/j.clay.2021.106110

[157] Bowang Shu, Yajing Chang, Enze Xu, Supeng Yang, Jinhua Zhang, Yang Jiang, Xiaopeng Cheng, and Dabin Yu, Highly efficient and blue–emitting $CsPbBr_3$ quantum dots synthesized by two–step supersaturated recrystallization, Nanotechnology 32 145712 (2021), doi: 10.1088/1361–6528/abcc21

[158] S. Mahlik, A. Lazarowska, J. Ueda, S. Tanabe and M. Grinberg, Spectroscopic properties and location of the Ce^{3+} energy levels in $Y_3Al_2Ga_3O_{12}$ and $Y_3Ga_5O_{12}$ at ambient and high hydrostatic pressure, Phys. Chem. Chem. Phys., 2016, 18, 6683, PCCP 2019, 21, 2816, doi: 10.1039/C5CP07732J

[159] Elseiver copyrights web–page: https://www.elsevier.com/about/policies/copyright#Author–rights